## Measurement of Magnetic Susceptibility in Brain Cortical Tissue by Magnetic Resonance

Jorge Campos Pazmiño

Medical Physics Unit
McGill University, Montreal

A thesis submitted to McGill University in partial fulfilment of the degree of

M.Sc. Medical Physics

## **Table of Contents**

Acknowledgments			v
R	Lésumé		vii
L	ist of A	bbreviations	xii
1	Int	oduction	1
	1.1	Motivation	1
	1.2	Objectives	2
	1.3	Thesis outline and scientific contributions	3
2	Ma	gnetic Resonance Imaging	4
	2.1	Introduction	4
	2.2	Interactions of the main magnetic field with the nuclear spin	5
	2.3	Radiofrequency field and linear gradient fields	6
	2.4	Relaxation times	8
	2.5	Signal detection	11
	2.6	Multi-echo gradient echo sequence (mGRE)	12
3	Qua	antitative susceptibility mapping	18
	3.1	Introduction	18
	3.2	Theoretical development	19
	3.2.1	Basic physical definitions and the estimation of the magnetic susceptibility from the phase of	
	com	plex MRI data	19
	3.2.2	Data acquisition and phase processing	26
	3.2.3	Background removal	31
	3.2.4	Dipole inversion	34
	3.2.5	Direct field inversion methods	36
	3	2.5.1 Preconditioned Total Field Inversion (nTFI)	38

4 Methods and materials	42
4.1 QSM pipeline for conventional QSM and direct inversion methods	42
4.2 Evaluation of susceptibility maps using numerical simulations	46
4.2.1 Designing a brain numerical model for QSM	46
4.2.2 Comparison of phase unwrapping algorithms	54
4.2.3 Interaction between the unwrapping and the background removal techniques in convo	entional QSM.55
4.2.4 Evaluation of susceptibility maps using numerical simulations	56
4.2.4.1 Unwrapping and background removal in QSM	56
4.2.4.2 Comparison of conventional QSM and direct field inversion methods	57
4.2.4.3 Decoding the operation of direct inversion methods	58
4.2.4.4 Measurement of the susceptibility in anatomical ROIs	
4.2.4.5 Susceptibility estimation for varying SNR	59
4.3 Evaluation of susceptibility maps using <i>in vivo</i> datasets	60
4.3.1 In vivo data acquisition	60
4.3.2 Unwrapping algorithms comparison	62
4.3.3 Unwrapping and background removal techniques in conventional QSM	63
4.3.4 Evaluation of susceptibility maps using <i>in vivo</i> datasets	64
5 Results	66
5.1 Evaluation of susceptibility maps using numerical simulations	66
5.1.1 Comparison of phase unwrapping algorithms	66
5.1.2 Unwrapping and background removal techniques in conventional QSM	70
5.1.3 Evaluation of susceptibility maps using numerical simulations	74
5.1.3.1 Unwrapping and background removal in QSM	74
5.1.3.2 Comparison of conventional QSM and direct field inversion methods	77
5.1.3.3 Decoding the operation of direct inversion methods	80
5.1.3.4 Measurement of the susceptibility in anatomical ROIs	82
5.1.3.5 Susceptibility estimation for varying SNR	85
5.2 Evaluation of direct field inversion methods using <i>in vivo</i> datasets	88
5.2.1 Unwrapping algorithm comparison	88
5.2.2 Unwrapping and background removal techniques in conventional QSM	93
5.2.3 Evaluation of susceptibility maps using <i>in vivo</i> datasets	96

	6.1.1	Comparison of phase unwrapping algorithms	102
	6.1.2	Unwrapping and background removal techniques in conventional QSM	103
	6.1.3	Evaluation of susceptibility maps using numerical simulations	105
	6.1	.3.1 Unwrapping and background removal in QSM	106
	6.1	.3.2 Comparison of conventional QSM and direct inversion methods	107
	6.1	.3.3 Decoding the operation of direct inversion problems	108
	6.1	.3.4 Measurement of the susceptibility in anatomical ROIs	110
	6.1	.3.5 Susceptibility estimation for varying SNR	111
	6.2	Evaluation of susceptibility maps using in vivo datasets	112
	6.2.1	Unwrapping algorithms comparison	112
	6.2.2	Unwrapping and background removal techniques in conventional QSM	113
	6.2.3	Evaluation of susceptibility maps using in vivo datasets	114
	6.3	Limitations	116
7	Con	clusions and future work	118
	7.1	Conclusions	118
	7.2	Future work	119
R	eferenc	es	121

## Acknowledgments

First, I would like to thank my supervisor, Prof. Ives Levesque. I will be always thankful to him for giving me the opportunity to be part of the MRI Methods Research group. He has been the most inspiring and supportive mentor anyone could have wished for. He believed in me every step of the way while guiding me through the amazing world of MRI.

I would like to thank all the members of the MRI Methods Research group, especially Véronique Fortier and Marc-Antoine Fortin. They were incredibly supportive during the countless hours of work and contributed with valuable discussion for this thesis. Véronique Fortier, PhD, provided guidance and insights for the development of the thesis and the understanding of the theoretical background, provided the Quality Guided algorithm for phase unwrapping, reviewed the results and discussion sections of this thesis. Also, I would like to mention Alex Ensworth, MSc, who conducted the acquisition of the experimental information and provided the THUMPR algorithm for the correction of temporal phase wraps.

This has been a great challenge for me and, I would not have been capable of accomplishing anything without the people that made me feel at home: my MSc classmates Alaina, Alana, James, Kayla, and Sabrina; my roommate Chris; and Mylène, the most incredible translator.

Por último y no menos importante, todo lo que hago, lo hago por ellos. Todo es para mamá, papá, hermano y una Miau. Ellos significan el mundo para mí.

## **Abstract**

Quantitative susceptibility mapping (QSM) is an MRI modality that can estimate the magnetic susceptibility distribution of tissue. QSM uses the assumption that phase shifts in the complex MR measured data are primarily produced by susceptibility-induced field perturbations within the volume-of-interest. Thus, QSM calculates the susceptibility distribution by solving the inverse problem of deriving the susceptibility distribution from the field perturbation in the phase data, which is an ill-posed inverse problem. To solve the inverse problem, the measured phase data requires first post-processing (phase offset correction, phase unwrapping, and weighted least square fit to combine multi-echo phase information) and the removal of background magnetic field perturbations (field perturbations produced outside the volume-of-interest). The separation of QSM in three steps corresponds to conventional QSM. The approach adopted in conventional QSM tends to break down in regions surrounded by steep changes of susceptibility, like the cortical region of the brain.

Direct inversion methods combine the background removal and dipole inversion steps in a single algorithm and are proposed as a solution for the shortcomings of conventional QSM. The hypothesis of this project is thus that direct inversion methods are a better option to measure the susceptibility in the cortex when compared to conventional QSM.

The results of this project indicate that among the studied methods, conventional QSM is a better option for measuring the susceptibility in deep grey matter structures, while direct inversion techniques are a promising approach to measure the susceptibility in the cortex of the brain. But the lack of refinement of these methods when solving the ill-posed inverse problem highlights the need to improve current methods or to develop novel techniques based on this approach. Also, it is proposed in this thesis that direct inversion methods rely on the orthogonality between the subspaces spanned by dipolar fields inside and outside the volume-of-interest. This theoretical framework explains why direct inversion methods are a promising technique to measure susceptibility in the cortex. Moreover, the proposed explanation outlines the path to improve direct inversion techniques.

## Résumé

La cartographie quantitative de la susceptibilité magnétique (QSM, *Quantitative Susceptibility Mapping*) est une modalité d'IRM qui permet d'estimer la distribution de susceptibilité du tissu. La QSM part du principe que les variations dans les données complexes mesurées par la résonance magnétique perturbations du champ induites par la susceptibilité dans la région d'intérêt (ROI). Ainsi, la QSM calcule la distribution de susceptibilité en résolvant le problème inverse de la dérivation de la distribution de susceptibilité à partir de la perturbation du champ magnétique dans les données brutes, qui est un problème inverse mal-posé. Pour résoudre ce problème inverse, les données brutes mesurées doivent d'abord être traitées (correction du déphasage initial, déroulement de phase et combinaison des informations de la séquence d'écho de gradient par la méthode des moindres carrés pondérés) et les champs d'arrière-plan doivent être éliminés (perturbations du champ produites à l'extérieur de la région d'intérêt). La séparation de la QSM en trois étapes est typique de la QSM conventionnel. L'approche adoptée dans la QSM conventionnelle tend à échouer dans les régions qui présentent de fortes variations de susceptibilité telle que la région corticale du cerveau.

Les méthodes d'inversion directe combinent les étapes de suppression des champs d'arrière-plan et d'inversion du dipôle en un seul algorithme et sont proposées comme solution aux défauts de la QSM conventionnel. L'hypothèse de ce projet est donc que les méthodes d'inversion directe sont une meilleure option pour mesurer la susceptibilité dans le cortex par rapport à la QSM conventionnel.

Les résultats de ce projet indiquent que parmi les méthodes étudiées, la QSM conventionnel demeure la meilleure option pour mesurer la susceptibilité dans les structures profondes de la matière grise alors que les techniques d'inversion directe sont une approche prometteuse pour mesurer la susceptibilité dans le cortex du cerveau. Cependant, le manque de raffinement de ces méthodes lors de la résolution du problème inverse mal-posé souligne la nécessité d'améliorer les méthodes actuelles ou de développer de nouvelles techniques basées sur cette approche. Aussi, dans cette thèse, nous proposons que les méthodes d'inversion directe reposent sur l'orthogonalité

entre les sous-espaces couverts par les champs dipolaires à l'intérieur et à l'extérieur de la région d'intérêt. Ce cadre théorique explique pourquoi les méthodes d'inversion directe sont une technique prometteuse pour mesurer la susceptibilité dans le cortex. En outre, l'explication proposée esquisse la voie à suivre pour améliorer les techniques par inversion directe.

# **List of Figures**

Figure 2.1: Illustration of a B1 RF field circularly polarized and tuned to the Larmor frequency.
Figure reproduced from [17] with permission
Figure 2.2: T1, T2, and T2* relaxations illustrated in an MR signal over time. Figure reproduced
from [19] with permission
Figure 2.3: Schematic representation of quadrature detection. Figure adapted from [11] 12
Figure 2.4: Spoiled GRE sequence. Figure reproduced from [21] with permission
Figure 2.5: Multi-echo gradient echo sequence (mGRE). Figure adapted from [21]
Figure 3.1: Schematic representation of diamagnetic and paramagnetic materials after the
application of a magnetic field H. Figure reproduced from [29] with permission
Figure 3.2: Illustration of the Lorentz sphere approach to determine the demagnetization
magnetic field in a point of observation. Figure reproduced from [2] with permission
Figure 3.3: Representation of the unit dipole response function in image and Fourier space.
Figure reproduced from [2] with permission. 25
Figure 4.1: Schematic representation of the QSM pipeline created for this work. The pipeline is a
modified version of the pipeline used in [7]
Figure 4.2: Axial, sagittal, and coronal views of the T1-weighted dataset used to create numerical
models, head numerical model, and brain numerical models A and B
Figure 4.3: Image registration for T1w dataset and m GRE magnitude image using MATLAB. 49
Figure 4.4: Illustration of tissue classification for the numerical head model using BrainSuite 51
Figure 5.1: Unwrapped phase in a one-dimensional profile across an axial slice of the numerical
model B67
Figure 5.2: Maximum intensity projection (MIP) difference maps comparing the ground truth for
the unwrapped phase in numerical model B with the results calculated with different unwrapping
techniques and after correction using THUMPR
Figure 5.3: Comparison of background removal algorithms and the effect of unwrapping
techniques on numerical model B
Figure 5.4: Maximum intensity projection (MIP) difference maps in an eroded mask (6 voxels)
comparing the ground truth for the local field shift (LFS) in numerical model B with the results
calculated with different unwrapping techniques and background removal algorithm73
Figure 5.5: Maximum intensity projection (MIP) difference maps in a mask covering the entirety
of the brain comparing the ground truth for the local field shift (LFS) in numerical model B with

the results calculated with different unwrapping techniquesand background removal algorithm.
Figure 5.6: Axial and sagittal views of susceptibility maps for numerical model B for different
unwrapping techniques using conventional QSM and direct field inversion techniques
Figure 5.7: Maximum intensity projection (MIP) difference maps comparing the ground truth in
numerical model B and the susceptibility maps for different unwrapping techniques using
conventional QSM and direct field inversion techniques
Figure 5.8: Maximum intensity projection (MIP) difference maps comparing the ground truth of
the local field shift (LFS) maps obtained using PDF and forward modeling the susceptibility
distribution estimated by direct inversion methods
Figure 5.9: Comparison of conventional QSM and direct inversion methods in axial and sagittal
slices, and one-dimensional profiles
Figure 5.10: Representation of the operation of direct inversion methods. To illustrate how these
methods work, pLN-QSM was selected as an example
Figure 5.11: Histograms comparing the susceptibility distribution estimated by conventional
QSM and direct inversion methods with the ground truth in numerical model B
Figure 5.12: Bar plot of the mean and standard deviation in anatomical ROIs inside the
numerical models of the brain
Figure 5.13: Axial slice of numerical model B for different SNR values and QSM techniques 86
Figure 5.14: Box charts for the susceptibility measured at different SNRs (10, 20, 40, and 60) in
model B for the cortical region of the brain and the globus pallidus
Figure 5.15: Unwrapped phase in a one-dimensional profile across an axial slice in a <i>in vivo</i>
dataset
Figure 5.16: SEGUE and QG unwrapping difference in regions where the phase wraps are not
well-behaved90
Figure 5.17: Violin plots representing the phase distribution after spatial unwrapping (using QG)
at each echo before and after temporal phase unwrapping using THUMPR
Figure 5.18: Wrapped phase in an axial slice and one-dimensional profiles to study the changes
in wrapped and unwrapped phase (using QG) due to phase offset correction
Figure 5.19: Comparison of background removal algorithms and the effect of unwrapping
techniques on an in vivo dataset. In this figure, the rows determine the unwrapping technique
while the columns represent a different background removal method
Figure 5.20: Effect of phase offset correction in TFS and LFS maps. a), b), c), and d) present the
maps generated with different methods to calculate the phase offset correction and the
corresponding difference maps95

Figure 5.21: Susceptibility maps and difference maps for all dipole inversion and direct inversion	sion
methods paired with different unwrapping techniques	96
Figure 5.22: Effect of adding a preconditioner in LN-QSM.	97
Figure 5.23: Axial and sagittal views for conventional QSM and direct inversion methods	98
Figure 5.24: Systematic underestimation of susceptibility values in pTFI and pLN-QSM	99
Figure 5.25: Bar plot of the mean and standard deviation in anatomical ROIs in dataset B1	100

## **List of Tables**

Table 2.1: Approximate T1 and T2 relaxation values of different human body tissues at B0=3 T
and 37 °C. Values obtained from [18]
Table 2.2: Contrast in a 3D GRE sequence as function of flip angle, TE, and TR. The
information presented in the table was collected from [22]
Table 4.1: BrainSuite tags and susceptibility values used to identify regions in the head and brain
tissue. The susceptibility values were retrieved from [84]. The susceptibility values for regions
containing a mixture of components were determined as the average values of the susceptibility
of the individual components
Table 4.2: BrainSuite tags and susceptibility values for deep grey matter structures included in
model B. The values presented in the table were collected from [81] and correspond to the
average values for each structure using CSF as the zero reference
Table 4.3: 3D mGRE sequence parameters for collecting complex data for QSM experiments. 61
Table 4.4: MP-RAGE sequence parameters for T1w images
Table 5.1: RMSE values calculated in radians for each echo time and each unwrapping
technique. For each value at a determined echo time, the corresponding unwrapped phase
extracted from numerical model B was used as ground truth
Table 5.2: RMSE values (in rad) for SNR 10, 20, 40, and 60 comparing the unwrapped phase for
all techniques with the ground truth in model B
Table 5.3: RMSE calculated for the combination of unwrapping and background removal
techniques for numerical model B
Table 5.4: RMSE in ppb for numerical model B for different combinations of unwrapping
techniques and conventional and direct inversion QSM techniques
Table 5.5: Percent errors comparing the mean value of the susceptibility in anatomical ROIs and
the true values for the cortical region of the brain, thalamus, caudate nucleus, putamen, and
globus pallidus

## List of Abbreviations

**ANOVA** Analysis of variance

**ARLO** Auto-Regression on Linear Operations

**BET** Brain Extraction Tool

**BFC** Bias Field Corrector

**bSSFP** Balanced Steady-State Free Precession

**CN** Caudate nucleus

**CSF** Cerebrospinal Fluid

**DCT** Discrete Cosine Transform

dLu Discrete Laplacian Unwrapping

**E-SHARP** Extended SHARP

**FFT** Fast Fourier Transform

**FMRIB** Functional Magnetic Resonance Imaging of the Brain

**FOV** Field of view

**FSL** Functional Magnetic Resonance Imaging of the Brain Software Library

**GM** Grey Matter

**GP** Globus pallidus

**GRE** Gradient Echo

GUI Graphical User Interface

HARPERELLA HARmonic (background) PhasE REmovaL using the Laplacian operator

HC Heteroskedasticity-consistent

**HFEN** High Frequency Error Norm

**iSWIM** Iterative Susceptibility Weighted Imaging and Mapping

LBV Laplacian Boundary Value

LFS Local Field Shift

**LN-QSM** Least-Norm QSM

MEDI Morphology Enabled Dipole Inversion

Morphology Enabled Dipole Inversion with automatic uniform

MEDI+0 cerebrospinal fluid zero reference

mGRE Multi-echo gradient echo

MIP Maximum Intensity Projection

MP2RAGE Magnetization-Prepared two Rapid Acquisition Gradient Echoes

MRI Magnetic Resoncance Imaging

NIfTI Neuroimaging Informatics Technology Initiative

**PDF** Projection onto Dipole Fields

**pLN-QSM** Preconditioned Least-Norm QSM

**PRELUDE** Phase Region Expanding Labeller for Unwrapping Discrete Estimates

**pTFI** Preconditioned Total Field Inversion

PU Putamen

**QG** Quality Guided unwrapping

**QSM** Quantitative Susceptibility Mapping

**RDF** Relative Difference Field

**RESHARP** Regularization Enabled SHARP

**RF** Radiofrequency

**RMSE** Root-Mean-Square Error

**ROI** Region Of Interest

Phase Unwrapping with a Rapid Opensource Minimum Spanning TreE

AlgOrithm

scSWIM Structurally constrained Susceptibility Weighted Imaging and Mapping

**SEGUE** Speedy rEgion-Growing Algorithm for Unwrapping Estimated Phase

**SENSE** SENsitivity Encoding

**SHARP** Sophisticated Harmonic Artifact Reduction for Phase

**SNR** Signal to Noise Ratio

**SPURS** Simultaneous phase unwrapping and removal of chemical shift

SS Slice Selection

**SSIM** Structural Similarity Index Measure

**STAGE** Strategically Acquired Gradient Echo

STI Susceptibility Tensor Imaging

**TFI** Total Field Inversion

**TFIR** Regularized Total Field Inversion

**TGV** Total Generalized Variation

TH Thalamus

**THUMPR** Temporal pHase Unwrapping by Median Phase Restoration

**TKD** Truncated k-space Division

TV Total Variation

**UMPIRE** Unwrapping Multi-echo Phase Images with iRregular Echo spacings

V-SHARP Variable-kernel SHARP

**WM** White Matter

## Chapter 1

### Introduction

#### 1.1 Motivation

Quantitative susceptibility mapping (QSM) is an MRI modality that can estimate the underlying magnetic susceptibility distribution using MRI phase measurements generally obtained from a 3D GRE sequence [1], [2]. In the brain, the magnetic susceptibility of tissue can be used as a biomarker to detect several neurodegenerative diseases and a variety of brain lesions since it is mainly affected by the tissue water content, myelin, iron, and calcium [2]–[5]. A conventional QSM pipeline has three main steps: phase unwrapping, background field removal, and dipole inversion. Each step on its own is a challenging problem to solve and the separation into three steps just makes the outcome less accurate due to error propagation [6], [7]. Moreover, conventional QSM pipelines tend to perform poorly in the cortical region of the brain due to the nearby presence of the meninges, cerebrospinal fluid, blood flow, skull cortical bone, subcutaneous fat, and inaccuracies due to faulty brain extraction and edge erosion [6]–[8].

To overcome the shortcomings of conventional QSM, algorithms that combine the background removal and the dipole inversion in a single step have been proposed [6]–[10]. These methods will be referred to in this work as "direct inversion methods". However, some questions about direct inversion methods have been not fully addressed in the literature. Notable open questions regarding direct inversion methods are a comprehensive study of the effect of phase unwrapping in these methods, a clear delineation of the advantages and/or disadvantages of direct inversion methods when compared with conventional QSM, a description of the physical or mathematical assumptions that allow the separation of background and local fields, and a comparison of the performance of these methods in the cortex of the brain. Addressing these questions would

represent an advancement in the understanding of this particular set of techniques and on QSM in general. Moreover, addressing these questions could be valuable to refine the existing methods or to design novel QSM techniques capable of measuring susceptibility in critical regions like the cortex in the brain.

### 1.2 Objectives

The overall objective of this work was to determine whether or not direct inversion methods represent an improvement over conventional QSM when measuring the susceptibility in the cortical region of the brain. In this thesis, the term "conventional QSM" refers to QSM processing schemes that have independent steps for phase unwrapping, background field removal, and dipole inversion. On the other hand, "direct inversion QSM" corresponds to methods that combine the background removal and dipole inversion steps in a single algorithm while still requiring a separate step for phase unwrapping. The main objective of this thesis was achieved by building over three specific objectives designed to provide a compelling answer to the main research question.

The first objective of this work was to create a pipeline capable of producing susceptibility maps for conventional QSM and direct inversion methods and then compare the susceptibility maps obtained with both approaches. Also, the results of this work were used to establish the optimal methods for each step of the pipeline, especially for the direct inversion pipeline.

The second objective was to investigate the physical and mathematical principles behind the separation of local and background fields in direct inversion methods.

The third and final objective was to assess the performance of conventional QSM and direct inversion methods in deep gray matter structures and the cortical region of the brain. To accomplish this goal, the susceptibility was measured in these regions of the brain using numerical simulations and *in vivo* datasets.

### 1.3 Thesis outline and scientific contributions

Chapter 2 is a background chapter containing a brief review of basic MRI theory. Different topics are covered in this chapter including the interaction of magnetic fields with nuclear spins, the use of radiofrequency fields and linear gradients fields in MRI, relaxation, and signal detection. To close this chapter, multi-echo gradient echo sequences are explained since this sequence is the basis for collecting experimental information for QSM.

Chapter 3 is a literature review of QSM theory. The chapter starts with the theory of the ill-posed inverse problem for calculating the susceptibility distribution that produces a specific magnetic field and the relation between MR phase data and susceptibility-induced magnetic field perturbations. Subsequently, the chapter covers the data acquisition, phase data processing, background removal, and dipole inversion methods used in conventional QSM. Finally, the chapter presents a review of direct inversion methods. This review is focused on the methods analyzed in this thesis Preconditioned Total Field Inversion (pTFI), Least-Norm QSM (LN-QSM), and Regularized Total Field Inversion (TFIR).

Chapters 4, 5, and 6 are the methods, results, and discussion sections of this thesis. The methods section describes the design of the QSM pipeline, the design of the numerical models, the recollection of experimental data, and all the experiments performed with numerical simulations and *in vivo* datasets. Results and discussion chapters present the work done to compare the performance of conventional QSM and direct inversion methods in deep grey matter and the cortical region of the brain. Also, a theoretical framework for the operation of direct inversion methods is proposed.

Chapter 7 presents the conclusions for this project and the future work planned to create a novel direct inversion method.

## Chapter 2

### **Magnetic Resonance Imaging**

### 2.1 Introduction

MRI is a non-invasive imaging modality with a wide range of applications. In addition to anatomic imaging, MRI can be used for *in vivo* physiological studies and for mapping a plethora of chemical and physical parameters. Moreover, when compared with other imaging modalities that use X-rays for diagnostic purposes, like CT or traditional radiography, MRI offers comparable spatial resolution, better soft-tissue contrast, and no known health risks for the patient under normal operating conditions [11].

The name of this modality refers to the assortment of magnetic fields that are used to interact with the spin of nuclei in the molecules of the imaged object. The purposes of these fields are to set a net magnetization in the object, to excite the nucleus at frequencies that match the precessional frequency of the spins, and to encode spatial information regarding the location of the nucleus. The "nuclear" nature of this modality was omitted from the name to avoid the general public associating MRI with the use of ionizing radiation [12].

The beginning of MRI as a discipline dates back to two key years, 1946 and 1973. In 1946, Nuclear Magnetic Resonance (NMR) in condensed matter was discovered independently by Felix Bloch [13] and Edward Purcell [14] (work for which they shared the Nobel Prize in physics in 1952). In 1973, Paul Lauterbur [15] showed that it was possible to encode spatial information using spatially varying magnetic fields that change the Larmor frequency across the studied object. Afterward, during the 1980s, MRI went from being a research topic only limited to academia, to a thriving developing field in industry and medicine [11], [12].

### 2.2 Interactions of the main magnetic field with the nuclear spin

MRI is possible thanks to the interaction between nuclear spin and magnetic field, but not all nuclei are useful in this context. Nuclei used for imaging must have a nonzero intrinsic angular momentum. For the nuclei of atoms, the magnetic moment  $(\mu)$  and the total angular momentum (I, I)also called nuclear spin) are related by  $\mu = \gamma I$ , where  $\gamma$  is the gyromagnetic ratio. The total angular momentum arises from the intrinsic angular momentum (spin) and orbital angular momentum of the protons and neutrons in the nucleus [16]. But, since the nucleons tend to group in a way in which the angular momentum vanishes, this property can be described exclusively in terms of the unpaired nucleons in the outer shell [12]. Thus, only the nuclei with an odd number of neutrons, protons, or both (since in this case, the unpaired proton and neutron do not interact to create zero momentum) will have a nuclear spin and magnetic moment different from zero. This dependence of the angular momentum on the number of nucleons explains why elements like <sup>16</sup>O or <sup>12</sup>C cannot be used in MRI [12]. However, the nuclear configuration of an element is not the only criterion that needs to be considered for imaging purposes. The concentration of the element needs to be high enough to generate a measurable signal. <sup>1</sup>H (which can be described as a single proton of spin 1/2) is the main element used in MRI since it is the most abundant (non-zero spin) nucleus in the body. Apart from <sup>1</sup>H, <sup>23</sup>Na and <sup>31</sup>P have found some applicability in MRI [12].

When nuclear spins are placed in an external static magnetic field (denoted by  $\mathbf{B_0}$ ), magnetization and precession take place. For spin 1/2 particles placed in a magnetic field, there are two possible energy states in which the spin is parallel or anti-parallel to the  $\mathbf{B_0}$  orientation. The parallel spin state corresponds to the lowest energy level. Although the spins tend to occupy the lowest energy state, the magnitude of thermal excitations is big enough to exceed the energy gap between the two states. The ratio of spin populations is described by Boltzmann statistics as [11]:

$$\frac{n_{-}}{n_{+}} = e^{-\Delta E/kT} = e^{-\gamma \hbar B_0/kT}$$
 2.1

Where  $n_-$  and  $n_+$  are the number of spins in the anti-parallel and parallel states, respectively,  $\Delta E$  is the energy gap, k is the Boltzmann constant, and T is the temperature. This expression can be used to calculate the small excess of  $n_+$ , when compared to  $n_-$ , which explains the macroscopic

magnetization of an object placed in the magnetic field. The equilibrium nuclear magnetization  $M_0$  can be calculated as [11]:

$$M_0 = \frac{N\gamma^2 \hbar^2 I_z (I_z + 1) B_0}{3kT}$$
 2.2

Where N is the number of nuclear spins and  $I_z$  is their spin (for protons,  $I_z = 1/2$ ).

On the other hand, precession can be explained using a classical approach. When a magnetic dipole  $\mu$  is placed in a static magnetic field  $B_0$ , the equation of motion is described by the Bloch equation [12]:

$$\frac{\mathrm{d}\mu}{\mathrm{d}t} = \gamma\mu \times \mathbf{B_0} \tag{2.3}$$

The solution to this equation represents a precessional movement of the magnetic dipole around the field direction, with an angular frequency given by the Larmor relation [12]:

$$\mathbf{\omega} = \gamma \mathbf{B_0} \tag{2.4}$$

Where the angular velocity vector is  $\mathbf{\omega} = -\omega \hat{\mathbf{z}}$  since it represents a left-handed rotation. The value of  $\gamma$  depends on the nucleus placed in the magnetic field. In the case of  $^{1}$ H,  $\gamma = 267.522 \times 10^{6} [\text{rad} \cdot \text{s}^{-1} \cdot \text{T}^{-1}]$  (or  $\gamma/2\pi = 42.577 [\text{MHz} \cdot \text{T}^{-1}]$  [12]).

### 2.3 Radiofrequency field and linear gradient fields

In addition to the main magnetic field, other magnetic fields are used in MRI to generate an image. These two fields are the radiofrequency (RF) field  $\mathbf{B_1}$  and linear gradient field  $\mathbf{G}$ .

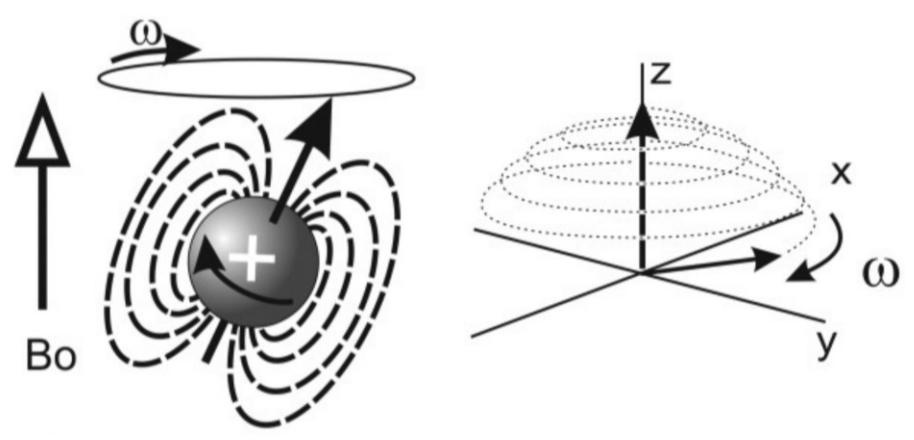


Figure 2.1: Illustration of a  $\mathbf{B_1}$  RF field circularly polarized and tuned to the Larmor frequency. The RF field produces the precession of the magnetization towards the x-y plane. Figure reproduced from [17] with permission.

Due to the application of the main field  $\mathbf{B_0}$ , the spins are in equilibrium along the  $\hat{\mathbf{z}}$  direction. To measure an MR signal, it is required to move the spin out of the equilibrium position, for which an oscillating magnetic field  $\mathbf{B_1}$  with a frequency that matches the precession frequency of the spins is applied. For the nuclei and magnitude of the main fields used in MRI, the frequency of  $\mathbf{B_1}$  is within the RF spectrum. The field  $\mathbf{B_1}$  is oriented in the x-y plane and it is circularly polarized. The torque that  $\mathbf{B_1}$  applies over the spins rotates the magnetization vector towards the x-y plane as illustrated in Figure 2.1. The angle of rotation of the magnetization depends on the magnitude of the field and the time of duration of the RF pulse. After shifting the magnetization from the equilibrium position, the rotating component of the magnetization along the x-y plane induces, according to Faraday's law, an electromotive force into a receiver coil oriented to detect the component of the magnetization along the x-y plane [11].

The other magnetic fields used in MRI correspond to linear gradients. These fields are used to encode spatial information in the signal detected by the receiver coils or to allow the selective excitation of only certain regions of interest of the element inside the scanner. Three different gradients are applied to linearly change the magnitude of the main magnetic field in the three orthogonal directions  $\hat{\mathbf{x}}$ ,  $\hat{\mathbf{y}}$ , and  $\hat{\mathbf{z}}$  (while the orientation of the field remains along the  $\hat{\mathbf{z}}$  direction). Thus, with the combination of the three gradients, the magnitude of the main magnetic field can be altered such that it represents a spatial position. Consequently, the frequency of the spins also changes with the position (as described by equation 2.4). By analyzing the frequency content of

the obtained signal, the magnetization can be mapped to a specific spatial position [11]. The change in frequency due to the linear gradients can be expressed as:

$$\omega(\mathbf{r}) = \gamma(\mathbf{B}_0 + \mathbf{G} \cdot \mathbf{r}) \tag{2.5}$$

Where **G** is the linear gradient vector field and  $\mathbf{r}$  is the position vector. The magnitude of the gradient field along each orthogonal orientation is usually less than 10 [mT/m] [11].

### 2.4 Relaxation times

Once the magnetization is moved out of the equilibrium position, it does not stay permanently in this excited state. The analysis of the magnetization state of the system can be performed by decomposing the magnetization into parallel or longitudinal ( $M_z$ ) and transverse ( $M_{xy}$ ) components (to the orientation of  $B_0$ ). The return to the equilibrium position is called relaxation and it takes place in both magnetization components. The dominant mechanism that mediates relaxation in biological tissues is magnetic dipole-dipole interaction [11].

Longitudinal relaxation refers to the recovery of the longitudinal magnetization ( $M_z$ ) after the RF excitation. This phenomenon is quantified by the relaxation time  $T_1$ , which represents the time required to recover about 63% of the maximum magnetization at thermal equilibrium ( $M_0$ ) along the longitudinal direction (when assuming  $M_z(t=0)=0$ ). This process is mainly caused by the exchange of energy between the nuclei and the surrounding medium. The exchange of energy is caused by random fluctuations in the magnetic fields due to the motion of the surrounding magnetic dipoles [11]. Since  $T_1$  relaxation implies the system returning to thermal equilibrium, the exchange of energy involves transitions of the spins to the  $n_+$  population. These transitions involve the transverse component of the magnetization becoming zero at the same time the longitudinal component recovers [12]. The magnetic field fluctuations that produce these transitions need to have an x-y component at a frequency close to the spins' resonant frequency, which depends on the main magnetic field. Thus, the value of  $T_1$  depends on the magnitude of  $B_0$ . The value of  $T_1$  increases with increasing  $B_0$  because higher frequencies are linked to higher energy exchanges

required for relaxation [11]. The relaxation of the magnetization along the longitudinal orientation can be expressed as [11]:

$$M_z(t) = M_0 + (M_z(0) - M_0)e^{-\frac{t}{T_1}}$$
 2.6

On the other hand, the transverse relaxation represents the decay of the transverse magnetization  $(M_{xy})$  towards zero. It is quantified using the parameter  $T_2$ , which represents when the transverse magnetization has fallen to about 37% of its initial value. As mentioned previously, longitudinal relaxation is accompanied by transverse relaxation. However, there are additional mechanisms that cause  $T_2$  relaxation, without altering the longitudinal component. Thus,  $T_2 \le T_1$  [12]. Transverse relaxation, in addition to the field fluctuations in the x-y component, is caused by fluctuations on the  $\hat{\mathbf{z}}$  component due to neighbor dipoles interacting between each other. These fluctuations dominate this relaxation process and manifest themselves as a dephasing of the transverse components of the spin system. Consequently, the magnetization in this orientation becomes zero. Since these field fluctuations do not depend on the main field strength,  $T_2$  does not depend on  $B_0$  [11]. The relaxation of the magnetization along the longitudinal orientation can be expressed as [11]:

$$M_{xy}(t) = M_{xy}(t)e^{-\frac{t}{T_2}}$$
 2.7

Figure 2.2 illustrates  $T_1$  and  $T_2$  behaviors as a function of time. On the other hand, Table 2.1 shows  $T_1$  and  $T_2$  values for representative tissues at  $B_0=3$  T and 37 °C [18].

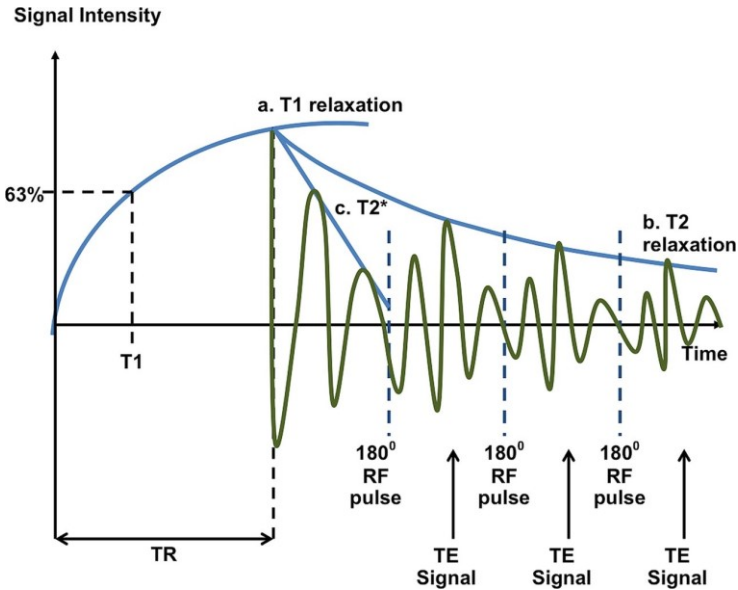


Figure 2.2:  $T_1$ ,  $T_2$ , and  $T_2^*$  relaxations illustrated in an MR signal over time. (a)  $T_1$  relaxation appears as a longitudinal magnetization recovery over time (it is assumed that it occurs after an RF pulse not showed in the image). (b)  $T_2$  relaxation takes place as a decay of the transverse magnetization over time. (c)  $T_2^*$  is also a decay of the transverse magnetization. The difference between these two phenomena is that  $T_2^*$  relaxation will naturally take place as observed in c).  $T_2$  decay is observed only when additional RF refocusing pulses are used. In the case of the image,  $180^\circ$  RF pulses are used to temporally cause a signal gain due to the rephase of the spins (spin echo). The maximum gain after each refocusing pulse will not be the same in each case and it will be affected by  $T_2$  relaxation. Figure reproduced from [19] with permission.

Table 2.1: Approximate  $T_1$  and  $T_2$  relaxation values of different human body tissues at  $B_0=3$  T and 37 °C. Values obtained from [18].

Tissue	T <sub>1</sub> [ms]	T <sub>2</sub> [ms]
Gray matter (GM)	$1820 \pm 114$	99 ± 7
White matter (WM)	$1084 \pm 45$	69 ± 3
Skeletal muscle	$1412 \pm 13$	50 ± 4
Spinal cord	993 ± 47	$78 \pm 2$
Blood	$1932 \pm 85$	$275 \pm 50$

In reality, the decay of the transverse component is faster than the one predicted by  $T_2$ . This additional dephasing is caused by external field inhomogeneities. This effect is described by the

parameter  $T_2'$ . The total transverse relaxation can be expressed through the value  $T_2^*$  as  $T_2^{*-1} = T_2^{-1} + T_2'^{-1}$ . The effect of  $T_2'$  can be reversed by the design of the pulse sequence used during imaging [12].  $T_2^*$  relaxation and an example of how the pulse sequence can make the signal decay according to  $T_2$  instead of  $T_2^*$  are illustrated in Figure 2.2.

Relaxation can be included in the Bloch equation as:

$$\frac{d\mathbf{M}}{dt} = \gamma \mathbf{M} \times \mathbf{B} - \frac{1}{T_1} (\mathbf{M}_z - \mathbf{M}_0) \hat{\mathbf{z}} - \frac{1}{T_2^*} (\mathbf{M}_x \hat{\mathbf{x}} + \mathbf{M}_y \hat{\mathbf{y}})$$
2.8

### 2.5 Signal detection

To produce a measurable signal, a combination of RF pulses is used to produce a non-zero value for the magnetization in the x - y plane. A model for the complex-valued received signal ( $s_r(t)$ ) generated by a volume of precessing transverse magnetization can be stated as (neglecting gain factors and constant phase factors) [11]:

$$s_{\mathbf{r}}(t) = \iiint M_{0}(\mathbf{r})e^{-\frac{t}{T_{2}(\mathbf{r})}}e^{-i\omega_{0}t}\exp\left(-i\gamma\int_{0}^{t}\mathbf{G}(t)\cdot\mathbf{r}\,d\tau\right)d\mathbf{V}$$
 2.9

In the model presented in equation 2.9, the magnetization  $M_0(\mathbf{r})$  depends on MR paramaters like the proton density, while the three exponential terms account for relaxation, precession, and the effect of gradient fields. From a practical perspective, the measured signal is demodulated and collected using quadrature detection [11]. The physical signal  $(s_p(t))$  is demodulated by scaling it by a reference (sinusoidal or cosinusoidal) signal. The frequency of this reference signal is  $\Omega = \omega_0 + \delta \omega$  and it may include an offset  $\delta \omega$  from the Larmor frequency [12]. Demodulation of the signal is equivalent to analyzing the recorded signal from the perspective of the rotating frame of reference [12]. After demodulation of the signal, it is collected as two outputs corresponding to the real and imaginary components of the baseband signal. Quadrature detection is illustrated in Figure 2.3. In the figure, the frequency offset was selected as zero. The low-pass filtering step is required for eliminating high-frequency components that are produced after the introduction of the

reference signal for demodulation [11]. After demodulation and filtering, real (in-phase) and imaginary (quadrature) components for the signal are obtained.

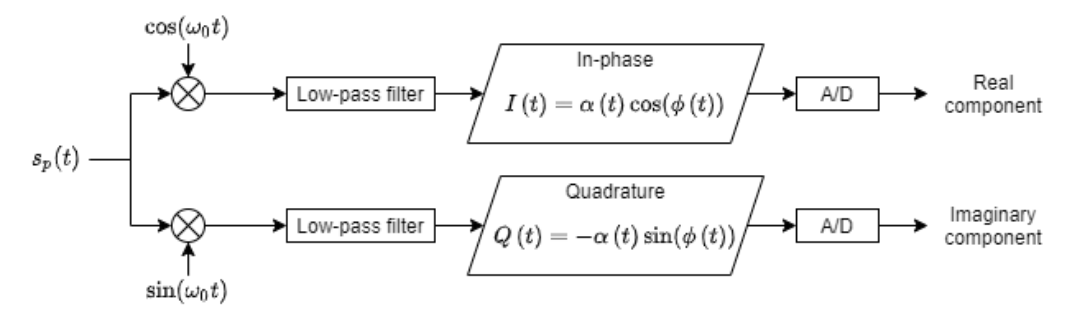


Figure 2.3: Schematic representation of quadrature detection. Quadrature detection produces two outputs, real (in-phase) and imaginary (quadrature) components, for the measured physical signal. The outputs are obtained after demodulation (using sinusoidal/cosinusoidal reference signals) and low-pass filtering. Figure adapted from [11].

The signal equation (equation 2.9) can be interpreted as a Fourier transform of the magnetization, where the coordinates in Fourier space (or k-space) are given by [11]:

$$k(t) = \frac{\gamma}{2\pi} \int_{0}^{t} \mathbf{G}(\tau) d\tau$$
 2.10

Identifying that the signal equation represents the Fourier transform of the magnetization sheds some light on how MRI encodes spatial information. By sampling the signal at a specific time, it is possible to collect information in k-space, which later can be subjected to an inverse Fourier transform to reconstruct the image. Relation 2.10 shows that the gradient fields establish how the information for the image reconstruction is collected in k-space. The pulse sequence determines how the magnetization is excited and the information in k-space is collected.

### 2.6 Multi-echo gradient echo sequence (mGRE)

An MR pulse sequence is a particular combination of RF pulses and gradients with different parameters and timing. Depending on the pulse sequence, it is possible to generate MR images with different appearances or to measure different information [20]. In general, there are two fundamental types of imaging pulse sequences: spin-echo and gradient-echo. Even though it was not discussed thoroughly, a spin-echo sequence was shown in Figure 2.2 to illustrate T<sub>1</sub>, T<sub>2</sub>, and

T<sub>2</sub>\* relaxation. Conversely, gradient echo sequences will be explored in detail since this sequence is of great relevance in the following chapters.

Due to relaxation, it is impossible to excite the system with a single RF pulse and collect information for an infinite amount of time since the measurable signal decays exponentially. Although, depending on the selected pulse sequence, it is possible to introduce a combination of excitations and linear gradients (appropriately timed) to collect enough information in k-space to overcome this limitation and create images (or maps in the case of quantitative MRI) with different contrasts and spatial resolutions depending on the desired application for the MR image (map). One specific sequence relevant for this work is called 3D multi-echo gradient echo (mGRE) sequence.

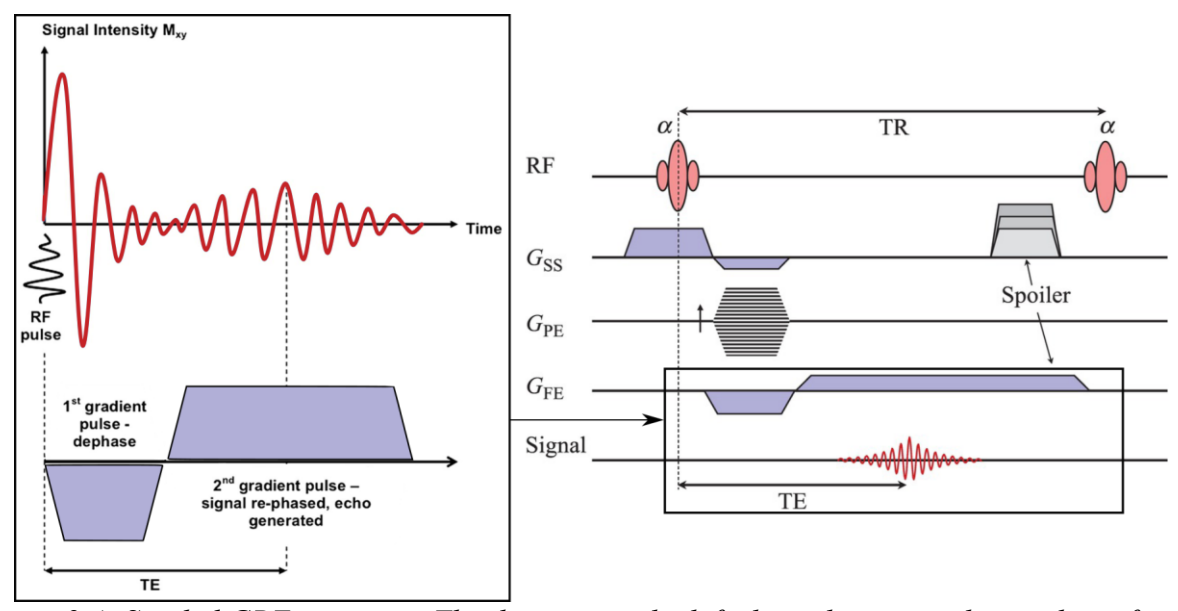


Figure 2.4: Spoiled GRE sequence. The diagram at the left shows how a gradient echo is formed once the area of the lobes of the gradients in  $G_{FE}$  is equal to zero. The diagram at the right shows the entire pulse sequence, including the possibility to add variable gradient spoiling to eliminate the remaining transverse magnetization. Figure reproduced from [21] with permission.

Before diving into 3D mGRE sequences, it is necessary to first explore 2D GRE sequences. In Figure 2.4, a typical 2D gradient echo sequence is illustrated. First, the volume of interest is divided into slices through a process called selective excitation. In this case, a linear gradient is set in a particular direction causing the Larmor frequency to be modulated across this direction. Thus, an

RF pulse will be capable of exciting only a portion (perpendicular to the orientation of the gradient) of the volume. The magnitude of the gradient and the position of the slice along the axis set the central frequency required to excite a slice of infinitesimal width. The shape of the RF pulse determines the profile and width of the slice generated in the volume of interest. For this work, the slice selection gradient will be considered as  $G_z$  and is illustrated in Figure 2.4 in the SS (slice selection) axis. The first (positive) lobe corresponds to the gradient used to select the slice, while the second (negative) lobe is used to refocus the spins across the selected slice. Since the slice has a finite thickness, there would be some linear dephasing proportional to z that can be reversed with the negative lobe in the slice selection orientation [11]. The additional gradient in SS (spoiler) will be discussed later.

Once the slice is selected, the data acquisition in k-space turns into a 2D problem. To collect information, different patterns can be used to sample k-space but in this case, only a 2D grid will be considered. The position in  $k_x$  and  $k_y$  is given by equation 2.10. Thus, the position is defined by two gradients  $G_x$  and  $G_y$ , which are also called frequency/readout ( $G_{FE}$ ) and phase encode ( $G_{PE}$ ) gradients, respectively. These two gradients are illustrated in Figure 2.4. The difference between the two gradients is that the phase encode gradient is used exclusively to alter the position in k-space for acquiring data, meaning changing the row in the 2D grid in which information will be acquired. On the other hand, the frequency encode gradient is used to sample k-space while the data acquisition is turned on [11].

The use of linear gradients (according to equation 2.9) adds extra dephasing that causes a faster signal decay than the decay predicted by  $T_2$  relaxation. However, this dephasing can be reverted. Since the added phase in the frequency encode direction depends on the integral in equation 2.10, for  $G_x$  the value of the integral can be made zero by considering a negative lobe followed by a positive lobe as illustrated in Figure 2.4, such that the area under the negative and positive gradients is zero (in other words when the readout direction coincides with the point  $k_x = 0$ ). The lost phase due to the negative gradient is recovered as soon as the positive gradient is applied, reaching a maximum possible recovery once the areas counteract each other. This increase in signal amplitude is called a gradient echo. The instant in time in which the echo occurs is denominated as TE. However, regardless of the signal amplitude increased, the magnitude at time TE decays

exponentially (with time) according to  $T_2^*$  relaxation. The effect of relaxation cannot be avoided and in contrast to other sequences, like a spin echo sequence, no 180° is used to cause  $T_2$  relaxation instead of  $T_2^*$  [11].

The scan time in a 2D GRE sequence is given by [22]:

Scan time (2D GRE) = 
$$TR \times N_v \times NEX \times number of slices$$
 2.11

Where TR is the repetition time (meaning the time between the RF pulses at the beginning of each GRE sequence),  $N_y$  is the number of phase encode steps, and NEX is the number of excitations (the number of times that a given line in k-space is repeatedly taken to improve SNR).

A notable property of the GRE sequence is that its relatively short scan time enables 3D GRE volume imaging in a reasonable amount of time. Under these circumstances, a volume is selected instead of a slice and within this volume, the acquisition is done with an extra (secondary) phase encode gradient in the orientation of the  $G_z$  gradient. This extra gradient allows the sampling of k-space equivalently to the phase encode gradient. 3D GRE sequences result in advantages like thinner "slices" (often referred to as "partitions") when compared to regular slice selection and increased SNR (since SNR  $\propto \sqrt{N_z}$ , where  $N_z$  is the number of phase encode steps in the  $G_z$  gradient direction). The disadvantage is longer scan times depending on the number of extra phase encode steps  $N_z$  added, although scan times can be kept reasonably low by considering short TR and small flip angles [22]:

Scan time (3D GRE) = 
$$TR \times N_y \times N_z \times NEX$$
 2.12

The parameters that affect the contrast in a 3D GRE sequence are the flip angle, TR, TE, and spoiling. The general effect of flip angle, TR, and TE in the contrast in a 3D GRE sequence is presented in Table 2.2. The combination of these parameters also changes the amount of residual transverse magnetization remaining before the RF excitation. This residual magnetization appears when the TR is too short for a given flip angle, such that there is not enough time to allow for complete T<sub>2</sub>\* relaxation. The amount of residual transverse magnetization before the RF pulse changes from cycle to cycle, but after the first few cycles, this value reaches a steady state. The steady-state component of the transverse magnetization affects the contrast such that its growth also increases the amount of T<sub>2</sub>\* weighting [22]. Nevertheless, keeping or removing this residual transverse magnetization requires extra considerations. To keep the residual transversal

magnetization a combination of alternating RF pulses, spoiling gradients in the SS and readout directions, and rewinder gradients along the phase-encoding are required as implemented in GRASS/FISP/FFE sequences. On the other hand, eliminating the transverse magnetization requires spoiling using RF and variable gradient spoiling as done in SPGR/FLASH/T1-FFE sequence (the addition of variable gradient spoiling is illustrated in Figure 2.4).

Table 2.2: Contrast in a 3D GRE (non-balanced) sequence as function of flip angle, TE, and TR. An estimation for "small", "large", "short", and "long" flip angle, TE, and TR values are included in the table. The combinations of the parameters not presented in the table mostly corresponds to mixed contrast cases. The information presented in the table was collected from [22].  $PDw = proton\ density-weighted$ ,  $Tlw = T_1-weighted$ ,  $T2*w = T_2*-weighted$ 

Parameter	Enhanced PDw	Enhanced T1w	Enhanced T2*w
Flip angle	Small (5° to 30°)	Large (60° to 90°)	Small (5° to 30°)
TE	Short (2-5 ms)	Short (2-5 ms)	Long (10-100 ms)
TR	Short/Long	Long (~100 ms)	Short $(TR < 3T_2^*)$

The GRE sequence presented in Figure 2.4 can be modified with additional frequency encode gradients to include not only one echo but multiple echoes for a single RF excitation, as illustrated in Figure 2.5. In order to fit more than a single echo acquisition inside an excitation in a GRE sequence, the readout can be performed either in a single k-space direction or in both. In the first case, an opposite signed gradient must be applied after each acquisition while the signal is not sampled to enable the acquisition from the same orientation in k-space as the previous one. This type of readout with a gradient to reposition the signal sampling is called unipolar readout, monopolar readout, or flyback readout. In Figure 2.5, the use of a unipolar readout corresponds to only collecting the blue signal. On the other hand, instead of using a gradient just to change the position in k-space without sampling the signal, it is possible to acquire information in both orientations, during the positive and negative lobes of the gradient used to move the acquisition through k-space in the readout orientation. This type of acquisition is called bipolar readout. In Figure 2.5, the use of a bipolar readout corresponds to collecting the blue and purple signals. Generally, in the case of a flyback readout the unused readout pulse lobes (purple lobes) are redesigned to be as short in duration as possible when used as flyback gradient pulses.

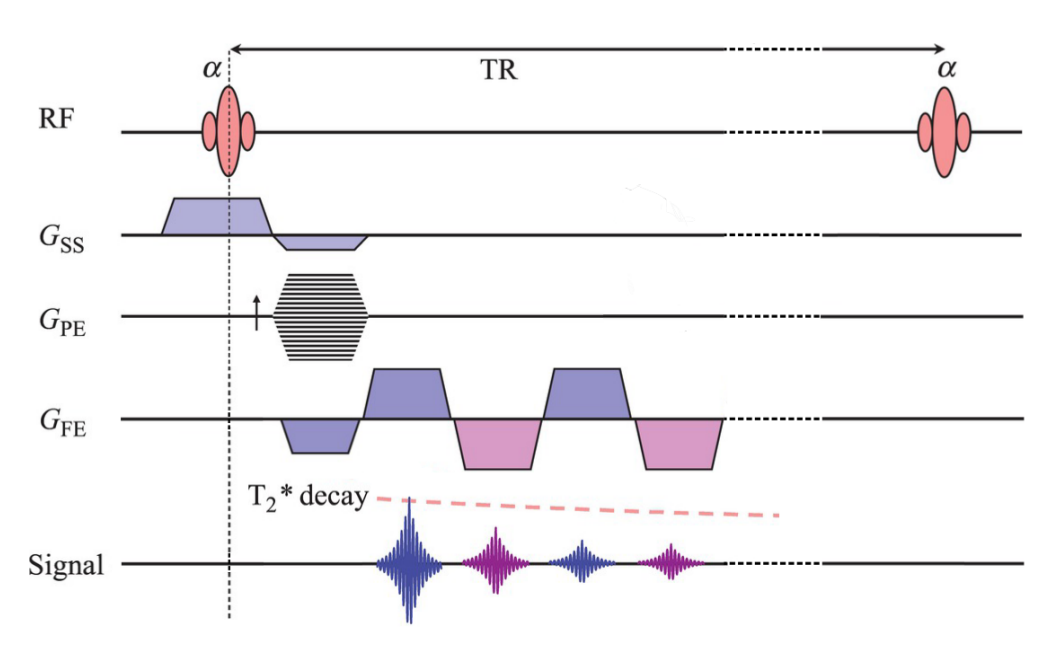


Figure 2.5: Multi-echo gradient echo sequence (mGRE). Compared to the sequence in Figure 2.4, more than one echo can be collected by introducing additional frequency encode gradients. Figure adapted from [21].

Each echo will occur at different times  $TE_1$ ,  $TE_2$ ,  $TE_3$ , etc. The measurements at the different echoes will have different  $T_2^*$ -weighting. Additionally, a 3D extension to this sequence is also possible in a similar fashion as discussed for a GRE sequence. The addition of a "phase encode" gradients in the  $G_z$  direction would produce a 3D mGRE sequence. This sequence will be the focus when discussing the acquisition of MR complex data for QSM.

## Chapter 3

### Quantitative susceptibility mapping

#### 3.1 Introduction

QSM is an MRI technique that estimates the susceptibility distribution of the underlying tissue [2]. Its development started in the mid-1990s. QSM emerged as further advancement of susceptibility weighted imaging (SWI). In SWI, phase information is (generally) obtained using a spoiled gradient echo (GRE) sequence, with long echo times, short flip angles, and high field strengths. This results in altered  $T_2^*$  contrast that depends on the change of susceptibility throughout tissue. SWI highlights regions of short  $T_2^*$ . Thus, small changes in susceptibility are manifested as signal intensity loss, while steep changes (that lead to short relaxation values) are represented as signal hyperintensity [23]. In comparison with SWI, which creates magnetic susceptibility weighted images and depicts its perturbing effect in the main magnetic field; QSM creates quantitative maps of the susceptibility.

In QSM, phase (and in some cases magnitude) information is combined with post-processing techniques for the estimation of the susceptibility distribution. In biological tissue, the theoretical determination of the susceptibility distribution is an extremely complex task due to a myriad of factors like the variety of molecules and ions forming the tissue, the cellular arrangement of each tissue, and the complex cellular environment surrounding each tissue. QSM measures the relative susceptibility variation of the tissue inside a voxel, meaning that the measured values are not absolute susceptibilities. Generally, CSF is selected as the zero reference [5]. The susceptibility variation across tissue is what drives the contrast in susceptibility maps. The structures that cause the biggest contrast are those with strong susceptibilities. Therefore, the source of contrast changes depending on the tissue. In WM, lipids correspond to the main source of contrast due to the myelination of axons. In deep brain tissue, such as putamen, globus pallidus, thalamus, and caudate

nuclei, the contrast is driven by iron-rich molecules which are highly paramagnetic [5]. There are other structures outside the central nervous system that possess a strong susceptibility including them the kidneys, heart, and liver. In each case, different structures are the main source of susceptibility: the membranes of the nephrons in the kidneys, the  $\alpha$ -helixes of myofilaments in the myocardium, and iron concentration in the liver [5]. Although, QSM has found extensive application for imaging the brain, its use in other regions of the body is an active field of research [24]–[26].

### 3.2 Theoretical development

## 3.2.1 Basic physical definitions and the estimation of the magnetic susceptibility from the phase of complex MRI data

When a material is placed in an external magnetic field, it may become magnetized. From a macroscopic point of view, the material can be pictured as an assembly of tiny magnetic dipoles. When these dipoles interact with a magnetic field, they align parallel (paramagnetism) or antiparallel (diamagnetism) to the magnetic field. When the material is removed from the magnetic field, the alignment of the dipoles is lost, except in ferromagnetic material [27]. The magnetization **M** is a vector field that represents the magnetic moment per unit of volume and it relates the fields **B** and **H** [27], [28] inside a material (there is no magnetization in vacuum):

$$\mathbf{B} = \mu_0(\mathbf{H} + \mathbf{M}) \tag{3.1}$$

In the special case of linear media,  $\mathbf{M} = \chi \mathbf{H}$  (or equivalently  $\mathbf{B} = \mu_0 \left(\frac{1}{\chi} + \mathbf{1}\right) \mathbf{M}$ ), the magnetization and the magnetic field are proportional, where the constant of proportionality is the magnetic susceptibility. The magnetic susceptibility is a macroscopic physical parameter that describes the response of a material to an applied magnetic field, meaning the magnetic moment induced by the magnetic field  $\mathbf{H}$ . The sign of the susceptibility indicates if the material is diamagnetic or paramagnetic. For  $\chi < 0$  the material is diamagnetic, while for  $\chi > 0$  the material is paramagnetic [28]. The behavior of paramagnetic and diamagnetic materials depending on the applied field is illustrated in Figure 3.1.

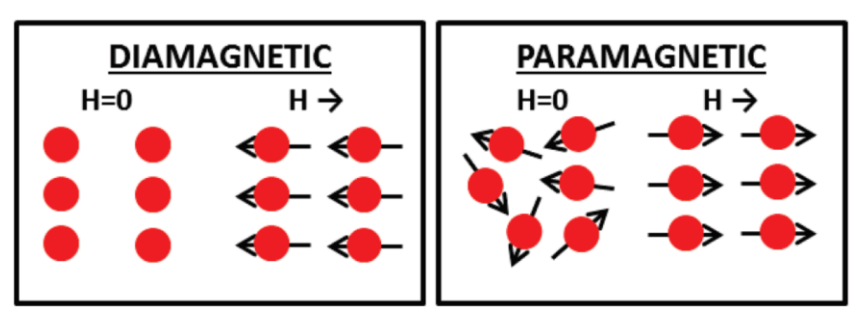


Figure 3.1: Schematic representation of diamagnetic and paramagnetic materials after the application of a magnetic field **H**. Figure reproduced from [29] with permission.

Regardless of the apparent simplicity of relation 3.1, defining magnetic fields in magnetizable media requires extreme caution. When a magnetizable material is placed inside a magnetic field, that will be noted as  $\mathbf{B_{ext}}$ , the magnetic field that is established inside the material can be considerably different from the external field. The reason for this difference is that the external magnetic field induces a magnetization inside the material. This magnetization produces its own magnetic field named demagnetization field  $\mathbf{B_{demag}(r)}$ , which physically arises from the magnetization at the surface of the material or any region in which  $\nabla \cdot \mathbf{M} \neq 0$  [30], [31]. Thus, the magnetic field inside the material would be the sum of the external field and the demagnetization field [28]

$$B(r) = B_{ext}(r) + B_{demag}(r)$$
3.2

The demagnetizing corrections can be neglected only if the magnetization of the material is considerably low when compared with the external magnetic field **H** [28]. However, in the case of MRI, the demagnetization field can be used to quantify susceptibility-induced perturbations and consequently, the susceptibility distribution producing these perturbations (as done in QSM) [5].

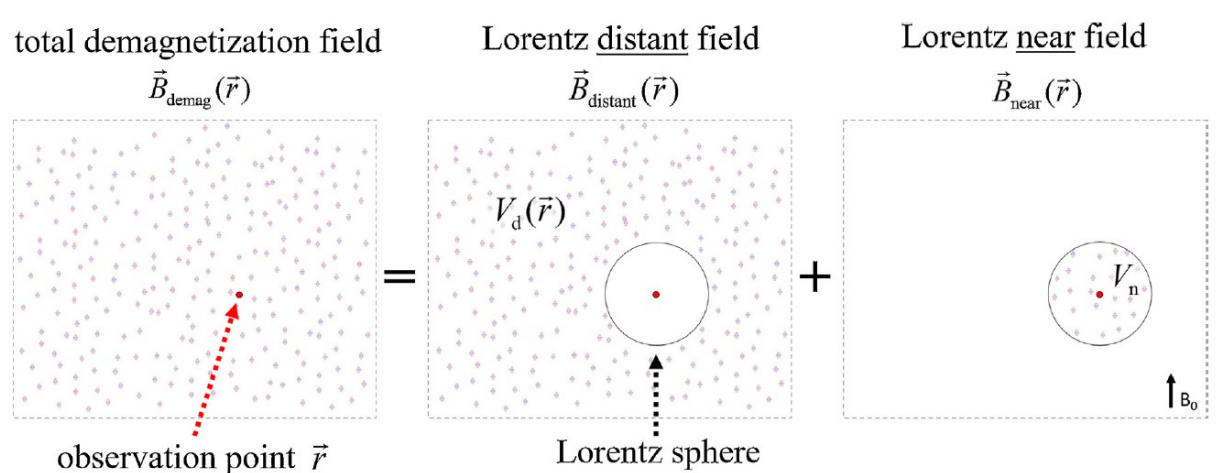


Figure 3.2: Illustration of the Lorentz sphere approach to determine the demagnetization magnetic field in a point of observation. The image illustrates how the volume is divided into two regions by a virtual surface defined as the Lorentz sphere. The volume outside the sphere generates the distant magnetic field, while the volume inside generates the near field. The demagnetization field at the point of observation is the sum of the distant and near fields. Figure reproduced from [2] with permission.

To calculate the value of  $B_{demag}$ , it is possible to use the Lorentz sphere formalism. This formalism is illustrated in Figure 3.2. The main idea behind this approach is to divide the field into two different contributions that originate in the "distant" region  $V_d$  and "near" region  $V_n$ , such that  $B_{demag}(r) = B_{distant}(r) + B_{near}(r)$ . In  $V_d$ , the dipoles are treated as a continuous magnetic moment density. In  $V_n$  the dipoles are considered discrete elements. The surface (called Lorentz surface) separating these two regions is arbitrary in shape and size. However, the estimation is more accurate for a large  $V_n$ , although the term linked to this region becomes more complex to solve. On the other hand, the Lorentz surface cannot be too small since the magnetic field in the distant region must be modeled as a continuous medium (which would not be possible if  $V_n$  is small). The minimum size of the Lorentz field should be equivalent to the distance between adjacent dipoles [2]. How to calculate these terms is outside the scope of this thesis (a full derivation of the terms  $B_{distant}(r)$  and  $B_{near}(r)$  is presented in [2]). But what is relevant in this case is that the knowledge of these terms enables the calculation of the demagnetization field in terms of the susceptibility distribution (producing the field perturbations corresponding to the demagnetization field) and external applied field  $B_{ext} = B_0 \hat{\mathbf{z}}$ :

$$\mathbf{B_{demag}}(\mathbf{r}) = \mathbf{B_{ext}} (\chi_{app} * b_{\chi})(\mathbf{r})$$
 3.3

The term  $\chi_{app}(\mathbf{r})$  is the susceptibility value evaluated at the point  $\mathbf{r}$  and the symbol \* denotes the convolution. The "app" subscript stands for "apparent" and it was selected to illustrate the fact that the expression considers the effective susceptibility along the direction of the main external field. More generally,  $\chi_{app} = \widehat{\mathbf{z}^T} \cdot \overline{\chi} \cdot \widehat{\mathbf{z}}$  where  $\overline{\chi}$  is the susceptibility tensor. The term  $b_{\chi}(\mathbf{r})$  corresponds to the dipole kernel, which is the magnitude of the dipolar field (without including the constant  $\mu_0$ ) when the magnetization and field are oriented parallel to  $\widehat{\mathbf{z}}$ :

$$b_{\chi}(\mathbf{r}) = \begin{cases} \frac{3\hat{\mathbf{r}}(\hat{\mathbf{z}} \cdot \hat{\mathbf{r}}) - \hat{\mathbf{z}}}{4\pi \|\mathbf{r}\|_{2}^{3}} \cdot \hat{\mathbf{z}}, & \mathbf{r} \neq \mathbf{0} \\ 0, & \mathbf{r} = \mathbf{0} \end{cases}$$
3.4

The demagnetization field (in terms of the susceptibility distribution inducing this field) can be used to derive the backbone equation of QSM. By replacing equation 3.3 in 3.2 and taking the Fourier transform of the resulting expression the following equation can be obtained:

$$\operatorname{FT}\left\{\frac{\operatorname{B}(\mathbf{r}) - \operatorname{B}_{0}}{\operatorname{B}_{0}}\right\} = \operatorname{FT}\left\{\chi_{\operatorname{app}}(\mathbf{r})\right\} \odot \operatorname{FT}\left\{b_{\chi}(\mathbf{r})\right\}$$
 3.5

The expression inside the Fourier transform on the left-hand side of the previous expression is called Relative Difference Field (RDF) in QSM literature [2]. However, in this work, the term Local Field Shift (LFS) was preferred over RDF to make a clear distinction between the relative field before and after background field removal (which will be discussed later in this chapter). The symbol  $\odot$  is the Hadamard product. Lastly, labeling the Fourier transform of the dipole kernel as  $b_{\chi}(k) = FT\{b_{\chi}(\mathbf{r})\}$ , the kernel expressed in Fourier space is ([1], eq. 5):

$$b_{\chi}(\mathbf{k}) = \begin{cases} \frac{1}{3} - \frac{k_{z}^{2}}{k}, & \text{for } k \neq 0\\ 0, & \text{for } k = 0 \end{cases}$$
 3.6

The definition of this function at  $\mathbf{k} = \mathbf{0}$  requires some discussion. As reported by Marques and Bowtell ([32], [33]), this value corresponds to the average field offset of the magnetic field and it can be used to adjust the magnetic field to fulfill specific boundary conditions. Setting the value

of 3.6 as 0 in  $\mathbf{k} = \mathbf{0}$  is equivalent to include the Lorentz sphere correction (equivalent to a phase offset of  $-\frac{2}{3}\mu_0 M$ ) in equation 3.3 within the volume corresponding to the Lorentz sphere. This assumption is also equivalent to setting the value over the sphere as zero.

The idea behind QSM is to use equation 3.5 to estimate the value of  $\chi_{app}(\mathbf{r})$  by measuring data that can be used to infer the susceptibility-induced magnetic field perturbations, which corresponds to the numerator on the left-hand side of equation 3.5. This information is contained in the phase of the complex signal obtained using a 3D multi-echo gradient echo (mGRE) sequence. The phase image can be obtained by taking the arctangent of the ratio the imaginary and real parts of the complex data,  $S_{Im}$  and  $S_{Re}$ , as in  $\Theta = \tan^{-1}(S_{Im}/S_{Re})$ .

In a 3D mGRE sequence, the FID decays with  $T_2^*$  relaxation and the signal is affected by susceptibility effects [22]. The magnetic field inside the object placed in the scanner changes in relation to the main field value  $B_0$ , consequently the frequency  $\omega_0 = \gamma B_0$  also presents shifts across the object. These shifts (in the magnetic field or frequency) are caused due to intrinsic inhomogeneities in the main field, chemical shifts, and susceptibility-induced effects. In many scenarios, from these three sources of field (frequency) inducing inhomogeneities in the main field, only susceptibility effects are of relevance. In modern scanners, the use of passive shimming allows for inhomogeneities intrinsic to the particular scanner to be of the order of 1-2 ppm, while active shimming reduces these inhomogeneities even further [33]. Chemical shift effects can be neglected in some regions like brain tissue [2]. Consequently, the only effects remaining in the brain are the ones caused by the bulk susceptibility distribution [33]. Retaining the effects of susceptibility-induced fields in the signal can be undesirable in some circumstances since it can lead to various artifacts (especially close to air/tissue interfaces) and fast signal decay due to transverse dephasing. However, this information can be exploited to quantify the susceptibility distribution of the underlying tissue in QSM.

Variations in magnetic susceptibility cause long-ranging field distortions that affect the GRE complex data to produce signal voids and/or geometrical image distortions [34]. Geometric distortions are a factor that should be accounted for since distortion-free images are desirable when studying the anatomy in QSM images. However, it has been reported that at 3 T, no noticeable

geometric distortions have been observed in QSM brain images in deep brain nuclei, peripheral cortex, and ventricular system [35]. In fact, susceptibility maps can be used to predict and/or remove air/tissue and bone/tissue interface effects in the complex GRE data [1]. In this thesis, all the data was acquired at 3 T, and consequently it will be assumed that geometric distortions are not a factor that will affect the depiction of the anatomy in the brain. This assumption would not hold for higher field strengths or when considering different acquisitions modes such as echoplanar imaging (EPI) [36].

In principle, the phase evolves linearly with time. That said, there are second-order effects that introduce non-linearities in the phase evolution. It is still an open question how these effects can be accounted for in the QSM problem and how they affect the estimation of the susceptibility in the resulting map [2], [37]. The linear phase accumulation can be modeled as [1]:

$$\Theta(\mathbf{r}, TE_i) = \phi_0(\mathbf{r}) + \phi(\mathbf{r}, TE_i) = \phi_0(\mathbf{r}) + \gamma \Delta B_z(\mathbf{r}) TE_i$$
 3.7

This expression contains two terms, one that is time-independent corresponding to  $\phi_0(\mathbf{r})$  and a second term  $\phi(\mathbf{r}, TE_i) = \gamma \Delta B_z(\mathbf{r}) TE_i$  that depends on the echo time TE and  $\Delta B_z(\mathbf{r}) = B(\mathbf{r}) - B_0$  (which represents the field perturbations). The term  $\phi_0$  is called the transceiver phase offset [2] and it depends on factors like the phase distribution after RF excitation and receiver coil sensitivity [37], [38]. This factor needs to be removed before using the phase of the complex signal to determine the field perturbations. The phase data that includes the phase offset is denoted in this work by  $\Theta(\mathbf{r}, TE_i)$ .

In the case of a single RF coil, equation 3.7 represents the accrued phase measured by it. In the case of using a phased array, each coil element will collect phase information described by equation 3.7. Then, the information from each coil must be combined to generate a composite signal. Generally, during the unification of the phase from different coils, the phase offset of each coil is eliminated (phase matching), which is not a trivial task since the way in which this parameter is handled will affect the final susceptibility map. Different methods for phase matching and combining the phase information of the coils in the assembly are described in [37]. However, even after phase matching, the composite signal often contains a phase offset due to time-independent contributions that cannot be removed through phase matching. One particular example is the use

of parallel imaging in the form of SENSE since this technique keeps transmit phase contributions [2].

After removal of the transceiver offset, equation 3.7 can be replaced into equation 3.5 to obtain the following expression:

$$FT\left\{\frac{1}{\sqrt{TE}}\phi(r)\right\} = B_0FT\left\{\chi_{app}(r)\right\} \odot FT\left\{b_{\chi}(r)\right\}$$
 3.8

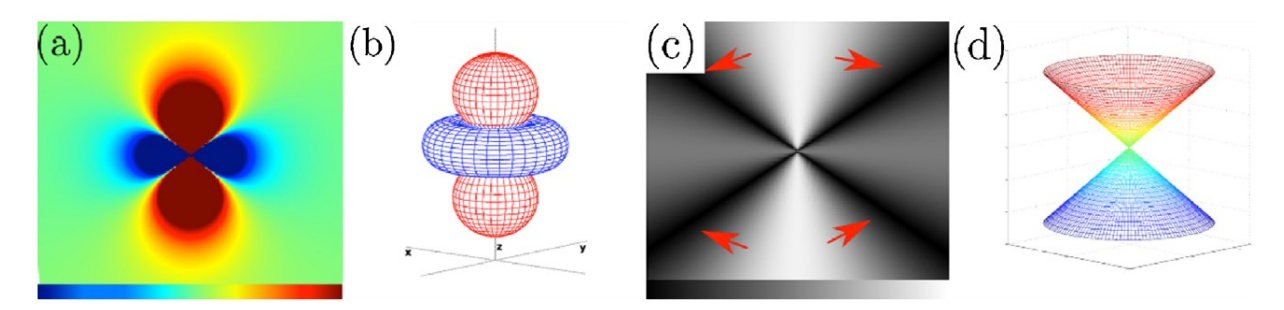


Figure 3.3: Representation of the unit dipole response function in image and Fourier space. b) and d) are surface plots of the unit dipole in image space and Fourier space, respectively. a) and d) correspond to sagittal slices of b) and d). The red arrows in c) indicate the "problematic" conic region in Fourier space where the function is zero and close to zero. Figure reproduced from [2] with permission.

In principle, equation 3.8 is easy to solve for  $\chi_{app}(r)$ . It is simply required to divide each element at both sides of the equality by the corresponding element of  $B_0FT\{b_\chi(r)\}$  and subsequently perform an inverse FFT. Sadly, the problem is far more complex. Looking at the unit dipole response function in k-space (illustrated in Figure 3.3), the function is zero in a well-defined region. Equation 3.6 can be alternatively stated as [2]:

$$b_{\chi}(\mathbf{k}) = \begin{cases} \frac{1}{3} - \cos^2 \beta, & \text{for } k \neq 0 \\ 0, & \text{for } k = 0 \end{cases}$$
 3.9

Where  $\beta$  is the angle between the vectors  $\mathbf{k}$  and  $\mathbf{k_z}$ . Then, it is easy to see that dividing an element by the value of the function  $b_{\chi}(\mathbf{k})$  is not possible when  $\cos^2(\beta) = \frac{1}{3}$ , which happens for  $\beta = \frac{1}{3}$ 

 $54.74^{\circ}$ . The set of points corresponding to zero in the k-space forms a conical surface. It is impossible to estimate the information corresponding to  $FT\{\chi_{app}(r)\}$  at the points coinciding with the conical surface from the information of the accumulated phase alone. Moreover, for the points close to the conical surface, the value of the dipole response is extremely small, making the pointwise product in equation 3.8 small compared with the noise in the measured data [2]. Due to these constraints, the inverse problem linked to equation 3.8 becomes ill-posed.

Alternatives to solve the ill-posed inverse problem will be explored in the following subsections when addressing either dipole inversion process or direct field inversion methods. However, even reaching the point in which is it necessary to solve the inverse problem first requires to overcome other obstacles. Therefore, an entire pipeline to process the information from the complex signal is required.

## 3.2.2 Data acquisition and phase processing

The most widely used pulse sequence to obtain MR complex data for QSM is 3D mGRE sequence. As described in the previous subsection, the signal obtained from this sequence contains information on the magnetic susceptibility-induced effects. The phase information at multiple echo times can be used to determine the phase offset  $\phi_0(\mathbf{r})$  and magnetic field shift  $\Delta B_z(\mathbf{r})$  in equation 3.7. Other acquisition techniques can be used instead of GRE. This work is exclusively based on 3D mGRE data acquisition, but there is research for QSM involving other acquisition techniques like balanced Steady-State Free Precession (bSSFP) [37], Magnetization-Prepared two Rapid Acquisition Gradient Echoes MP2RAGE [39], multi-echo, and multi-flip angle data collected using Strategically Acquired Gradient Echo (STAGE) [40].

From this point, it will be assumed that the information from multiple coil elements has been combined and multiple echoes were acquired at different echo times. To combine the data from all the echoes, it is required to first eliminate the remaining phase offset  $\phi_0(\mathbf{r})$ . However, analyzing the phase and removing the phase offset first requires further consideration about whether the readout gradients were unipolar or bipolar. Each readout type has its advantages and disadvantages, and the selection will affect how phase offset corrections and echo combination are performed.

Unipolar gradients provide consistency to the measured phase at different echo times since the use of bipolar gradients introduces discrepancy between odd and even (or positive and negative gradient lobes) echoes due to non-ideal effects like waveform delays and eddy currents caused by the rapid sign switching of the gradients. In contrast, bipolar readout allows for better acquisition efficiency and reduced echo spacing. Since QSM relies on small field perturbations to estimate the susceptibility distribution, unipolar readouts are better for achieving higher accuracy. Although, if better acquisition efficiency is required, bipolar readouts can be used in QSM after considering corrections to mitigate non-ideal behaviors. Gradient waveform polarity and its effect in QSM have been studied in detail in [41]. For this research project, unipolar readout gradients were used to collect data, thus every technique discussed will be centered around this case.

For a unipolar acquisition, one way to calculate the phase offset for all echoes consists in using the phase measured during the first two echoes. Denoting the phase unwrapping operation as U[ ], the unwrapped phase with symbols  $\varphi_u$  and  $\Theta_u$ , and the wrapped phase with  $\varphi_w$  and  $\Theta_w$ , the unwrapped phase for the first echo can be determined as:

$$\phi_{1u} = \left(\frac{U\left[\angle\left[\exp\left(i\Theta_{w}(\mathbf{r}, TE_{2})\right)\exp\left(-\Theta_{w}(\mathbf{r}, TE_{1})\right)\right]\right]}{TE_{2} - TE_{1}}\right)TE_{1}$$
3.10

This phase can then be used to estimate the correction factor:

$$\exp(i\phi_0) = \exp(i\Theta_w(\mathbf{r}, TE_1)) \exp(-i\phi_u(\mathbf{r}, TE_1))$$
3.11

The correction factor can be used through complex division to eliminate the phase offset from each measurement. The advantage of this approach is that it enables an optimal SNR in the phase images since it includes smoothing of the  $\phi_0$  correction before it is applied [37]. Moreover, imposing smoothness in  $\phi_0$  is consistent with the assumption that this distribution is dominated by the phase of the  $B_1$  transmit and receive fields [3]. The drawback is that the method is relatively computationally demanding (compared with other methods) since it requires unwrapping of the phase difference in equation 3.10. Another advantage of this method is that it can be easily adapted

to bipolar readouts, in which case a correction for odd and even echoes can be created using the first two odd and first two even echoes separately [42].

Once the phase offset has been removed using complex division, it is necessary to unwrap the phase data  $\phi(\mathbf{r}, TE_i)$  at each echo time. Unwrapping was already introduced in equation 3.10 but it has not been explained yet. When measuring phase as part of a complex signal, the values of the phase can be retrieved only in an interval of  $2\pi$ . In this case, the interval will be defined as  $(-\pi, \pi]$ , but in reality, any interval of the form  $(\phi_L, \phi_L + 2\pi]$  for a lower limit  $\phi_L$  can be used. Choosing a particular value for  $\phi_L$  can be convenient to avoid phase wrapping as discussed in [37]. Any value of phase measured outside the range  $(-\pi, \pi]$  would be "wrapped" inside the range by the addition or subtraction of a multiple integer of  $2\pi$ . These wraps are discontinuities following phase isocontours that manifest themselves as 2D closed isolines or 3D closed isosurfaces [37]. The problem in principle can be solved simply by adding or subtracting the opposite phase shift that caused the wrapping, but this is an ill-posed problem since there is an infinite number of solutions but only a single correct physical solution [43]. To solve this problem, additional assumptions are generally required. Most often, spatial and temporal smoothness of the unwrapped phase is assumed [1]. Moreover, the phase unwrapping problem becomes even more challenging due to unreliable phase values produced by noise and phase aliasing that produce abnormal fringe lines [44]. One example of these abnormalities is open-ended fringe lines, meaning non-closed isocontours that are interrupted by residues (a 2-by-2 voxel loop) that cannot be unwrapped by adding a multiple of  $2\pi$  [37].

The most basic algorithm to unwrap phase in a 1D case is Itoh's method, but this method can be severely affected by sampling and noise [45]. Additionally, it cannot be efficiently generalized to higher dimensions. For phase unwrapping in the context of MRI, there are different types of algorithms to handle this problem. In this work, three of the main categories will be considered: Laplacian unwrapping, path-following methods, and temporal unwrapping. Other categories include region-growing unwrapping like PRELUDE [46] and its successor SEGUE [47]), and graph-cut unwrapping like SPURS [48]. The theory presented below about phase unwrapping technique is mostly (except where it is explicitly cited) supported by [37].

Laplacian unwrapping exploits the fact that even though the phase is limited to the interval  $(-\pi, \pi]$  and it is discontinuous due to phase wraps, the exponential function is continuous in the complex plane and  $e^{i\varphi_w(r)} = e^{i\varphi_u(r)}$  [43]. Then, the unwrapped phase can be determined as [43]:

$$\nabla^2 \varphi_u = \operatorname{Im} \left( e^{-i\varphi_w} * \nabla^2 e^{i\varphi_w} \right) = \cos(\varphi_w) \nabla^2 \sin(\varphi_w) - \sin(\varphi_w) \nabla^2 \cos(\varphi_w) \quad 3.12$$

This relation corresponds to a discrete Poisson equation, which can be solved to find the unwrapped phase. The solution can only be obtained up to harmonic terms (terms whose Laplacian vanishes). These terms cannot be accurately retrieved unless boundary conditions for the problem are considered. In the case of QSM, getting the solution without the contribution of these terms can actually be desirable since these phase contributions would correspond to harmonic fields and consequently backgrounds fields that would be eliminated by some of the background field removal algorithms. Background fields, and the methods to remove them, will be explained in subsection 3.2.3 On the other hand, the inclusion of a second-order operator suppresses large phase changes in the unwrapped phase modifying large field shifts [4], [49], [50].

There are several ways to solve equation 3.12 and a detailed study of each possible solution is outside the scope of this thesis, but a brief overview of how these methods work will be provided here. The basic idea consists in solving the right-hand term in equation 3.12 using the collected experimental information, which will be equivalent to find the (discrete) Laplacian of the unwrapped phase. Then, the unwrapped phase can be obtained through a deconvolution with the Laplacian kernel. Then, this approach requires a definition of the forward and inverse discrete Laplacian kernels (meaning the kernel used for the deconvolution) to be used. The most common discrete operators used to build Laplacian kernels correspond to the finite difference operator, fast Fourier transform (FFT), and the discrete cosine transform (DCT). A deeper overview of many variations to implement these operators and some of their characteristics in the context of QSM are provided in [1], [37]. However, it is important to highlight that when defining the forward and inverse Laplacian kernels, it is better to use the same discrete operators for both kernels [43]. Also, the boundary conditions are often implicitly or explicitly defined when setting the kernels [37].

Path-following methods unwrap the phase of adjacent voxels by comparing their phase and determining whether their phase difference is greater than  $\pi$ . Generally, the phase comparison is

performed along regions that are guided based on the reliability/quality of the phase, for example labeling noisy voxels as less reliable. One of the key elements of these methods is the unwrapping of phase starting from the most reliable phase value towards the least reliable phase. This type of method has been widely adopted in QSM. Some examples of these methods are Quality Guided unwrapping (QG) [49], best path unwrapping [51], and ROMEO [51].

The last category of methods considered for this work corresponds to temporal unwrapping. This type of unwrapping resolves wraps caused due to temporal effects, throughout the phase evolution with time. In principle, these techniques can only be applied on phase images at more than one echo time and they only offer voxel-wise unwrapping across time (generally relying on the assumed linear phase evolution and short echo spacing), but they are incapable of resolving phase wraps between neighbor voxels at a fixed time, requiring additional spatial unwrapping or uneven echo spacing [2], [37]. One recent temporal unwrapping method knowns as UMPIRE [52] has overcome some of the limitations of these methods, but it still requires non-uniform echo spacing.

When comparing the three types of algorithms, Laplacian unwrapping corresponds to a relatively easy method to implement and it has the advantage to be robust to noise and phase errors like open fringe lines. But, the downside is that the unwrapped phase retrieved using these methods is generally not quantitatively accurate [4], [49], [50], although a better approximation for the unwrapped phase can be achieved by employing heuristics or adding other sophisticated algorithms to the unwrapping. On the other hand, spatial unwrapping using path-following techniques generally offers greater accuracy than other methods, but they are computationally more demanding and more prone to errors due to noise when compared to Laplacian methods. Additionally, path-following algorithms tend to introduce *post hoc*  $2\pi$  temporal wraps in all the voxels at an echo time. As a result, these methods also need temporal unwrapping or methods specifically design to correct these wraps like THUMPR [50] or the use of phase difference images [2]. Temporal unwrapping is better at unwrapping complex topographies, but it is more vulnerable to noise and generally considerably dependent on the assumption of linear phase evolution with time.

Finally, after all the echoes have been unwrapped, the data can be used to create a frequency shift map, meaning a quantitative map of  $\gamma\Delta B_z(r)$ . Equation 3.7 reflects the linear relation connecting the phase at each echo time and the frequency shift, which in this case would correspond to the slope of the equation. To find the slope of the equation given the heteroskedasticity in the problem (meaning the variability of the phase noise or standard deviation with echo time), a weighted least square fit is optimal [53]. The weights commonly used for the fit are the inverse of the variance  $1/\sigma^2$  of the phase measured at each echo, which for each echo corresponds to the squared SNR of the magnitude image [54]. Thus, the weights used in the solution for the slope can be the inverse square of the magnitude image. Other authors have used different weights like the magnitude image (not squared) [7] or the factor proposed by Wu et al. [55].

Since the weighted least square fit can estimate the slope and intercept of equation 3.7, the phase offset correction can also be calculated during this step. This is an alternative approach to the use of phase difference maps and complex division to eliminate the phase offset (equations 3.10 and 3.11).

## 3.2.3 Background removal

After obtaining the unwrapped phase for each echo and combining all echoes into a single map containing information about the magnetic field shift, it is time to find the magnetic susceptibility distribution that produces these magnetic field perturbations. However, there is a caveat. The magnetic field information is not limited to the field produced by sources exclusively inside the volume-of-interest. Due to the non-local (long-range) nature of magnetic field interactions, demagnetization fields originated outside the volume-of-interest or scanner-related field inhomogeneities seep into the volume-of-interest. These contributions are defined as background magnetic fields and they need to be removed to determine the local field (magnetic field due to sources exclusively inside the volume-of-interest). For this work, the magnetic susceptibility distribution generating the local field will be denoted as  $\chi_L^*$ . The distribution producing the background field will be  $\chi_B^*$ . Additionally, in this thesis, the quantitative maps containing information about the total field (local field + background field) and local field will be denoted as "Total Field Shift" (LFS) and "Local Field Shift" (LFS), respectively. This notation was chosen

to make a clear distinction between the magnetic fields before and after the background removal step.

Most of the background removal algorithms rely on physically and/or mathematically motivated properties of the background field that enable the separation of background fields from local contributions. The principles behind three different algorithms will be presented: Projection onto Dipole Fields (PDF) [56], Sophisticated Harmonic Artifact Reduction for Phase (SHARP) [57], and Laplacian Boundary Value (LBV).

PDF separates magnetic field contributions based on the projection theorem in Hilbert space. According to this theorem, the background susceptibility distribution can be obtained as:

$$\chi_{\mathrm{B}}^* = \operatorname{argmin}_{\chi_{\mathrm{B}}} \| w (\delta B - b_{\chi} * \chi_{\mathrm{B}}) \|_{2}^{2}$$
 3.13

where w is a weight derived from the magnitude images and  $\delta B = \Delta B_z/B_0$  is the measured data. Then, it is possible to estimate the "true" local field as  $B_L^* = \delta B - b_\chi * \chi_B^*$ , where  $B_L^*$  is an element of the space spanned by all the background unit dipole fields (B). B is a space orthogonal to the space spanned by all the local unit dipole fields (L). Thus, PDF relies on B  $\perp$  L and it basically projects the experimental data into the space B [2].

SHARP separates the magnetic fields by imposing the background fields as harmonic fields. A function f is harmonic when it satisfies the Laplace equation, meaning  $\nabla^2 f = 0$ . It also implies that the spherical mean value (SMV) of these functions is the same as the value of the function at the center of the sphere. Denoting the SMV of a function f as  $\langle f \rangle_S = S * f$  (where S is a kernel representing a normalized solid sphere) and the value of the function at the center of the sphere as  $f_0$ , then,  $\langle f \rangle_S = f_0$ . It is possible to use this idea to create an expression only dependent on the non-harmonic contributions of the fields. By subtracting the SMV of the measured field shift from the field shift itself, it is possible to calculate the map  $\delta B'$ :

$$\delta B' = \delta B - S * \delta B = \delta B_{nh} - S * \delta B_{nh}$$
3.14

where  $\delta B_{nh}$  is the non-harmonic contributions in  $\delta B$ . Then, the local field perturbations can be calculated using the kernel ( $\delta - S$ ) for  $\delta$  the Dirac delta function:

$$\delta B_{\rm nh} = (\delta - S) *^{-1} \delta B'$$
 3.15

SHARP has some limitations that have been addressed by variations of this algorithm. The spherical kernel S cannot be used at the boundary of the ROI because the sphere cannot cover regions outside the ROI, leading to the necessity of edge erosion and artifacts at the boundary [58]. To mitigate this effect, V-SHARP uses varying radius kernels, decreasing the radius for regions close to the boundary [59]. Other variations of SHARP use different strategies to improve the calculated LFS. For example, RESHARP adds Tikhonov regularization to enhance small norm features in the calculated local field [60], while E-SHARP extrapolates the calculated field to estimate the values omitted in SHARP close to the boundary [58].

LBV removes the background field by explicitly solving the Laplacian boundary value problem. To define the boundary conditions, the value of the local field at the boundary is assumed to be zero, while the value of the background field is the same as the value of the total field [61]. This approximation is feasible because the background field is generally one or two orders of magnitude greater than the local field [2].

Other algorithms for background removal are discussed and compared in [58]. From the algorithms presented in that paper, one notable algorithm is HARPERELLA, since it performs unwrapping and background removal simultaneously [62].

All the algorithms mentioned above separate the local and background fields by exploiting some mathematical and/or physical properties of these fields. The properties used in each case are rather different, which raises an important question regarding the uniqueness of the separability of the fields and the accuracy of the calculated local field. As discussed in [58], it is impossible to uniquely separate the two categories of magnetic fields without prior assumptions. Without these assumptions, it cannot be guaranteed that a background field would not be produced by an internal susceptibility distribution or inversely, an internal field produced by susceptibility placed outside the volume-of-interest. The use of additional assumptions allows a unique separation of the fields.

However, a unique separation does not ensure the estimation of the "correct" local field. For example, orthogonality breaks at regions close to the boundary of the volume-of-interest. Thus, the field obtained in these regions would have some degree of contamination from background fields erroneously considered as local fields. Although the consequences of these spurious fields on the final susceptibility map are not entirely clear, since it is possible that the dipole inversion technique corrects (to some degree) the erroneously interpreted information during background field removal [58]. On the other hand, assuming the harmonic nature of background fields and the use of an SMV operation to eliminate the harmonic contributions make it impossible to retrieve information close to the boundary of the ROI. In conclusion, even though a unique separation between background and internal fields is possible thanks to *a priori* assumptions, the uniqueness of the solution is not a guarantee of the accuracy of the estimation of the internal field, especially at regions where the considered physical/mathematical assumptions break.

## 3.2.4 Dipole inversion

After calculating the LFS (i.e., after the phase processing and background removal steps), it is possible to solve the ill-posed inverse problem linked to equation 3.5. There are several ways to handle the inverse problem and to cover every algorithm in the literature is outside the scope of this work. But a general overview of the basic ideas common to many methods will be provided.

Dipole inversion methods can be classified depending on whether the problem is solved in the Fourier space or the image space [2].

Fourier-based solutions (as the name suggests) solve the problem by first subjecting all the LFS information to a Fourier transform like equation 3.5. In Fourier space, a simple inverse filtering solution is not possible since  $FT\{b_{\chi}(r)\}$  is equal to zero in a well-defined region of Fourier space as illustrated in Figure 3.3. One way to get around this obstacle is to regularize the Fourier transform of the dipole kernel [32], [63]. The regularization will have consequences in the amount and type of artifacts present in the final susceptibility map [2]. This approach is called truncated k-space division (TKD).

Regularizing the dipole kernel as done in TKD-type solutions is not the only way to solve the inverse problem in Fourier space. There are other methods that tackle the inverse problem in Fourier space, for example in [64], the dipole inversion is performed by calculating the gradient of the LFS in Fourier space. In another example [65], some regions of Fourier space in the dipole kernel that correspond to vanishingly small regions in Fourier space are excluded from the dipole inversion and then recovered using compressed sensing.

Solutions in the image domain generally consist of iteratively determining a susceptibility distribution that after being forward modeled generates a magnetic field shift close to the one obtained from the experimentally collected data. Moreover, treating the inverse problem as an optimization problem enables the implementation of regularization techniques in the optimization algorithm. Thanks to the regularization, it is possible to explicitly or implicitly add *a priori* information to determine the susceptibility distribution [2]. Among all the methods in this category, the most popular is called Morphology Enabled Dipole Inversion (MEDI). This method exploits the similarity between magnitude images and the spatial distribution of the susceptibility by imposing the same edges from the magnitude image in the susceptibility map while sparsifying the edges that do not coincide between both representations [66].

Other methods do not strictly fit in these two categories. These methods are called hybrid methods [2]. They combine the information in Fourier space and image space. One example of this approach is iterative Susceptibility Weighted Imaging and Mapping (iSWIM). In this case, the regularization of the problematic regions in k-space is iteratively improved using information from a binary mask of predefined high susceptibility regions extracted from the susceptibility map generated in the previous iteration. The binary mask is created by thresholding the susceptibility map available at the beginning of the iterative step. The information extracted from the binary mask is Fourier transformed and used to supply information to the ill-defined conical region in k-space. This approach reduces streaking artifacts since the artifacts are mostly located outside the structures defining the binary mask, thus the values in the conic region in k-space contain no artifact either [67].

There are dipole inversion methods that handle the ill-posed inversion problem by collecting experimental information with the volume-of-interest at different orientations. These methods do not exactly fit in the previously stated categories. Notable examples of these types of methods are Calculation of Susceptibility through Multiple Orientations Sampling (COSMOS) and Susceptibility Tensor Imaging (STI). In COSMOS, by acquiring phase data for at least three different orientations of the volume-of-interest, it is possible to remove the ill-conditioning of the inverse problem. Since the problematic conical surface in k-space will be oriented in different directions for each measurement, it is possible to avoid this problematic region. The regions that are problematic in one measurement become well behave in another measurement due to the change of orientation [2]. On the other hand, STI accounts for anisotropy in the tissue and it enables the measurement of the susceptibility tensor. For this method, the measurements must be performed through (at least) six orientations [2]. Although these techniques solve the theoretical obstacles of solving the inverse problem, they are impractical to implement, especially in a clinical setting.

#### 3.2.5 Direct field inversion methods

Traditional QSM estimates the susceptibility distribution by dividing the inverse problem (after phase unwrapping) into two different steps: background removal and dipole inversion. However, this approach still has some shortcomings that could be improved. First, many of the inaccuracies in the susceptibility map originate in the background removal step. The source of these inaccuracies is the breakdown of most of the mathematical and/or physical assumptions at the boundary of the brain. These limitations hinder the quantification of susceptibility in structures like the cortical region of the brain or the superior sagittal sinus [6]. Second, the separation of the process into two steps results in error propagation from the background removal to the dipole inversion. Error propagation can have a significant effect on the final susceptibility map depending on the selected dipole inversion technique, since these present various degrees of sensitivity to errors in the input field [2]. Finally, due to large susceptibility variations in the brain, susceptibility maps often present streaking artifacts. Alternatives to mitigate these artifacts have been proposed in traditional QSM, such as regularization [66] and non-linear susceptibility-to-field relationships [68].

To address the challenges of conventional QSM, methods that jointly perform the background field removal and dipole inversion have been developed. These techniques perform the dipole inversion directly from the TFS map. Chronologically, the first methods created in this category were single-step QSM methods that used TV (Total Variation) and TGV (Total Generalized Variation) regularization [69], [70]. These methods still required explicit removal of the background field by removal of the harmonic contributions in the magnetic field, either by implementation of constraints over the Laplacian of the measured shift phase [69] or SMV filtration (similar to SHARP) [70].

Although TV/TGV methods enable single-step QSM (even obviating the phase unwrapping step), these methods still preserve some of the fundamental problems of conventional QSM [6], [7] like requiring edge erosion or inaccurate susceptibility quantification of the cortical region. Thus, to further improve the susceptibility maps, new methods appeared combining the background removal and the dipole inversion. Three methods will be considered in this thesis and they will be presented in subsections 3.2.5.1–3.2.5.3: Preconditioned Total Field Inversion (pTFI), Least-Norm Quantitative Susceptibility Mapping (LN-QSM), and Regularized Total Field Inversion (TFIR)

The three direct inversion algorithms considered for this project are not the only methods that exist in this category. TV and TGV methods are not included in the "direct inversion methods" category since they also eliminate the phase unwrapping step. Other methods are fast Total Field Inversion (fast TFI) [9] and automated Total Field Inversion (automated TFI) [10]. Fast TFI uses  $L_0$  regularization that relies on the assumption of sparsity of the susceptibility distribution to reduce the number of artifacts and enabling the solution of the inverse problem without requiring background removal. According to the authors of this method, the use of the  $L_0$  norm outperforms pTFI or MEDI [9]. On the other hand, automated TFI is a refinement of pTFI that calculates the preconditioner automatically. These two methods will not be explored any further since they would require to explore two topics that are outside the scope of this thesis: the use of  $L_0$ -norm instead of  $L_1$ -norm and the automation of the calculation of the preconditioner.

## 3.2.5.1 Preconditioned Total Field Inversion (pTFI)

This method uses a preconditioner (or rather a priorconditioner according to [71]) P that assumes that the final susceptibility distribution follows a Gaussian distribution with mean 0 and covariance matrix  $\Gamma$  such that  $PP^H \approx \Gamma$ . the preconditioner increases the convergence speed of the solution when used in conjunction with a conjugate gradient (CG) optimization algorithm [6].

In pTFI, the optimization problem is designed to find the susceptibility distribution  $\chi^* = \chi_L^* + \chi_B^*$ . For a binary mask M representing the volume-of-interest,  $\chi_L^* = M\chi^*$  and  $\chi_B^* = (1 - M)\chi^*$ . Then, the susceptibility distribution can be calculated as (the symbol \* denotes the convolution):

$$\chi^* = \operatorname{argmin}_{\chi} \frac{1}{2} \| w (\delta B - b_{\chi} * \chi) \|_2^2 + \lambda \| M \nabla \chi \|_1$$
 3.16

In this method, total variation (TV) regularization is added using the term  $\lambda ||M\nabla\chi||_1$ . TV regularization promotes smoothness and sparsity in the final susceptibility map [72], [73]. TV regularization also penalizes variations in the gradient of the susceptibility, and it is suitable to deal with piecewise continuous functions, unlike other types of regularization [74]. The variable  $\lambda$  is the regularization parameter for the TV regularization term. In pTFI, this parameter should be chosen such that it minimizes the root-mean-square error (RMSE) in a numerical phantom [6].

The variable w inside the least squares term corresponds to a weighting matrix that accounts for the nonuniform phase noise and is derived from the magnitude images [6], [72]. The entries of the matrix are the inverse of the standard deviation for the values in each voxel of the TFS map [75]. The elements of the matrix w are calculated as [7]:

$$w_{i,j} = \left(\sum_{k} Mag_{i,j,k}^{2}\right)^{1/2} \left(\frac{\sum_{i,j} M_{i,j}}{\sum_{i,j} \left(\sum_{k} Mag_{i,j,k}^{2}\right)^{1/2}}\right)$$
 3.17

The matrix w is the normalized values of the square root of the added (over all echoes) squared values of the voxels in the magnitude image. In equation 3.17, Mag<sub>i,j</sub> are the elements in the matrix

representing the magnitude image in the k-th echo and the sum over k is a sum across echoes.  $M_{i,j}$  are the elements in the matrix representing the binary mask.

By adding a preconditioner to equation 3.16, the argument that minimizes the expression becomes  $\chi = Py$ . Here, P is a matrix that represents the preconditioner and it has entries  $P_{i,j}$ :

$$P_{i,j} = \begin{cases} 1, & i, j \in M \\ P_{B_i}, & i, j \notin M \end{cases}$$
 3.18

The value  $P_B$  (for  $P_B > 1$ ) is an integer value selected ad hoc to reproduce the susceptibility gap between the susceptibility sources in the background and inside the volume-of-interest. The preconditioner assigns high values to the sources in the background [6], and  $P_B = 30$  was determined as the optimal value for QSM in the brain.

## 3.2.5.2 Least-Norm Quantitative Susceptibility Mapping (LN-QSM)

LN-QSM uses Tikhonov regularization to avoid the use of a preconditioner. Tikhonov regularization separates the background field from the local field by exploiting the fact that the background field is approximately two orders of magnitude greater than the local field [7]. In principle, Tikhonov regularization enforces distributions with small values for the susceptibility inside the volume-of-interest enabling the separation of local and background fields. The optimization problem for this method corresponds to the following equation:

$$\chi^* = \operatorname{argmin}_{\chi} \| w (\delta B - b_{\chi} * \chi) \|_{2}^{2} + \lambda_{1} \| M \nabla \chi \|_{1} + \lambda_{2} \| M \chi \|_{2}^{2}$$
 3.19

In this case, regularization is added by the two last terms on the right-hand side of equation 3.19. The  $L_1$ -norm term adds TV regularization (similarly to 3.16) to ensure a smooth solution. The  $L_2$ -norm term adds Tikhonov regularization. The accompanying constants  $\lambda_1$  and  $\lambda_2$  are regularization constants. In [7] the value of  $\lambda_2$  was calculated for brain imaging using the L-curve criterion [75]. On the other hand, the value of  $\lambda_1$  for brain imaging (in the same paper mentioned

before) was selected empirically and in agreement with the literature [76]–[78] about  $L_1$ -norm regularization in QSM.

In the optimization problem established in equation 3.19, the matrixes w and M are the same as in pTFI. The matrix w is a weighting matrix that accounts for the noise in the phase measurements and it is calculated according to 3.17.

## 3.2.5.3 Regularized Total Field Inversion (TFIR)

TFIR uses spatially varying regularization and it is presented by the authors as an improvement over other methods like pTFI and LN-QSM. This method regularizes the problem by adding a weighting matrix built by low-pass filtering a map of R<sub>2</sub>\* estimates obtained from the magnitude data of the mGRE sequence [8]. The susceptibility maps from TFIR reportedly provide a better depiction of regions of high susceptibility, while reducing streaking artifacts.

In TFIR, the optimization problem for calculation of the susceptibility distribution is:

$$\chi^* = \operatorname{argmin}_{\chi} \frac{1}{2} \| w (\delta B - b_{\chi} * \chi) \|_{2}^{2} + \lambda_{1} \| M \nabla \chi \|_{1} + \lambda_{2} \| e^{-|\tau L R_{2}^{*}|} L \chi \|_{2}^{2}$$
 3.20

 $R_2^*$  information is added in the model within the  $L_2$ -norm regularization (the third term in equation 3.20). The use of  $e^{-|\tau L R_2^*|}$  as a weight in the regularization term is justified by the resemblance between the susceptibility values and the point-wise inverse of this weighting matrix [8]. In this case, L is the SMV operator with radius k.  $\tau$  is a constant parameter that modifies the penalty imposed by the  $L_2$ -norm regularization. For brain imaging, k and  $\tau$  were optimized by minimizing the difference between susceptibility maps obtained from COSMOS and TFIR, in a single subject.

The values  $\lambda_1$  and  $\lambda_2$  are regularization parameters. In the original publication of TFIR,  $\lambda_2$  was selected to minimize the difference between susceptibility maps from COSMOS and TFIR results, with the same selection method as for the parameters k and  $\tau$ . The value of  $\lambda_1$  was selected empirically.

Finally, similar to pTFI and LN-QSM, the  $L_1$ -norm regularization corresponds to TV regularization and the matrices M and w are a brain binary mask and a weighting matrix, respectively. The entries of w are calculated as established in 3.17.

## Chapter 4

## Methods and materials

## 4.1 QSM pipeline for conventional QSM and direct inversion methods

For this project, a QSM pipeline capable of producing susceptibility maps using conventional QSM and direct inversion methods was created. A schematical representation of the established QSM pipeline is presented in Figure 4.1. This pipeline corresponds to a modified version of the pipeline proposed in [7].

Since this work was focused exclusively on brain QSM, the first step in the pipeline was to produce a binary brain mask from the magnitude images. The binary mask to define the volume-of-interest for determining the susceptibility distribution was obtained using the Brain Extraction Tool (BET) [79]. This software tool separates whole-head magnitude images into brain and non-brain tissue by first creating a rough mask using histogram-based thresholding. Then, the rough brain/non-brain separation is improved by creating a triangular tessellated sphere centered at the centre of gravity estimated from the initial brain/non-brain thresholding. Finally, each vertex of the sphere is moved toward the brain edge and the new tessellated surface is iteratively modified until achieving a smooth and optimal solution [79]. The BET function is part of the Functional Magnetic Resonance Imaging of the Brain (FMRIB) Software Library (FSL) developed by the FMRIB Analysis group at the University of Oxford. FSL is a set of analysis tools for brain imaging data focused on functional, structural, and diffusion MRI [80], [81].

For the QSM pipeline used in this project, phase offset correction was performed using the first two echoes and implemented before phase unwrapping (as illustrated in Figure 4.1). The phase offset correction was applied to all echo at each echo time and it was calculated as described in section 3.2.2 and based on the methods presented in [42], [58], [82]. After obtaining the phase

offset correction and the binary brain mask, the next step in the pipeline was unwrapping. Phase unwrapping is this work was understood as a two-stage process consisting of spatial phase unwrapping followed by temporal unwrapping (used to correct  $2\pi$  jumps introduced during spatial unwrapping). The implemented spatial unwrapping algorithms were: a local implementation of Laplacian unwrapping denominated as "discrete Laplacian unwrapping" (dLu) in [1], SEGUE [47], and Quality Guided unwrapping QG [49]. THUMPR was used for temporal unwrapping [50]. THUMPR is capable of correcting phase jumps of magnitude  $2n\pi$ , where n is an integer.

After phase unwrapping, all echoes were combined into a single (Total Field Shift) TFS map, shown in Figure 4.1. The echo combination was performed using a weighted least-squares fit with weights corresponding to the inverse of the variance of the phase measured at each echo, which is proportional to the SNR of the magnitude image for each echo [54]. Using the fitting residuals, a reliability mask was created to exclude voxels with a non-linear temporal evolution, which may be induced by flow artifacts (turbulent flow), partial volume effects, and/or excessive noise levels [3]. To create the reliability map, the map of fitting residuals was first smoothed (Gaussian smoothing). Then, every voxel corresponding to a value greater than an ad hoc threshold (selected according to the pipeline used in [7]) was excluded from subsequent steps in the pipeline.

From the magnitude images, two additional pieces of information were derived to use in conventional QSM and direct inversion. First, a weighting matrix w was calculated from the magnitude information to account for the nonuniform phase noise. The entries of this matrix were calculated according to relation 3.17. Second, a mask of cerebrospinal fluid (CSF) voxels was also derived from the magnitude information. The CSF mask was used to set the zero reference of the susceptibility distribution calculated by the QSM pipeline. The CSF mask was calculated by first determining the R<sub>2</sub> map from the magnitude images obtained from the mGRE sequence. The R<sub>2</sub> map was calculated using an algorithm for fast mono-exponential fitting based on Auto-Regression on Linear Operations of data (ARLO) [83]. Subsequently, the R<sub>2</sub> map was used to estimate the CSF mask using the CSF extraction tool provided in the MEDI toolbox [72]. CSF is not the only option for the reference tissue in QSM [84], but it was selected in this case as the most practical approach as a suitable reference tissue for QSM [85], [86].

The final steps in the pipeline consisted in estimation of the susceptibility distribution of the volume-of-interest (brain) either by background removal and dipole inversion (conventional QSM) or by direct field inversion. For this work, the background removal techniques considered were RESHARP [60], PDF [56], and LBV [61]. All of these background removal techniques were paired with two different dipole inversion algorithms, iSWIM [67] and MEDI+0 [85]. These dipole inversion techniques were selected to represent methods that operate in the Fourier and image domain, respectively. Moreover, MEDI+0 was selected since it uses L<sub>1</sub> regularization in the same fashion as the MEDI version presented in [66], but it also automatically zero-referenced the obtained susceptibility map using CSF as a reference, which is coherent with the selected reference for this work. On the other hand, the direct inversion methods selected here were pTFI [6], preconditioned LN-QSM (pLN-QSM) [7], and TFIR [8]. LN-QSM was implemented using the code made freely available by the authors of the method<sup>1</sup>. A preconditioner (as specified in equation 3.18) was added to the method for pLN-QSM. The addition of a preconditioner to LN-QSM is suggested in the original pipeline made available by the authors of the method, but it is not discussed in the original publication [7]. pTFI and TFIR were included in the pipeline via local implementations according to the theory detailed in the original publications for each method.

<sup>&</sup>lt;sup>1</sup> Repository for the original implementation of LN-QSM: https://github.com/sunhongfu/QSM

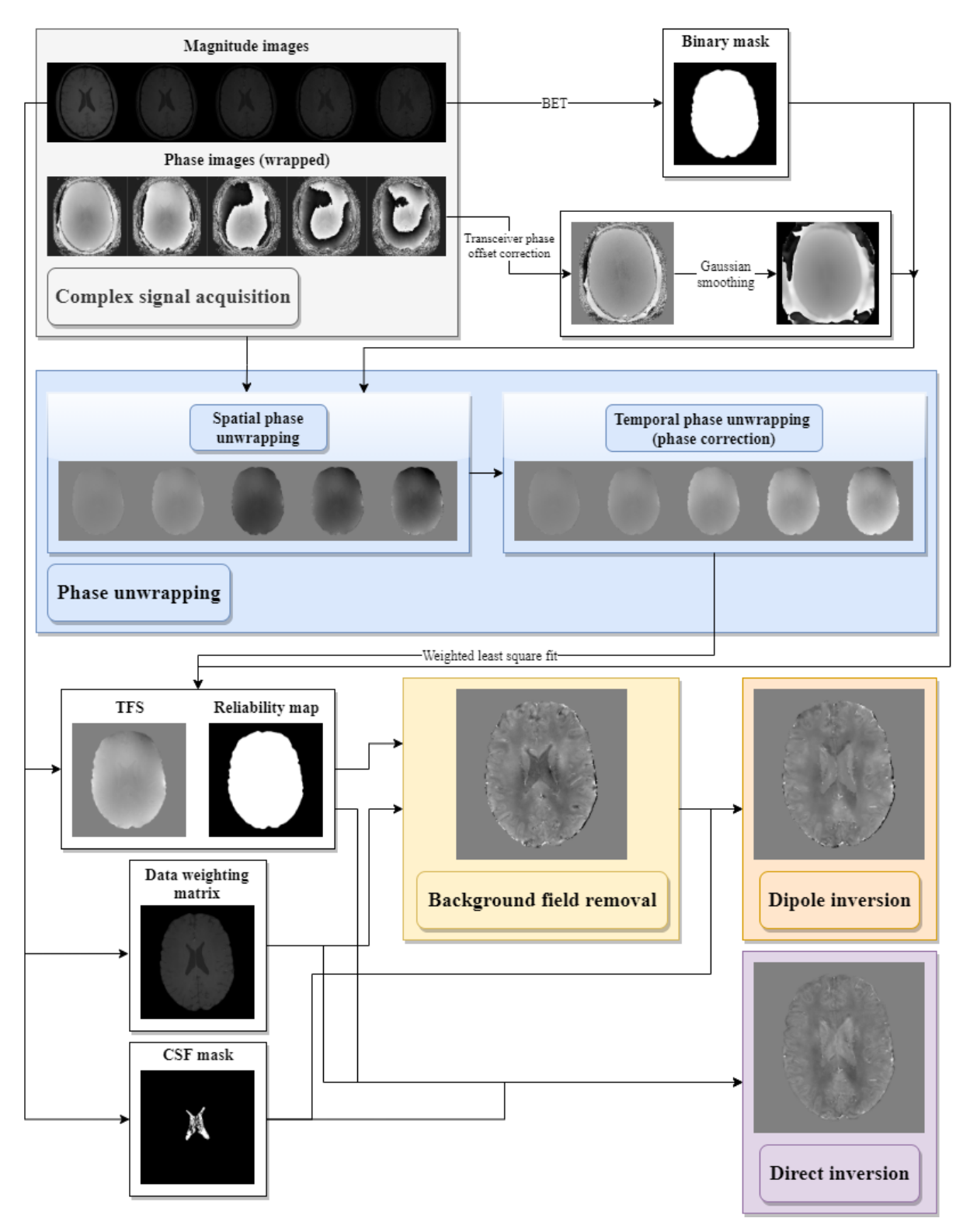


Figure 4.1: Schematic representation of the QSM pipeline created for this work. The pipeline is a modified version of the pipeline used in [7]. The phase unwrapping was performed by using discrete Laplacian unwrapping, SEGUE, or QG for spatial unwrapping, and THUMPR for

temporal unwrapping (temporal phase correction). The background field removal techniques were: SHARP, PDF, and LBV. These techniques were paired with two different dipole inversion algorithms: iSWIM and MEDI+0. The direct field inversion techniques implemented were pLN-QSM, pTFI, and TFIR.

## 4.2 Evaluation of susceptibility maps using numerical simulations

## 4.2.1 Designing a brain numerical model for QSM

To study direct inversion methods, two numerical models of the head were created. These numerical models were used as input for the pipeline described in section 4.1. Both numerical models were composed of two different parts, a numerical model of the head and a numerical model of the brain, as illustrated in Figure 4.2. The numerical model of the head (Figure 4.2 b)) contained regions representing scalp (soft tissue), skull, and air. The numerical model of the brain (Figure 4.2 c) and d)) was placed inside the head model. The difference between the two numerical models, denoted as "model A" and "model B", resided in the structures added inside the brain. Model A only contained regions corresponding to gray matter (GM), white matter (WM), and cerebrospinal fluid (CSF). The susceptibility of each region was assigned according to Table 4.1 [87]. In comparison with Model A, model B added deep gray matter structures inside the brain. The structures added to model B were the thalamus (TH), caudate nucleus (CN), putamen (PU), and globus pallidus (GP). In these regions of the brain (TH, CN, PU, and GP), the susceptibility values in model A were replaced by the values in Table 4.2 [88].

The structures in the head model were used to generate a realistic background field model for the brain, as done in [89]. To create the background field, air pockets were considered in the model to reproduce high susceptibility changes produced by the presence of structures like frontal sinus, sphenoid sinus, nasal cavity, and ear canal.

To create the head and brain numerical models a T1-weighted (T1w) dataset (Figure 4.2 a)) was used as a template. This dataset was acquired from a healthy male volunteer (43 years old) who gave written informed consent (Resarch Ethics Board of the RI-MUHC). To perform the

measurements, a Siemens Prisma 3T MRI scanner with a 20 channel head/neck coil was used. To obtain the T1w dataset, a magnetization-prepared rapid gradient echo (MP-RAGE) sequence was used with a voxel size of  $0.879 \times 0.879 \times 0.9$  mm<sup>3</sup> (repetition time TR = 2300 ms, echo time TE = 2.33 ms, inversion time TI = 900 ms, flip angle FA = 8°, bandwidth BW = 200 Hz/pixel, matrix size  $256 \times 256 \times 192$ ). This dataset was used for automatic tissue segmentation.

An mGRE sequence was used to obtain magnitude and phase data for QSM. The sequence parameters for this acquisition were TR = 50 ms, time for the first echo TE<sub>0</sub> = 4.9 ms, echo spacing  $\Delta$ TE = 5.4 ms, number of echoes = 5, flip angle FA = 15°, readout bandwidth BW = 470 Hz/pixel, voxel size  $0.8 \times 0.8 \times 1.5$  mm<sup>3</sup>, and matrix size  $288 \times 288 \times 104$ . Further detail about the experimental data collection for this project are presented in section 4.3.1.

Before image registration, the voxel size of the magnitude and phase images of the mGRE sequence was transformed from  $0.8 \times 0.8 \times 1.5 \text{ mm}^3$  to  $0.78 \times 0.78 \times 0.78 \text{ mm}^3$  isotropic voxel size by zero padding the complex data in Fourier space. The size of the padding was established by modifying the matrix size and voxel size while keeping the size of the field of view (FOV) constant. The size of the padding along the three dimensions was given by integer numbers that are calculated after rounding the results from the operation  $VS \odot MS/min(VS) - MS$ , where VS and MS are three-dimensional vector containing the voxel size and matrix size and  $\odot$  represents the point-wise product between the elements of the matrices. In a similar way, the voxel size of the T1w dataset was modified to match the voxel size  $0.78 \times 0.78 \times 0.78 \text{ mm}^3$ .

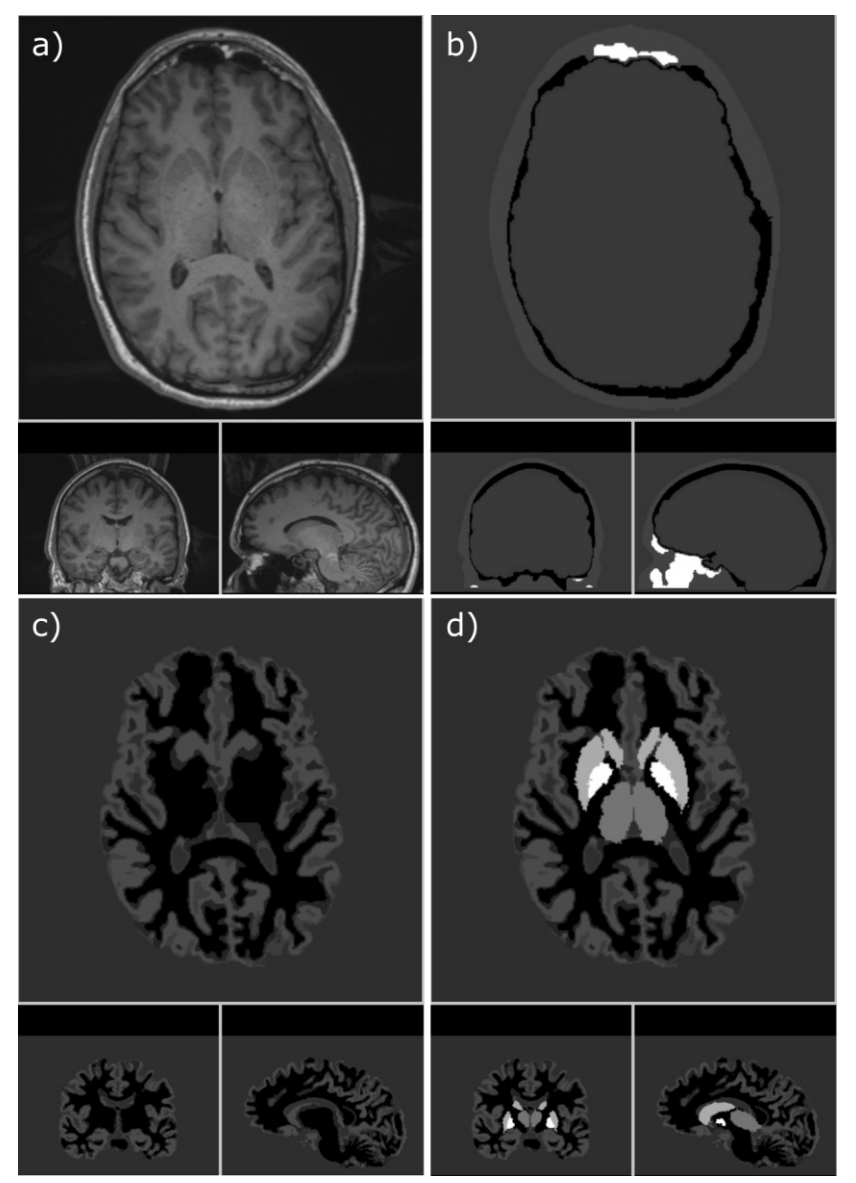


Figure 4.2: Axial, sagittal, and coronal views of the T1-weighted dataset used to create numerical models, head numerical model, and brain numerical models A and B. a) T1w brain image used as a template to create the numerical brain models. b) Head numerical model without brain parenchyma, including air pockets for the frontal sinus, sphenoid sinus, nasal cavity, and ear canal. c) Numerical model A of the brain containing grey matter (GM), white matter (WM), and CSF. d) Numerical model B, containing the structures in model A plus deep gray matter structures for the thalamus (TH), caudate nucleus (CN), putamen (PU), and globus pallidus (GP). Numerical brain models A and B are placed in the skull model to create a realistic background in simulations.

Image registration between the magnitude image of the mGRE sequence and the T1w dataset was performed using 3D 12 degrees of freedom affine registration in MATLAB with the function

imregister (which uses to intensity-based image registration), setting the initial step size (initial radius) of the optimizer to  $1.78 \times 10^{-3}$  and the number of iterations to 400. These two parameters were selected by gradually modifying them until good visual alignment was observed between the two datasets in bony structures and gyri of the brain. The result of image registration is illustrated in Figure 4.3, showing a slice of both datasets in three planes after image registration. The function imregister performs image registration using an algorithm based on Pyramiding affine registration [90] and a bilinear optimization.

Following image registration, the T1w dataset was used for automatic tissue classification. BrainSuite software was used for this purpose [91], [92]. BrainSuite was selected because it is extremely user friendly, it has a very intuitive GUI, its applications are well documented, it allows for manual corrections of many of the results obtained with the software and there are several video tutorials explaining different aspects of the software (from basic to advanced applications).

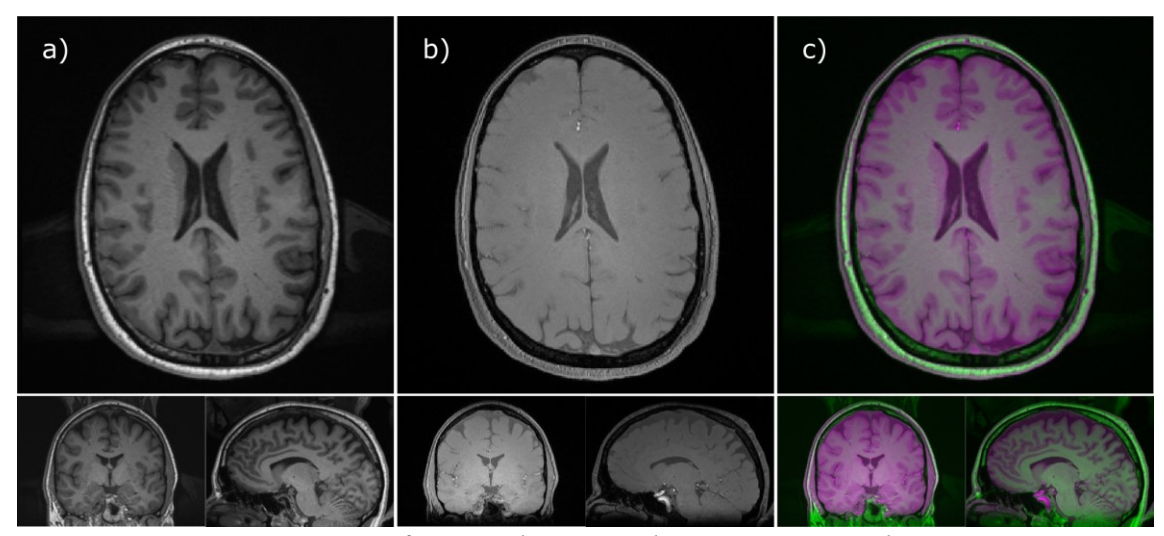


Figure 4.3: Image registration for T1w dataset and m GRE magnitude image using MATLAB. a) and b) are axial, sagittal, and coronal slices of the T1w image and magnitude image of the mGRE sequence, respectively, after registration. c) presents the slices overlapped.

To create the head model, the skull stripping tool of BrainSuite was used to delimit the boundary between the brain and the skull (7 diffusion iterations, diffusion constant 26.042, edge constant 0.64, and erosion size 2). Subsequently, the mask generated in this step was manually corrected in regions where the brain and skull were incorrectly separated. The next step to create the model

was to use the skull and scalp tool to automatically classify the structures in the T1w image as scalp/soft tissue, skull/bone, air, CSF, and brain tissue. Some regions that were incorrectly flagged when compared with the magnitude image or altered due to artifacts were manually corrected. After these processing steps, BrainSuite generated a NIfTI<sup>2</sup> file with tags representing each of the structures previously mentioned. These files were imported into MATLAB and the tag values generated by BrainSuite were replaced by the corresponding susceptibility values. The tags used by BrainSuite and the susceptibility values assigned in the model are presented in Table 4.1. The susceptibility values were retrieved from literature [87]. An illustration of the tissue classification for the head model is presented in Figure 4.4.

Table 4.1: BrainSuite tags and susceptibility values used to identify regions in the head and brain tissue. The susceptibility values were retrieved from [87]. The susceptibility values for regions containing a mixture of components were determined as the average values of the susceptibility of the individual components.

Structure	BrainSuite tag	Susceptibility [ppm]
Air	0	9.4
Scalp/soft tissue	16	0.6
Skull/bone	17	-2.5
CSF	18	0
GM	2	0.02
WM	3	-0.033
GM/CSF	4	0.01
GM/WM	5	-0.006

<sup>2</sup> NIfTI data format details, source code, and documentation: <a href="https://nifti.nimh.nih.gov/">https://nifti.nimh.nih.gov/</a>

Table 4.2: BrainSuite tags and susceptibility values for deep grey matter structures included in model B. The values presented in the table were collected from [84] and correspond to the average values for each structure using CSF as the zero reference.

Structure	BrainSuite tag	Susceptibility [ppm]
Right thalamus	640	-0.007
Left thalamus	641	
Right caudate nucleus	612	0.029
Left caudate nucleus	613	
Right putamen	614	0.026
Left putamen	615	
Right globus pallidus	616	0.104
Left globus pallidus	617	

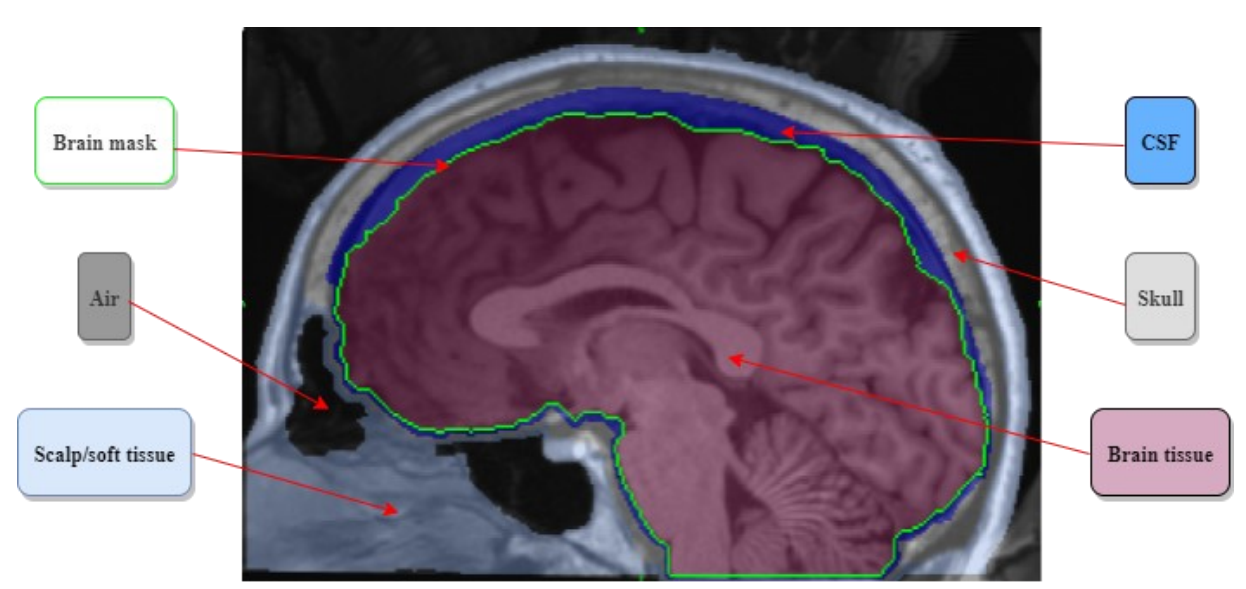


Figure 4.4: Illustration of tissue classification for the numerical head model using BrainSuite.

To create numerical brain model A, the T1w dataset was processed using BrainSuite. After using the skull stripping and skull/scalp tools, the tissue inside the brain was classified first by applying a non-uniformity correction using Bias Field Corrector (BFC) followed by the tissue classification tool using the Partial Volume Classifier. Non-uniformity correction was used to mitigate intensity variations caused in the image due to transmit/receive fields imperfections and artifacts due to

magnetic susceptibility. The BFC parameters were selected automatically using the iterative mode. The Partial Volume Classifier was used to classify the brain tissue into GM, WM, CSF, and regions containing a mixture of these three regions. The mixtures considered in the model were GM/CSF and GM/WM. In a similar fashion to the head model, the output of BrainSuite was imported to MATLAB and the tags for each region were replaced by the susceptibility values. These values are presented in Table 4.1. The value of the susceptibility in the regions where there is a mix of components was established as the average value of the susceptibility of each component since the magnetic susceptibility is an additive property.

To create numerical brain model B, model A was used in conjunction with the cortical surface extraction and surface/volume pipelines in Brainsuite. The cortical surface extraction pipeline was used to define the cortical region of the brain and to create a cortical mask for models A and B. The surface/volume pipeline registered the input MRI dataset to a brain atlas where the structures were already classified and labeled. The output of this tool was a NIfTI file containing the input dataset segmented into different cortical and subcortical regions. The surface/volume pipeline was used to include deep gray matter structures in model B in the form of TH, CN, PU, and GP and to create masks for measuring the susceptibility in anatomical ROIs for these regions. The structures included in model B and their susceptibility values are presented in Table 4.2. Deep grey matter structures that are also high susceptibility sources such as the substantia nigra and red nucleus were not included in the model since BrainSuite cannot automatically segment them.

All steps in the cortical surface extraction pipeline were executed either using an iterative solver (when available) or using the defaults values for each step. Subsequently, the results for the cerebral mask and the inner and pial surfaces were inspected for major errors. When inspecting the inner and pial surfaces, two aspects were considered to identify errors in the definition of these surfaces. 1) Appropriate delineation between grey and white matter. 2) Discontinuities or gaps in gyri that are challenging to depict accurately due to their thickness or to their location near regions of possible signal dropout. The first aspect was assessed by inspecting coronal slices and verifying that the gray/white junction determined by BrainSuite coincided with the observable separation in each slice of the T1w image. The second aspect was evaluated by looking at obvious missing gaps or discontinuities in the parahippocampal gyrus, gyrus rectus, and superior temporal gyrus, which

is where the most common errors occur due to their shape and size [91], [92]. Good agreement between the observable and calculated junctions was observed and no major discontinuities in the gyri were found.

After importing the .nii files to MATLAB and replacing the susceptibility values, the brain models A and B were placed inside the head model. Then, the susceptibility values were used to forward model the corresponding magnetic field shift according to equation 3.5. Since the numerical simulation was used for QSM considering the brain as the volume-of-interest, the field produced by the susceptibility distribution in the head model was assumed to be the background field. Meanwhile, the field that was produced by the susceptibility distribution of the brain model was assumed as the local field.

After forward modeling the magnetic field shift produced by the susceptibility distribution, this value was used in each voxel as the slope in equation 3.7 to generate the phase evolution as a function of echo time (assuming a linear relationship). The time-independent phase contribution in equation 3.7 was assumed to be zero, and no phase offset was added to the model. 5 echoes were generated using the same echo times as the magnitude image in the mGRE sequence describe before (time for the first echo  $TE_0 = 4.9$  ms, echo spacing  $\Delta TE = 5.4$  ms). The complex signal for each echo time and each voxel was composed of the magnitude information from the mGRE sequence (for a specific echo time and voxel) combined with the simulated phase (at the same echo time and voxel considered for the magnitude data). The wrapped phase was finally obtained as the phase of the complex signal.

Noise was added to the model to enable the study of QSM with varying levels of SNR. The noise was included in the model by adding white gaussian noise to the real and imaginary parts of the complex signal. The noise at each echo was included by creating a matrix (of the same size as the matrix containing the complex signal) of normally distributed random values using the random function in Matlab. The standard deviation of the noise distribution was set by multiplying the noise matric by the mean value of the magnitude image in the first echo divided by a fixed SNR value. The values considered for SNR were 10, 20, 40, and 60. The minimum value of 10 was

selected since the BET function failed to create a binary brain mask for the numerical model with lower SNR.

All the experiments described below were performed using model A and model B. The goal behind model A was to determine if the presence of high susceptibility sources affected the measurement of the susceptibility at the cortical region of the brain, by removing them. Thus, the results from both models will be presented when showing the measured susceptibility in anatomically relevant ROIs. For all other cases, only the results for the more realistic model B will be shown since only negligible variations between the results for both models were observed for unwrapping, background removal, and the appearance of the susceptibility maps (except for the presence of deep gray matter structures).

## 4.2.2 Comparison of phase unwrapping algorithms

In the numerical models, the unwrapped phase was studied after spatial and temporal unwrapping, i.e. after applying THUMPR. Two criteria were contemplated to select the spatial unwrapping algorithms. 1) The inclusion of path-following unwrapping techniques, considered as the most accurate, and of Laplacian unwrapping, considered as the most robust approach to noise and a large number of wraps [93]. 2) The selected methods were based on previous work done in our research group for conventional QSM [50]. The objective of the unwrapping comparison was to determine if the techniques that performed well in conventional QSM also performed well with direct inversion methods.

To assess the performance of the three unwrapping algorithms considered for this project, the unwrapped phase was studied and compared with the ground truth. The comparison was done in axial slices, one-dimensional profiles across axial slices, and using maximum intensity projection (MIP) difference maps. Additionally, the RMSE metric was used as a global quantitative metric to represent the agreement between the calculated unwrapped phase and the true phase. For each unwrapping technique, the accuracy of the technique and the source of errors for the unwrapped phase was determined. The performance of the algorithms was studied in the noiseless model and for varying levels of SNR.

The MIP difference maps were calculated by taking the absolute value of the voxel-wise difference between the ground truth and the calculated unwrapped phase. Then, the maximum values were projected onto a plane parallel to an axial slice (superior/inferior view) or parallel to a sagittal slice (lateral view). On the other hand, the RMSE value was calculated as:

$$RMSE = \frac{\left\| \mathbf{x}_{c} - \mathbf{x}_{g} \right\|_{2}}{\sqrt{n}}$$
4.1

 $x_c$  represents the 3D matrix containing the calculated unwrapped phase, while  $x_g$  is the ground truth phase. The  $L_2$ -norm in the formula is the Frobenius norm. n is the number of voxels in the matrices.

# 4.2.3 Interaction between the unwrapping and the background removal techniques in conventional QSM

Local field shift (LFS) maps were created for the numerical simulations to study the performance for every possible combination of the selected unwrapping (dLu, QG, and SEGUE) and background removal (PDF, RESHARP, and LBV) techniques. The three background removal techniques were selected to cover as many as possible of the physical/mathematical principles behind the operation of background removal algorithms [2], [58]. The LFS maps were compared to the ground truth using difference maps and the RMSE metric (equation 4.1). The difference maps were used to qualitatively identify spurious local fields and errors at the edge of the brain. The RMSE was calculated using three different masks to evaluate the performance of the techniques in an eroded brain mask (which roughly represents the performance of the techniques for subcortical structures), at the edges of the brain (defined by the volume that was excluded from the eroded mask), and in the whole brain (using the original binary brain mask). These masks were designed to quantitatively determine the accuracy of background removal at the edge of the brain, where the assumptions in PDF and LVB break down. Also, the three masks was were used to compare PDF and LBV with RESHARP, since this last technique requires edge erosion. The eroded mask for comparison was selected according to the erosion required in RESHARP (6)

voxels for numerical model B). The RMSE values for the edge of the brain and the whole brain were not calculated for RESHARP.

MIP difference maps were created comparing the calculated LFS maps and the ground truth from the numerical model. These maps were also used to show error propagation between the unwrapping to the background removal step

## 4.2.4 Evaluation of susceptibility maps using numerical simulations

## 4.2.4.1 Unwrapping and background removal in QSM

After finding the best background removal technique for conventional QSM, susceptibility maps were created for numerical model B using MEDI+0, iSWIM, pTFI, pLN-QSM, and TFIR, and all unwrapping techniques. The reasons behind using all unwrapping techniques were two-fold. First, when studying the best background removal technique for the numerical model, similar performance was observed for the methods paired with SEGUE and QG, thus it was not possible at that stage to establish the best unwrapping technique for comparison. Second, it was to verify that the unwrapping technique that performs better in conventional QSM [49], [50] was also the best option for direct inversion methods.

From the three direct inversion techniques considered for this project, pTFI and TFIR were local implementations created for this project, while LN-QSM was implemented using the code provided by the authors of the method. However, it was not possible to reproduce the results in [7] using the freely available code. The addition of a preconditioner (as suggested in pTFI and showed in equation 3.18) significantly improved the quality of the susceptibility maps obtained with LN-QSM. This method with a preconditioner was named preconditioned LN-QSM (pLN-QSM) and was used in all cases instead of LN-QSM. The use of a preconditioner is justified in the discussion section.

To solve the inverse problem in the three direct inversion methods, a non-linear conjugate gradient method was used. The initial distribution for the solver was a zero matrix. The iteration in the case

of pLN-QSM was stopped when one of two conditions was met: either the norm of the change in the solution was less than 0.01% of the norm of the current solution (the default value in the original LN-QSM code [7]) or the number of iterations exceeded 200. The default value for the maximum number of iterations in the original code was set to 500, even though the paper describing the method [7] established a limit of 200. The value of 200 in this work was selected first to emulate the value established in the cited paper, and because the results obtained with numerical simulations showed minimal improvement in RMSE beyond 150-200 iterations, when comparing the ground truth with the estimated susceptibility distribution. The same conditions to stop the conjugate gradient solver were used for the other two methods since comparable quality susceptibility maps and reconstruction times to pLN-QSM were achieved in both cases with this threshold.

The reconstruction parameters selected for direct inversion methods were as suggested by the authors for healthy brain QSM. For pTFI, parameters were  $P_B = 30$  and  $\lambda = 8 \times 10^{-4}$  [6]. For pLN-QSM, parameters were  $\lambda_1 = 1 \times 10^{-4}$  and  $\lambda_2 = 1 \times 10^{-3}$  as in LN-QSM [7], with an extra preconditioner with  $P_B = 30$ . For TFIR, parameters were  $\lambda_1 = 1 \times 10^{-3}$ ,  $\lambda_2 = 1 \times 10^{-1}$ , k = 2,  $\tau = 0.05$  [8].

The comparison of the impact of unwrapping on susceptibility maps was performed using the RMSE metric, a visual assessment of artifacts in the maps, and MIP difference maps. With this information, it was possible to establish the best unwrapping technique for direct inversion methods.

## 4.2.4.2 Comparison of conventional QSM and direct field inversion methods

To understand the advantages or disadvantages of direct inversion methods over conventional QSM, a qualitative assessment of the artifacts in the susceptibility maps of direct inversion methods was done (using only the best unwrapping technique) by comparison with conventional QSM. The comparison of the results was performed in representative axial and sagittal slices and one-dimensional profiles through the selected axial slice.

MIP difference maps comparing the LFS maps obtained from conventional QSM after background removal and the LFS map produced after forward modeling the susceptibility distribution obtained from the direct inversion method (pTFI, pLN-QSM, and TFIR) were created. These maps were used to show the reduced error in the local field estimated by direct inversion methods when compared with conventional QSM.

#### 4.2.4.3 Decoding the operation of direct inversion methods

To provide insight into the mechanisms behind the operation of direct inversion methods, the estimated susceptibility distributions calculated by direct inversion methods inside and outside the volume-of-interest (in this case the brain, defined by the binary mask) in the numerical models were used to calculate the local (LFS) and background fields. The local field was derived from the susceptibility distribution estimated inside the brain. The background field was considered as the field produced by the susceptibility distribution estimated outside the brain and multiplied by a preconditioner (for the methods which consider the use of a preconditioner). The calculated local and background fields were compared to the ground truth obtained from the numerical model. The comparison of these two fields was done to establish how the estimated susceptibility distribution in direct inversion methods contains information about the background field, while also generating a local field coherent with the modeled susceptibility distribution (in other words, a magnetic field that would allow accurate estimation of the susceptibility distribution inside the volume-of-interest). The metric for comparing the local and background magnetic field contributions with their respective ground truths was the RMSE.

#### 4.2.4.4 Measurement of the susceptibility in anatomical ROIs

To understand how QSM depicts the susceptibility in specific anatomical ROIs, the true discrete susceptibility distribution in numerical model B was compared with the estimated susceptibility distribution from conventional QSM and direct inversion methods, using histograms. Numerical model B is a set of discrete regions that represent structures inside the brain, and the histogram of its susceptibility distribution is a set of discrete bars representing the number of voxels and susceptibility of each structure. A good agreement between the ground truth and the estimated

susceptibility distribution from the selected QSM method should feature a multimodal distribution with peaks in the same positions as the discrete values in the ground truth. This was investigated for MEDI+0, iSWIM, pTFI, pLN-QSM, and TFIR.

A quantitative analysis of the susceptibility values in deep gray matter structures (TH, CN, PU, and, GP) and the cortical region of the brain was performed by measuring the mean and standard deviation of the susceptibility in ROIs representing these structures, in the numerical models. The values in the cortex were measured in models A and B. The susceptibility in deep gray matter structures was measured in model B. The measurement in each region was performed using the mask generated during the creation of the numerical models (subsection 4.2.1). The mean values measured in ROIs for the susceptibility distributions calculated by MEDI+0, iSWIM, pTFI, pLN-QSM, and TFIR were compared with the ground truth using the percentage error as a measurement of accuracy.

$$Percentage\ error\ [\%] = \frac{|Measured\ value\ -\ Theoretical\ value|}{Theoretical\ value} \times 100 \quad 4.2$$

#### 4.2.4.5 Susceptibility estimation for varying SNR

The performance of direct inversion methods and conventional QSM with varying levels of SNR was evaluated in numerical model B by analyzing the artifacts in the susceptibility maps. For each value of SNR (10, 20, 40, 60) susceptibility maps were created for MEDI+0, iSWIM, pTFI, pLN-QSM, and TFIR. Reconstruction parameters listed in subsection 4.2.4.1 were used. The susceptibility distributions in each map inside the cortex and GP were also studied using box charts to analyze the change due to SNR in the distributions in the cortical brain and the deep gray matter structure with the highest susceptibility value included in the numerical model.

## 4.3 Evaluation of susceptibility maps using in vivo datasets

#### 4.3.1 In vivo data acquisition

In vivo datasets were collected from five healthy volunteers (three males aged 26, 27, and 43, and two females aged 25 and 27). Informed consent under the approval from the Research Ethics Board of the McGill University Health Center (MUHC) was obtained for all the volunteers. Two different MRI scanners were used to collect information: a MAGNETOM Prisma 3T manufactured by Siemens Healthineers (Scanner I) and an Ingenia 3T manufactured by Philips Healthcare (Scanner II). For head imaging, the scanners were paired with a 20-channel head coil in the case of Scanner I, while for Scanner II a 15-channel was used. Scanners I and II had slightly different centre frequencies  $f_0$ , which were 123.258 MHz and 127.765 MHz, respectively.

The difference in centre frequency between Scanners I and II, due to a difference in main magnetic field, was accounted for in the QSM pipeline. The magnitude of the magnetic field is calculated as  $B_0 = 2\pi f_0/\gamma$ , where  $f_0$  is the centre frequency in Hz. The use of two different scanners implies possible differences in shimming for the data collected in each scanner. Differences in  $B_0$  field homogeneity and shimming alter the effect that air/tissue interfaces have over the QSM results [94], [95]. The differences in QSM arise due to the variability in the separation between background and local fields due to the shimming near air cavities [95]. The variability introduced due to the use of different scanners when studying anatomical ROIs is not significantly larger to the variability introduced when using the same scanner for different measurements (with the same acquisition parameters) [95]. To avoid the introduction of bias due to the variability between datasets when assessing the performance of the considered techniques, the datasets were not directly compared. Results for different datasets were only contrasted when there were qualitatively noticeable differences in the appearance of the susceptibility maps or when a technique failed in a particular dataset.

For all acquisitions, a 3D mGRE sequence was used to collect magnitude and phase information. Additionally, for three volunteers imaged in Scanner I, T1w datasets were collected using the MP-RAGE sequence (described in section 4.2.1). For all acquisitions, flow compensation and unipolar

readout gradients were employed. In the datasets acquired with Scanner II, parallel imaging (SENSE) was used (acceleration factor 2.4 and 1.5 in the phase encode directions). The sequence parameters are summarized in Table 4.3 and

Table 4.4 for mGRE and MP-RAGE protocols, respectively. The collected datasets were labeled by combining a letter, representing the volunteer, with a number representing the dataset from the specified volunteer.

Table 4.3: 3D mGRE sequence parameters for collecting complex data for QSM experiments. The letter in the name of the dataset denotes the volunteer. Datasets B1, C3, and E1 were obtained using Scanner I. All other datasets were collected using Scanner II. All acquisitions were designed to have five echoes, except B3 which had seven echoes.

Dataset	TR	$TE_0$	$\Delta TE$	FA	BW	Voxel size	Matrix size
	[ms]	[ms]	[ms]	[°]	$\left[\frac{Hz}{pixel}\right]$	[mm³]	[voxel]
A1	51	4.9	5.4	20	483	$0.60 \times 0.60 \times 1.00$	$336 \times 336 \times 155$
A2	51	5.0	5.4	20	322	$0.70 \times 0.70 \times 1.00$	$288 \times 288 \times 155$
A3	51	5.6	6.1	20	241	$0.70 \times 0.70 \times 1.00$	$288 \times 288 \times 155$
B1	50	4.9	5.4	15	470	$0.80 \times 0.80 \times 1.50$	$288 \times 288 \times 104$
B2	56	4.5	5.4	20	477	$0.54 \times 0.54 \times 1.00$	$400 \times 400 \times 168$
В3	56	4.5	5.4	20	482	$0.60 \times 0.60 \times 1.00$	$336 \times 336 \times 162$
C1	51	4.9	5.4	20	483	$0.60 \times 0.60 \times 1.00$	$336 \times 336 \times 162$
C2	51	5.0	5.4	20	322	$0.70 \times 0.70 \times 1.00$	$288 \times 288 \times 162$
С3	60	8.0	8.0	20	465	$1.00 \times 1.00 \times 1.00$	$224 \times 186 \times 176$
D1	51	5.4	5.5	20	280	$0.53 \times 0.53 \times 1.00$	$400 \times 400 \times 168$
D2	51	5.4	5.5	20	481	$0.55 \times 0.55 \times 1.00$	$384 \times 384 \times 168$
D3	51	5.4	5.5	20	653	$0.55 \times 0.55 \times 1.00$	$384 \times 384 \times 168$
E1	50	5.0	5.0	20	465	$1.00 \times 1.00 \times 1.00$	224 × 186 × 176

Table 4.4: MP-RAGE sequence parameters for T1w images. These datasets were collected with the corresponding 3D mGRE sequences using Scanner I.

Dataset	TR	TE	TI	FA	BW	Voxel size	Matrix size
	[ms]	[ms]	[ms]	[°]	$\left[\frac{Hz}{pixel}\right]$	[mm <sup>3</sup> ]	[voxel]
B1	2300	2.33	900	8	200	$0.879 \times 0.879 \times 0.9$	$256 \times 256 \times 192$
С3	2300	2.26	900	8	200	$1.0 \times 1.0 \times 1.0$	$192 \times 256 \times 256$
E1	2300	2.26	900	8	200	$1.0 \times 1.0 \times 1.0$	192 × 256 × 256

All datasets excluding C3 and E1 were originally collected for previous work in the MRI Methods Group in the McGill Medical Physics Unit [50].

#### 4.3.2 Unwrapping algorithms comparison

Similar to the analysis done with numerical simulations, the performance of the unwrapping technique in the measured datasets was done studying the unwrapped phase in an axial slice and one-dimensional profiles. However, in contrast with the numerical models, no ground truth was available for comparison. The closest data to the true phase, in this case, was the phase measured in regions where there were no phase wraps. These regions were used as a point of reference to identify alterations in the unwrapped phase due to the unwrapping process. A qualitative comparison between the wrapped phase and unwrapped phase between all three techniques (dLu, QG, and SEGUE) was performed for all collected datasets.

For the QSM pipeline of this project, the phase offset correction was performed before unwrapping, rather than during the weighted least-squares fit during echo combination to generate the total field shift (TFS) map. For the measured experimental data, the effect of phase offset correction before unwrapping and after unwrapping was studied to establish the optimal approach to process the phase information. The phase offset correction before unwrapping corresponded to the calculation of the phase offset through a phase difference map and then the elimination of the offset in the data through complex division as outlined in section 3.2.2 (equations 3.10 and 3.11).

On the other hand, phase offset correction after unwrapping assumed that the phase changes linearly with time. Then, the phase offset was removed during the weighted least square fit by using the intercept of the linear fit as the correction. This aspect was not studied in numerical simulations since they were designed with zero phase offset.

To determine the optimal phase offset correction approach, the wrapped and unwrapped phase data were compared using one-dimensional profiles and violin plots for the correction performed before and after unwrapping. Moreover, the artifacts caused by the phase offset correction were analyzed in the total field shift (TFS) and local field shift (LFS) maps. However, the results for the study of the TFS and LFS maps are presented in the section corresponding to the study of background removal in the collected data because background removal is required to produce LFS maps.

#### 4.3.3 Unwrapping and background removal techniques in conventional QSM

The different combinations of unwrapping and background removal techniques were tested for *in vivo* datasets by comparing the LFS maps obtained for each combination with the best combination determined according to numerical simulations. The unwrapping algorithms considered were dLu, QG, and SEGUE. The background removal techniques used were PDF, RESHARP, and LBV. The comparison was done using difference maps and the RMSE metric to quantify the difference between the selected reference technique (according to the best performing combination in numerical simulation) and the results obtained for every other combination. The presence of incorrectly identified local fields and errors close to the edge of the brain were also identified qualitatively by visually analyzing the LFS maps and difference maps. Qualitatively, in numerical simulation, it was observed that erroneously identified local fields (meaning background fields that were incorrectly considered as local fields) can be identified as abnormally bright or dark regions in the LFS maps.

As explained in section 4.3.2, the presence of artifacts in the TFS and LFS maps due to the phase offset correction performed before and after phase unwrapping was studied by comparing (through difference maps) the TFS and LFS maps calculated for each case. The background removal

algorithm used to generate the LFS map (and to compare the two scenarios) was the technique deemed the best option according to the results in numerical simulations and *in vivo* datasets.

#### 4.3.4 Evaluation of susceptibility maps using in vivo datasets

Analogous to what was done in numerical simulations, the quality of the susceptibility maps depending on unwrapping technique and dipole inversion/direct inversion method was assessed by comparing the appearance of the susceptibility maps created for each case. All susceptibility maps were calculated using the reconstruction parameters listed in subsection 4.2.4.1.

In vivo datasets were used to illustrate the effect of the preconditioner in LN-QSM and the improved quality of the susceptibility maps in pLN-QSM. Five different susceptibility maps were created for LN-QSM ( $P_B = 0$ ) and pLN-QSM ( $P_B = 30$ ) for different numbers of iterations of the non-linear conjugate gradient solver. The iterations considered for each case were 100, 200, 300, 400, and 500. Representative axial slices for the estimated susceptibility maps were presented for each result.

When processing the datasets, the performance of pTFI and pLN-QSM changed depending on the dataset, even when the same regularization parameters were used. To illustrate the variations in the susceptibility maps for these two techniques between datasets, the results were calculated (using MEDI+0, iSWIM, pTFI, pLN-QSM, and TFIR) for datasets D1, D2, D3, and B2 and compared considering representative axial slices for each dataset. Datasets D1, D2, and D3 were selected since these datasets correspond to the same volunteer scanned three times in a single day with slightly different sequence parameters. On the other hand, dataset B2 was selected among all datasets as it presented the most noticeable changes in the appearance of the susceptibility maps calculated with pTFI or pLN-QSM.

Finally, as done with numerical simulation, anatomical ROIs were used to measure the mean and standard deviation of the susceptibility in deep gray matter structures and the cortical region of the brain. The measurements were performed for dataset B1 using the automatic segmented ROIs produced during the creation of the numerical models. Unbalanced two-way analysis of variance

(ANOVA) with repeated measurements was performed to determine if susceptibility values from different methods were statistically different (significance level p < 0.05). The test was set up with two factors: methods and ROIs. Within the factor "methods", five levels corresponding to MEDI+0, iSWIM, pTFI, pLN-QSM, and TFIR were considered. Within the factor "ROIs", five levels corresponding to the cortex, thalamus, caudate nucleus, putamen, and globus pallidus were considered. The ANOVA test also included a heteroskedasticity-consistent (HC) correction [96]. After finding significant differences with the ANOVA test, post-hoc multiple pairwise comparisons with Bonferroni adjustments to the p-values was performed. The ANOVA test and post-hoc testing were performed in RStudio.

# Chapter 5

# **Results**

### 5.1 Evaluation of susceptibility maps using numerical simulations

#### 5.1.1 Comparison of phase unwrapping algorithms

In the numerical simulation (model B), QG and SEGUE phase unwrapping results (after correction using THUMPR) were equivalent and coincided with the ground truth of the unwrapped phase, while dLu modified the phase when compared with the ground truth. Figure 5.1 shows a visual comparison between the wrapped and unwrapped phases in numerical model B. The top row of the figure contains an axial slice showing the phase wraps (in all five echoes) produced due to the steep change in susceptibility caused by the presence of the air pocket simulating the frontal sinus. In the bottom row, the profiles of the phase values (taken across the red line in the selected axial slice) are shown. This trend was observed consistently across most of the volume-of-interest (brain) when comparing the unwrapped phase for all techniques and the ground truth.

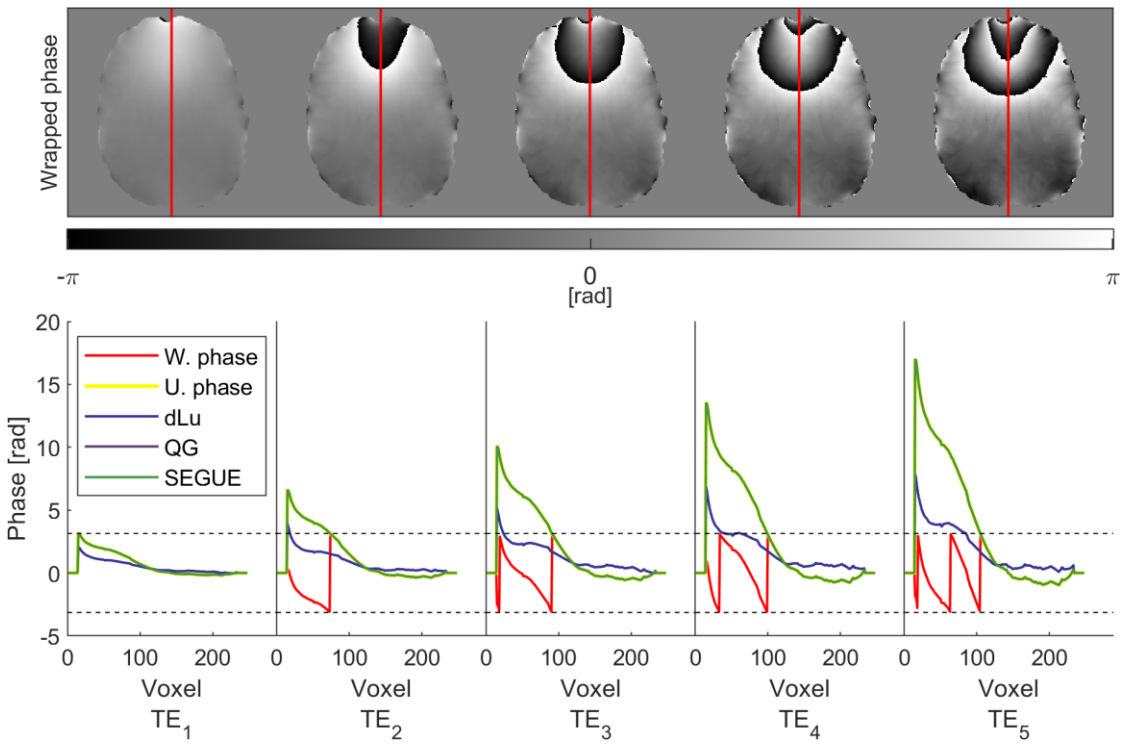


Figure 5.1: Unwrapped phase in a one-dimensional profile across an axial slice of the numerical model B. The three unwrapping techniques were dLu: discrete Laplacian, QG: quality guided, and SEGUE. The curve corresponding to QG is not observable in the diagram since the results from SEGUE and QG coincide.

In general, the biggest differences when comparing the performance of all unwrapping techniques in the numerical simulation were observed in regions close to the sinuses and the ear canal, as expected due to the steep change in susceptibility. Additionally, differences between the performance of SEGUE and QG (which appear equivalent in Figure 5.1) were observed in some voxels at the edges of the brain. These differences were caused by phase wraps at the edge of the brain. The source of these wraps was the susceptibility change in the regions representing CSF and bone near the edge of the brain. To demonstrate the errors caused by air pockets and at the edges of the brain (which are not observable in Figure 5.1), Figure 5.2 presents maximum intensity projection (MIP) difference maps for each method using as a reference of comparison the true phase from the numerical model.

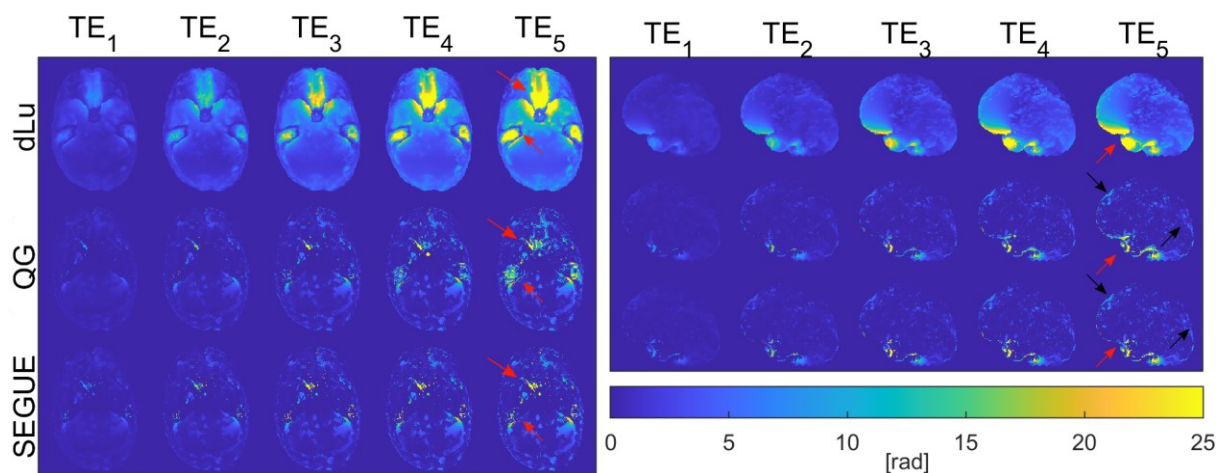


Figure 5.2: Maximum intensity projection (MIP) difference maps comparing the ground truth for the unwrapped phase in numerical model B with the results calculated with different unwrapping techniques (dLu: discrete Laplacian, QG: quality guided, and SEGUE). Superior/inferior and lateral views are presented for each case. The range to display the images was selected as 25 radians, which is the same range selected in Figure 5.1. The red arrows point to the highest magnitude deviations from the ground truth due to the air pockets representing sinuses and the ear canal. Black arrows point to high magnitude errors caused by wraps due to bone and CSF at the edge of the brain.

Table 5.1: RMSE values calculated in radians for each echo time and each unwrapping technique (dLu: discrete Laplacian, QG: quality guided, and SEGUE.). For each value at a determined echo time, the corresponding unwrapped phase extracted from numerical model B was used as ground truth.

	TE <sub>1</sub>	TE <sub>2</sub>	TE <sub>3</sub>	TE <sub>4</sub>	TE <sub>5</sub>
	[rad]	[rad]	[rad]	[rad]	[rad]
dLu	0.74	1.53	2.41	3.35	4.19
QG	0.11	0.20	0.31	0.47	0.68
SEGUE	0.12	0.23	0.35	0.46	0.58

To establish a quantitative comparison and to put all the errors in a global context, the RMSE values comparing the unwrapped phase and the true phase for each echo are presented in Table 5.1 for the noiseless numerical model and in Table 5.2 for varying levels of SNR in the simulated complex data.

In the noiseless case (Table 5.1), the RMSE increased with echo time for all unwrapping techniques, which is congruent with Figure 5.2. For TE<sub>1</sub>, TE<sub>2</sub>, and TE<sub>3</sub> QG presented the smallest RMSE. For TE<sub>4</sub> and TE<sub>5</sub> SEGUE presented the smallest RMSE. Once again, these results agree with Figure 5.2, which indicates that for the last two echoes, the errors in QG were more spread out inside the brain.

The RMSE increased with decreasing SNR for all three unwrapping techniques, meaning that the accuracy of the methods decreased with noise. When adding noise to the numerical model, QG was the best performing method (lowest RMSE values across all echoes) for SNR 10 and 20. For SNR 40 and 60, the trend observed in the noiseless case was repeated, in other words, QG had smaller RMSE for the three first echoes, while SEGUE performed better for the last two. This result would suggest that QG is less affected by noise when compared to SEGUE. Finally, the results in the table suggest that the precision of dLu does not decrease compared to the other methods, although the accuracy of dLu was still the lowest. This can be confirmed by looking at the RMSE values for the last echo for SNR 10 and SNR 60. In the case of QG and dLu, the value doubled from SNR 60 to SNR 10, while in dLu, it just increased by approximately 2%.

Table 5.2: RMSE values (in rad) for SNR 10, 20, 40, and 60 comparing the unwrapped phase for all techniques (dLu: discrete Laplacian, QG: quality guided, and SEGUE.) with the ground truth in model B.

SNR:			10			20				
	TE <sub>1</sub>	TE <sub>2</sub>	TE <sub>3</sub>	TE <sub>4</sub>	TE <sub>5</sub>	TE <sub>1</sub>	TE <sub>2</sub>	TE <sub>3</sub>	TE <sub>4</sub>	TE <sub>5</sub>
dLu	0.72	1.57	2.46	3.38	4.29	0.72	1.55	2.44	3.37	4.24
QG	0.25	0.47	0.72	1.00	1.30	0.14	0.26	0.40	0.58	0.83
SEGUE	0.28	0.55	0.83	1.11	1.45	0.19	0.36	0.55	0.73	0.92
SNR:			40			60				
	TE <sub>1</sub>	TE <sub>2</sub>	TE <sub>3</sub>	TE <sub>4</sub>	TE <sub>5</sub>	TE <sub>1</sub>	TE <sub>2</sub>	TE <sub>3</sub>	TE <sub>4</sub>	TE <sub>5</sub>
dLu	0.73	1.54	2.42	3.36	4.22	0.73	1.53	2.42	3.36	4.21
QG	0.12	0.23	0.36	0.54	0.76	0.12	0.22	0.34	0.52	0.75
SEGUE	0.14	0.27	0.40	0.54	0.68	0.13	0.24	0.37	0.49	0.62

#### 5.1.2 Unwrapping and background removal techniques in conventional QSM

PDF was the background removal algorithm that produced the local field shift (LFS) maps with the least amount of erroneously identified local fields. Moreover, PDF did not require edge erosion. It was possible to compare the performance of PDF, RESHARP, and LBV through a visual inspection of the results for each technique. In Figure 5.3, PDF produced the most visually appealing results when paired with QG or SEGUE. That said, PDF presented errors at the edge of the brain, marked by orange arrows in Figure 5.3. Contrarily, this figure illustrates that RESHARP and LBV have the biggest amount of background fields (in the displayed slice) incorrectly identified as local fields (inaccurate background removal). These errors can be observed close to the anterior region of the brain, especially when these methods were paired with dLu (as indicated by the green arrows in Figure 5.3). Moreover, the difference maps also make apparent how RESHARP requires erosion of the LFS map since it is easier to compare the size of the result and the true local field map in the selected slice. LBV also presented errors at the edges of the brain but their appearance was different when compared to PDF, and they are marked in Figure 5.3 with red arrows. The errors at the edge of the brain in PDF were constrained to the very edge of the brain. These artifacts produced a characteristic "texture" at the edge of the LFS maps absent in RESHARP or LBV. In LBV the errors at the edge looked like spurious fields that propagate towards the interior of the brain.

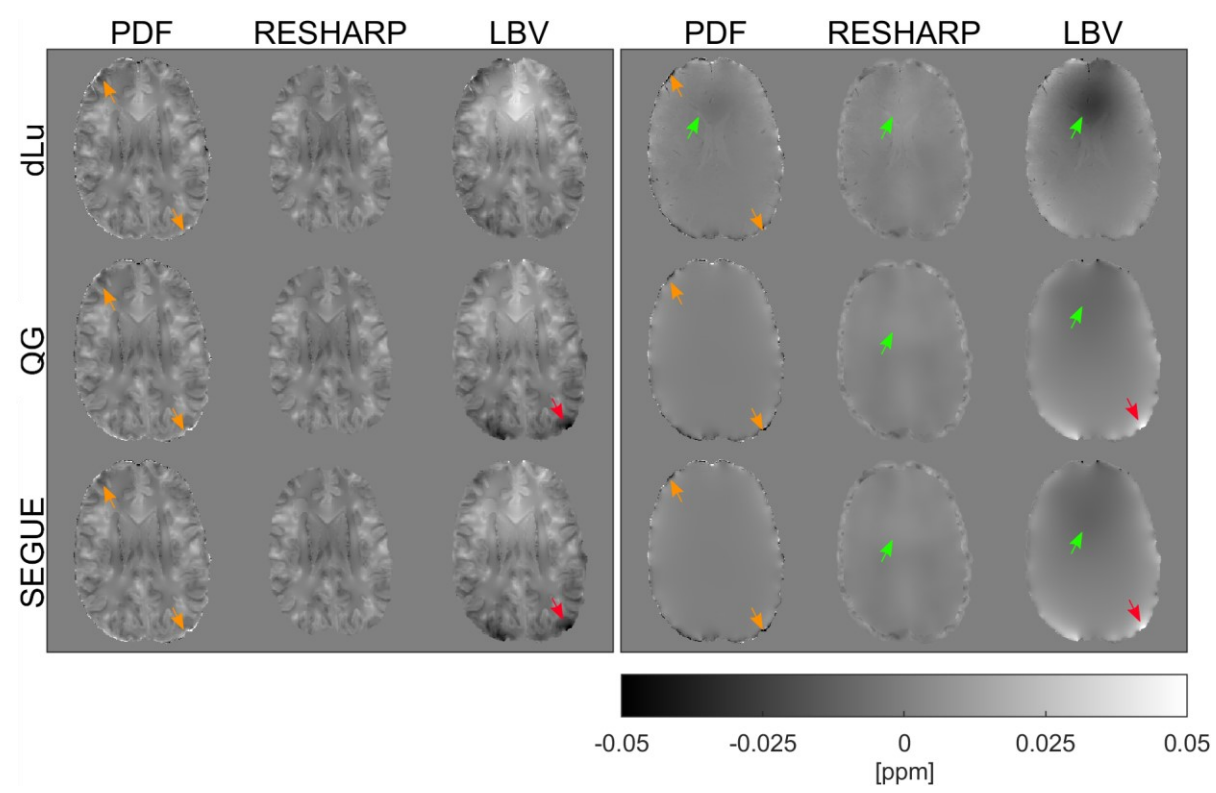


Figure 5.3: Comparison of background removal algorithms and the effect of unwrapping techniques on numerical model B. The left image shows LFS maps. The right image shows difference maps for each LFS map using as ground truth the local magnetic field derived from the numerical model. The background removal techniques were PDF, RESHARP (6 voxels radius), and LBV. The green arrows indicate examples of incorrectly identified local fields in the anterior region of the brain. The orange and red arrows indicate errors at the edges of the brain in PDF and LBV, respectively.

Using the RMSE as a metric to assess the performance of the background removal techniques, PDF was the most accurate algorithm. The RMSE values are presented in Table 5.3. When comparing the performance of PDF and LBV depending on unwrapping technique, QG+PDF or LBV performed better in the eroded mask, while dLu+PDF or LBV performed better at the edge of the brain. dLu+PDF or LBV also performed better overall in the entire brain (due to the relatively small error at the edge). PDF performed better than LBV and RESHARP in the entire brain and eroded mask, respectively, when paired with any of the three unwrapping techniques. PDF outperformed all methods in the eroded brain mask when paired with QG or SEGUE. PDF does not require explicit edge erosion (in contrast with RESHARP). Consequently, PDF was selected as the best background removal technique. However, the best unwrapping technique to

combine with PDF (for QSM) remains an open question, since the RMSE suggests that SEGUE and QG provided comparable performance, while dLu generated better results at the edge of the brain and in all the volume-of-interest. The question of the best unwrapping technique will be addressed in subsection 5.1.3.1.

Table 5.3: RMSE calculated for the combination of unwrapping and background removal techniques for numerical model B. Three different volumes were considered for calculating the RMSE. 1) A mask eroded by 6 voxels. 2) A mask representing the edge of the brain, this mask was created by subtracting the mask for the entire brain and the eroded mask. 3) The mask covering the entire brain. In the case of RESHARP, the RMSE values were only calculated for the eroded mask since the method cannot recover information outside the eroded mask.

Phase unwrapping	dLu			QG			SEGUE		
Mask erosion	Eroded	Brain	Entire	Eroded	Brain	Entire	Eroded	Brain	Entire
Mask erosion	mask	edge	brain	mask	edge	brain	mask	edge	brain
RMSE for PDF [ppb]	5.0	13.0	12.3	2.6	18.4	16.4	2.6	19.1	17.0
RMSE for RESHARP [ppb]	4.0	-	-	3.1	-	-	3.1	-	-
RMSE for LBV [ppb]	17.2	11.6	18.3	14.5	20.8	22.4	14.9	22.3	23.7

The degree of error in PDF at the edge of the brain was considerably higher when compared to the error at the eroded mask. According to the RMSE in Table 5.3, this result held for the three unwrapping techniques. Additionally, LBV presented the same trend. This trend in LBV and PDF was coherent with the images displayed in Figure 5.3. With PDF, the errors in the anterior part of the brain were mostly gone while the errors in the edge of the brain were less spread out across the edges when compared with LBV. dLu+LBV produced the lowest RMSE at the edge of the brain but, due to the poor performance of LBV in the eroded mask and full brain, this technique was discarded for the following subsection.

In PDF, the largest inaccuracies were constrained at the edges of the brain. MIP difference maps were created in an eroded mask (Figure 5.4) and in the full brain mask (Figure 5.5) to illustrate how the biggest errors in the LFS map were constrained at the edges. When comparing the maps for PDF in Figure 5.4 and Figure 5.5, the amount of high magnitude errors increased in the second case. The errors in PDF in Figure 5.5 could be traced back to the inaccuracies in the unwrapping technique caused by air pockets (sinuses and the ear canal) and wraps due to CSF and bone interfaces. However, compared to the result from unwrapping, the errors in PDF were much more spread across the edges of the brain. A similar observation can be done for LBV, although the errors in the eroded mask in LBV were higher than for PDF and RESHARP (which is consistent with Table 5.3).

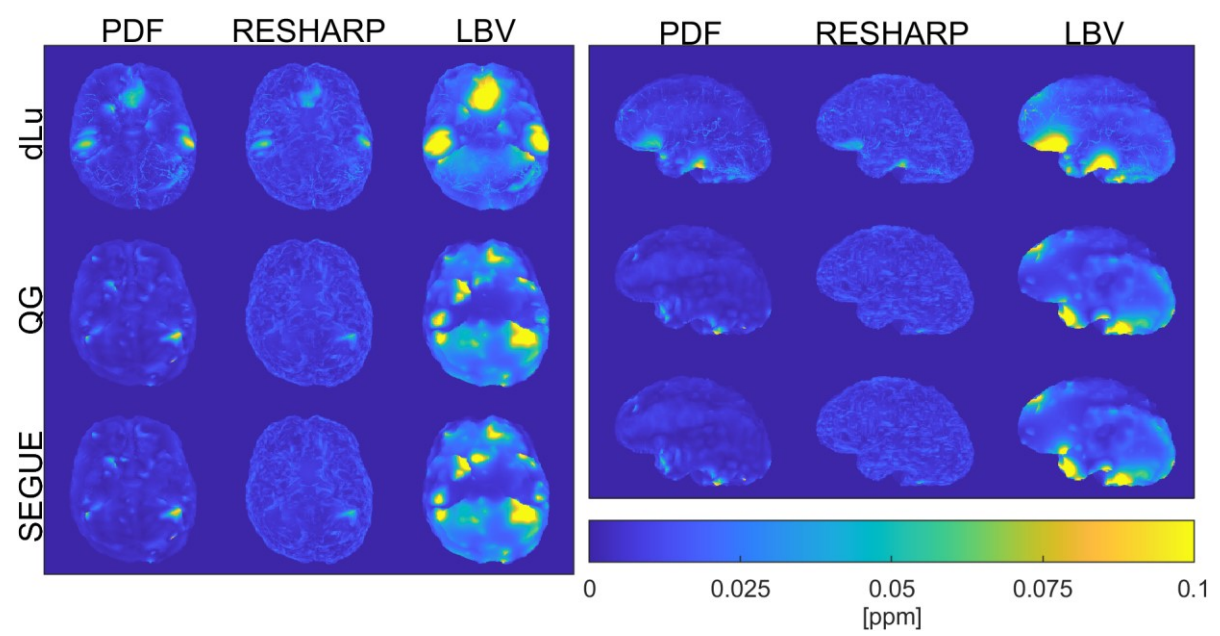


Figure 5.4: Maximum intensity projection (MIP) difference maps in an eroded mask (6 voxels) comparing the ground truth for the local field shift (LFS) in numerical model B with the results calculated with different unwrapping techniques (dLu: discrete Laplacian, QG: quality guided, and SEGUE) and background removal algorithm (PDF, RESHARP, and LBV). Superior/inferior and lateral views are presented for each case.

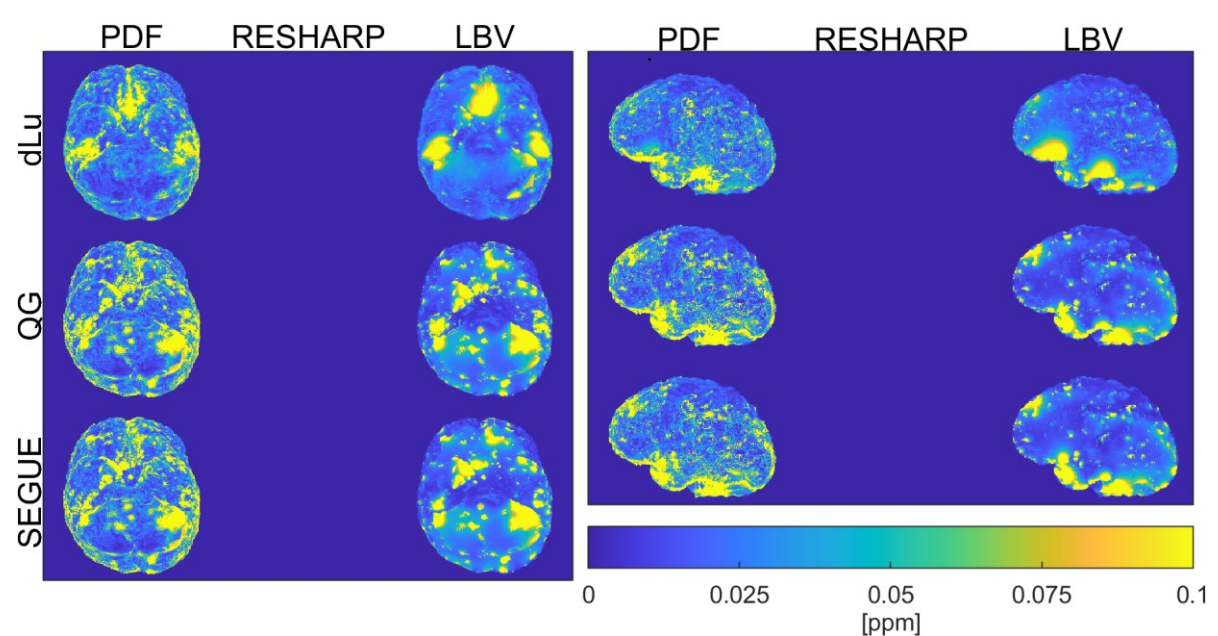


Figure 5.5: Maximum intensity projection (MIP) difference maps in a mask covering the entirety of the brain comparing the ground truth for the local field shift (LFS) in numerical model B with the results calculated with different unwrapping techniques (dLu: discrete Laplacian, QG: quality guided, and SEGUE) and background removal algorithm (PDF, RESHARP, and LBV). Superior/inferior and lateral views are presented for each case. The MIP maps for RESHARP were not calculated since this method cannot retrieve information outside the eroded mask.

#### 5.1.3 Evaluation of susceptibility maps using numerical simulations

#### 5.1.3.1 Unwrapping and background removal in QSM

According to the results from subsection 5.1.2, it was established that PDF was the best option for the background removal step. Thus, the susceptibility maps for comparison between conventional QSM and direct inversion methods were generated using PDF. However, in subsection 5.1.2, it was not possible to define the best unwrapping technique to pair with PDF. Consequently, different unwrapping techniques are used in this subsection. Moreover, consideration of different unwrapping techniques (despite findings in subsection 5.1.1) was also done to establish how unwrapping affects direct inversion methods.

Considering the RMSE values presented in Table 5.4 comparing the ground truth of the susceptibility map and the susceptibility distributions estimated using different techniques, the best unwrapping technique for QSM was QG. Almost all the techniques performed better when paired with QG. TFIR was an exception since it performed better when paired with dLu. However, the RMSE of dLu+TFIR was around 1.5 to 2.6 times bigger than QG paired with dipole inversion algorithms, pTFI, or pLN-QSM. Therefore, QG produced the most accurate susceptibility maps.

Table 5.4: RMSE in ppb for numerical model B for different combinations of unwrapping techniques and conventional and direct inversion QSM techniques. All conventional QSM susceptibility maps were created using PDF as the background removal algorithm.

	MEDI+0	iSWIM	pTFI	pLN-QSM	TFIR
	[ppb]	[ppb]	[ppb]	[ppb]	[ppb]
dLu	60.2	42.7	32.7	35.1	49.9
QG	32.3	33.3	19.0	19.6	72.4
SEGUE	101.0	91.4	64.4	69.5	88.6

Using the RMSE as a metric of accuracy, the three most accurate methods were pTFI, pLN-QSM, and MEDI+0 paired with QG (and PDF in the case of conventional QSM). The most accurate method was pTFI. This result suggests that direct inversion methods are more accurate than conventional QSM.

When qualitatively comparing the visual appearance of the susceptibility maps depending on the unwrapping technique, the techniques paired with QG presented fewer artifacts. Figure 5.6 shows axial and sagittal views for numerical model B and different combinations of QSM and unwrapping techniques. In the numerical model, when using SEGUE or dLu, there were several "bright and dark" artifacts (red arrows), ringing artifacts (blue arrows), and streaking artifacts (green arrows) close to the anterior part of the brain. Most of those artifacts were much less prominent when using QG. Most of the artifacts remaining in direct inversion methods when paired with QG corresponded to regularization artifacts that manifest themselves as shadows or "non-uniform" intensity across the image.

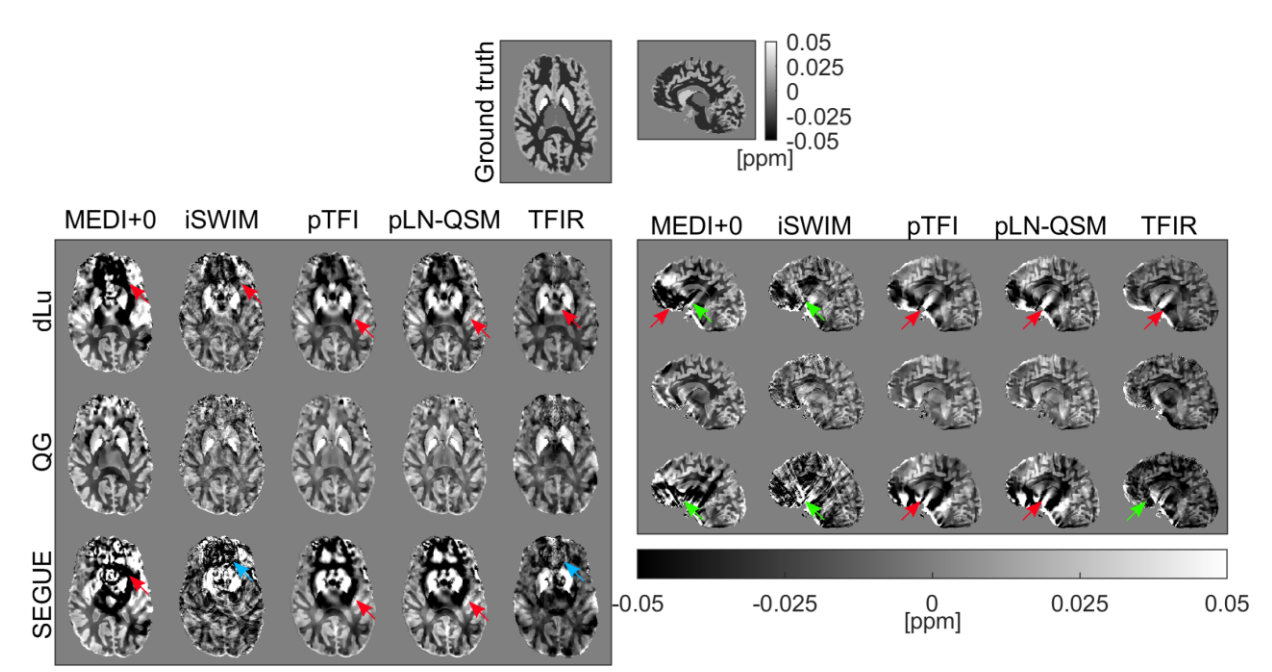


Figure 5.6: Axial and sagittal views of susceptibility maps for numerical model B for different unwrapping techniques using conventional QSM and direct field inversion techniques. For all conventional QSM results, the background removal was performed with PDF. The susceptibility mapping algorithms considered were MEDI+0, iSWIM, pTFI, pLN-QSM, and TFIR. The rows represent the unwrapping method, while the columns are the dipole inversion or direct inversion technique. The arrows point to "bright and dark" artifacts (red arrows), ringing artifacts (blue arrows), and streaking artifacts (green arrows).

MIP difference maps (Figure 5.7) depict pTFI and pLN-QSM paired with QG as the methods with the smallest errors when comparing the estimated susceptibility distributions and the ground truth for numerical model B, which is coherent with the RMSE metric and the visual assessment of the susceptibility maps. The location of the errors in pTFI and pLN-QSM (black arrows) coincided with errors that can be traced back to deviations from the true phase during unwrapping, meaning errors due to air pockets simulating sinuses and ear canals. Additional high magnitude errors (red arrows) presented in the space corresponding to deep gray matter structures (thalamus, caudate nucleus, putamen, and globus pallidus). In conventional QSM, the maps showed high magnitude errors that were much more spread throughout the volume-of-interest (compared to direct inversion methods).

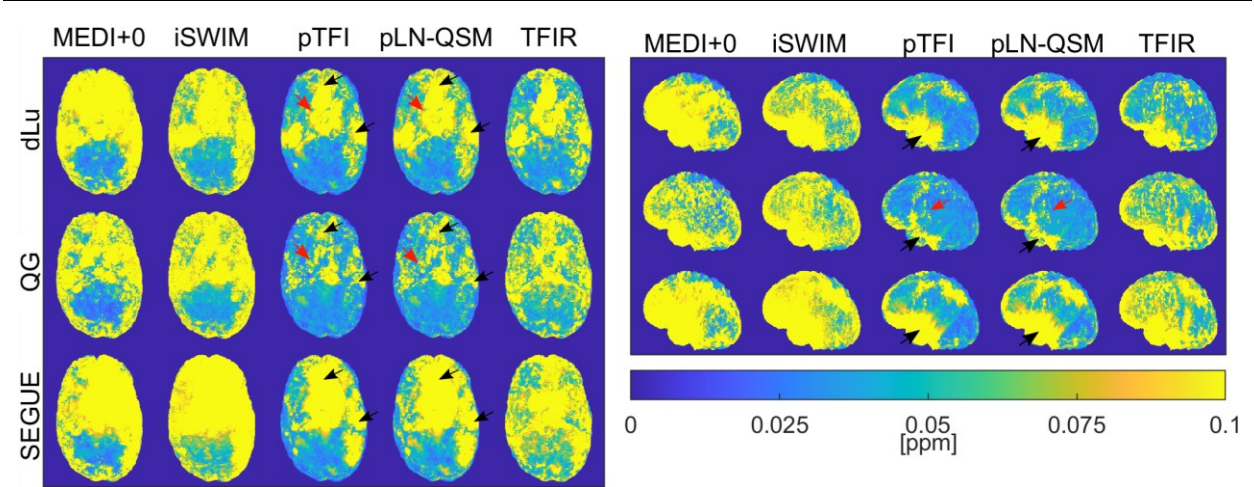


Figure 5.7: Maximum intensity projection (MIP) difference maps comparing the ground truth in numerical model B and the susceptibility maps for different unwrapping techniques using conventional QSM and direct field inversion techniques. Superior/inferior and lateral views are presented for each case. The display range was selected as the same in Figure 5.6. The black arrows point to regions of high magnitude errors due to air pockets (sinuses and ear canal). Red arrows point to errors in deep gray matter structures.

In subsequent subsections, QG was used in all results for the numerical simulations.

#### 5.1.3.2 Comparison of conventional QSM and direct field inversion methods

In pTFI and pLN-QSM, the combination of background removal and dipole inversion in a single step reduced the number of errors in the final susceptibility map. This result is observable in Figure 5.7 by comparing the susceptibility maps for QG. In this figure, the maps from pTFI and pLN-QSM presented fewer errors than MEDI+0 and iSWIM. To show that the elimination of an explicit background removal step was the element that lead to fewer errors in QSM, Figure 5.8 showed a comparison of the LFS maps produce by QG+PDF and by forward modeling the susceptibility distribution in pTFI, pLN-QSM, and TFIR. In pTFI and pLN-QSM, the errors were considerably less spread across the edge of the brain in comparison to PDF. TFIR, which according to the RMSE in Table 5.4 produced the worst susceptibility maps among all direct inversion methods, also generated a susceptibility map that corresponded to an LFS map with fewer errors than the conventional pipeline.

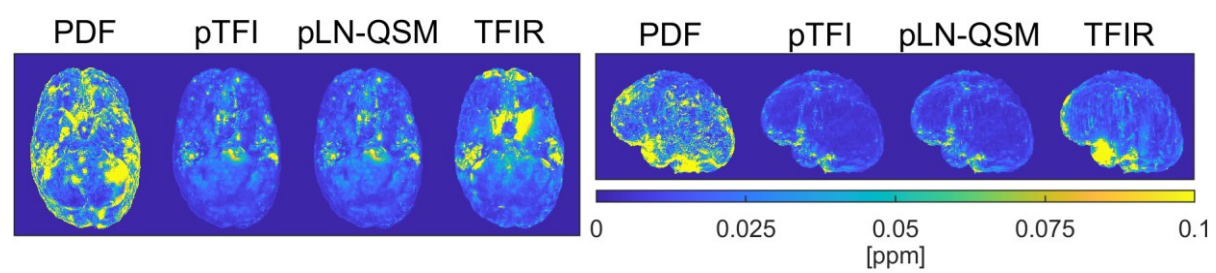


Figure 5.8: Maximum intensity projection (MIP) difference maps comparing the ground truth of the local field shift (LFS) maps obtained using PDF and forward modeling the susceptibility distribution estimated by direct inversion methods. Superior/inferior and lateral views are presented for each case.

pTFI and pLN-QSM retained less structural information when compared to MEDI+0, but these two direct inversion methods also produced fewer artifacts close to the edges (in comparison to conventional QSM). In Figure 5.9 a) and b), the distribution of errors depicted in the difference maps show how pTFI and pLN-QSM struggled to reproduce susceptibility changes, which is more apparent in the axial view of the susceptibility maps. The profiles (for the susceptibility values) in Figure 5.9 c) support this statement by showing that pTFI and pLN-QSM produced smooth susceptibility profiles (due to the added regularization in these methods) that cannot accurately reproduce the discontinuities in the initial numerical model. On the other hand, when compared to the other techniques, MEDI+0 retained more structural information causing "flat" looking difference maps.

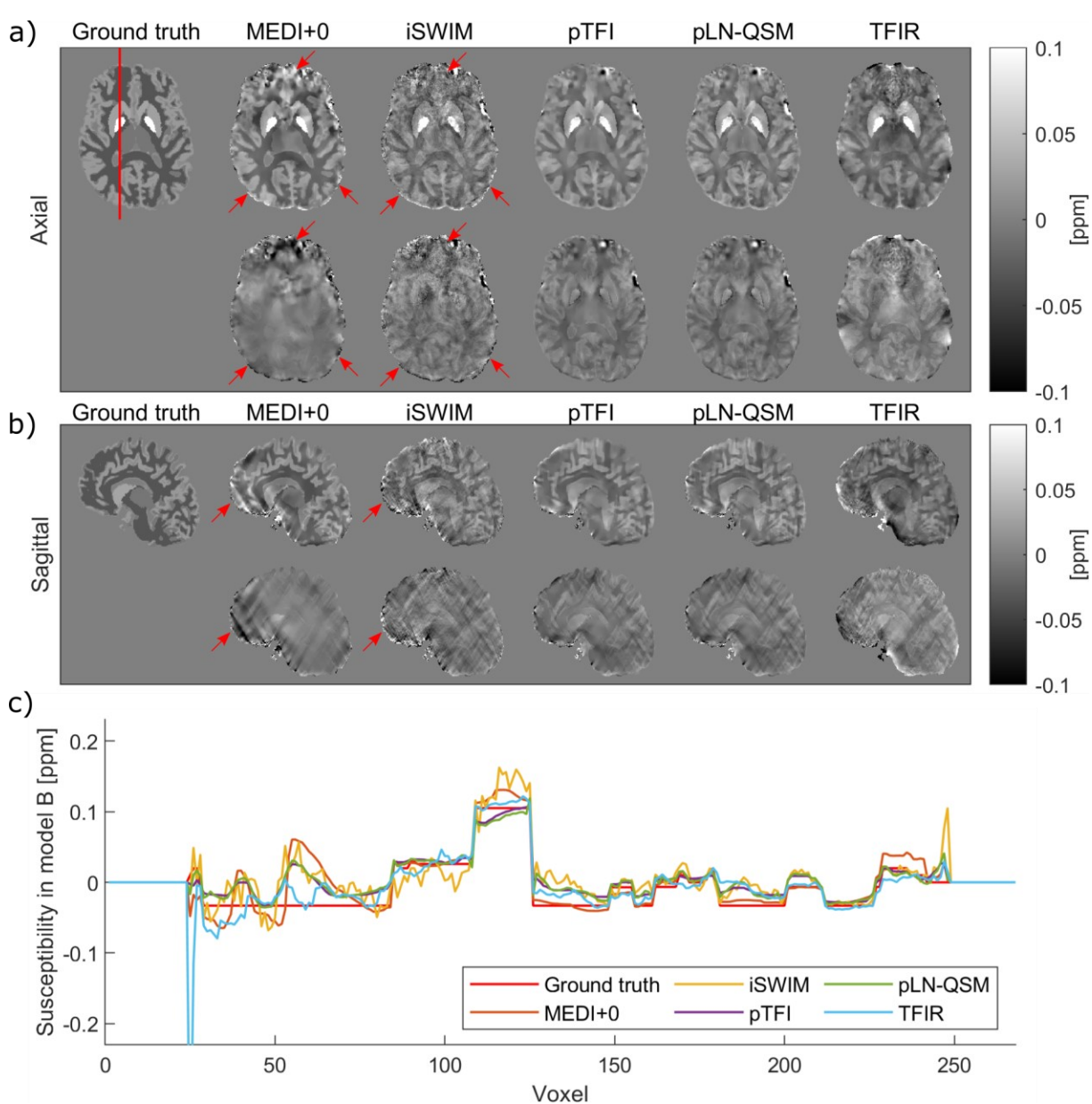


Figure 5.9: Comparison of conventional QSM and direct inversion methods in axial and sagittal slices, and one-dimensional profiles. a) Susceptibility maps (superior row) and difference maps (inferior row) for an axial slice in numerical model B. b) Susceptibility maps (superior row) and difference maps (inferior row) for a sagittal slice in numerical model B. c) One-dimensional profile representing the susceptibility across the red line illustrated in a). The red arrows indicate artifacts in conventional QSM that are not present in direct inversion methods.

pTFI and pLN-QSM showed fewer artifacts close to the anterior regions of the brain in axial and sagittal views. Moreover, these techniques did not present the abnormal "textured" edge that appears in conventional QSM due to PDF, which makes these methods overall more accurate.

These artifacts are indicated in Figure 5.9 a) and b) by red arrows. Finally, iSWIM and TFIR produced the susceptibility with the most amount of artifacts for conventional QSM and direct inversion methods. iSWIM produced susceptibility maps with a "salt and pepper" texture that translates into an irregular profile in Figure 5.9 c). TFIR presented ringing artifacts due to the inclusion of spherical mean value (SMV) filtration.

#### 5.1.3.3 Decoding the operation of direct inversion methods

Direct inversion methods work by creating a susceptibility distribution outside the brain to model the background field. The background field corresponds to dipolar fields produced by sources outside the volume-of-interest. By studying the susceptibility distributions produced by direct inversion methods inside and outside the volume-of-interest (in this case, defined by the brain binary mask), it was verified that the estimated susceptibility distribution outside the brain was different from zero. Figure 5.10 presents a comparison between the ground truths and estimated maps for the background field, local field shift (LFS), and susceptibility distribution. A good agreement was observed between the estimated background field (produced by the susceptibility outside the brain) and the true background field included in the model, according to the RMSE metric. The same was observed when comparing the estimated LFS with the true local field included in the model. The RMSE when comparing the background field and LFS maps were 0.0899 ppm and 0.0050 ppm, respectively. The values make sense when considering the order of magnitude in each case. Background field are expected to be around unity of ppm, while in the case of local fields the order of magnitude is tenths of ppm. In both cases, the RMSE was two orders of magnitude smaller than the corresponding range of values. This small error signals agreement between the forward models from the ground truth and the estimated solution. It confirms that the susceptibility distribution established outside the brain is how pLN-QSM determines the background field. Figure 5.10 was created from the results obtained for numerical simulation in model B and pLN-QSM. Similar agreement and consequently the same mechanism to model the background field was observed for pTFI and TFIR (images not presented).

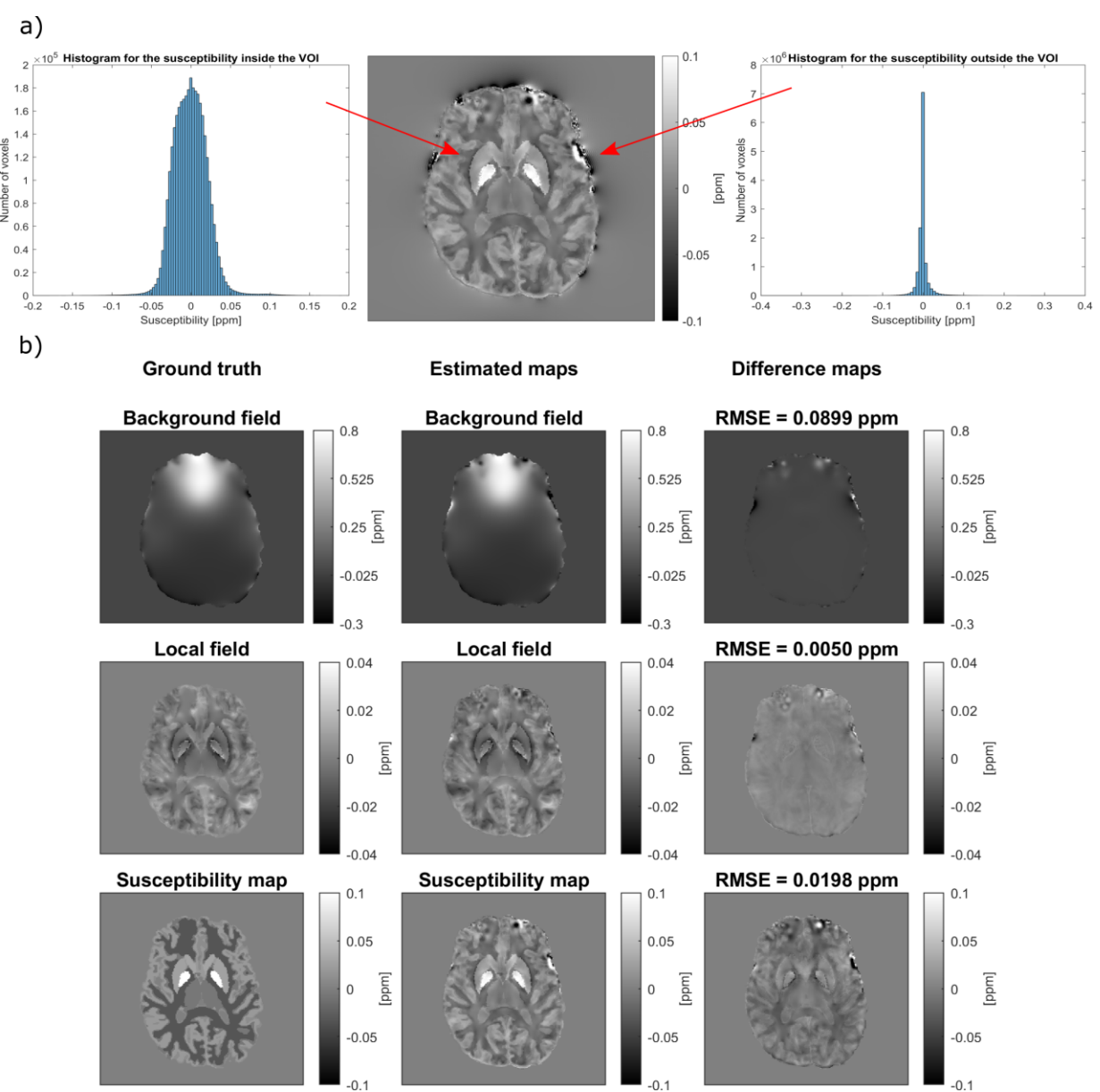


Figure 5.10: Representation of the operation of direct inversion methods. pLN-QSM was selected to illustrate how these methods work. a) The figure shows an axial slice of the estimated susceptibility for model B. The histograms show the susceptibility distribution inside and outside the brain (in the entire brain). b) The susceptibility distributions inside and outside the brain were forward modeled to generate the corresponding background field and local field (LFS), which were compared with the ground truth from numerical model B. The estimated and true susceptibility maps are also compared. The RMSE was used as a metric for comparison.

#### 5.1.3.4 Measurement of the susceptibility in anatomical ROIs

One small detail in Figure 5.10 that should catch the attention of the attentive reader is that the estimated susceptibility distribution inside the brain is gaussian, even though the input model (model B) was composed of a discrete set of susceptibility values. To estimate the susceptibility, iSWIM, pTFI, pLN-QSM, and TFIR produced gaussian susceptibility distributions. These behaviors are presented in Figure 5.11. The initial numerical model is a set of discrete susceptibility values, but the LFS calculated from these values (as showed in the figure) is normally distributed. Thus, the QSM inverse problem, in the context of these numerical simulations, can be considered as seeking a discrete solution (susceptibility distribution) from the normally distributed LFS. MEDI+0 was the only method that produced a multimodal distribution. When comparing this distribution to the ground truth in Figure 5.11 b), it is possible to see how the peaks in MEDI+0 are reminiscent of the position of the peaks at -0.033, -0.006, and 0.02 ppm in the ground truth. However, the multimodal distribution does not exactly coincide with the distribution of the numerical model. All other methods generate gaussian susceptibility distributions (Figure 5.11 b) and c)). Finally, it is important to highlight that all the histograms are normalized to the number of voxels, consequently, the height of the bars in the histogram also has valuable information. In all cases, the height of the bars in the ground truth is around one order of magnitude greater than in the estimated susceptibility distributions.

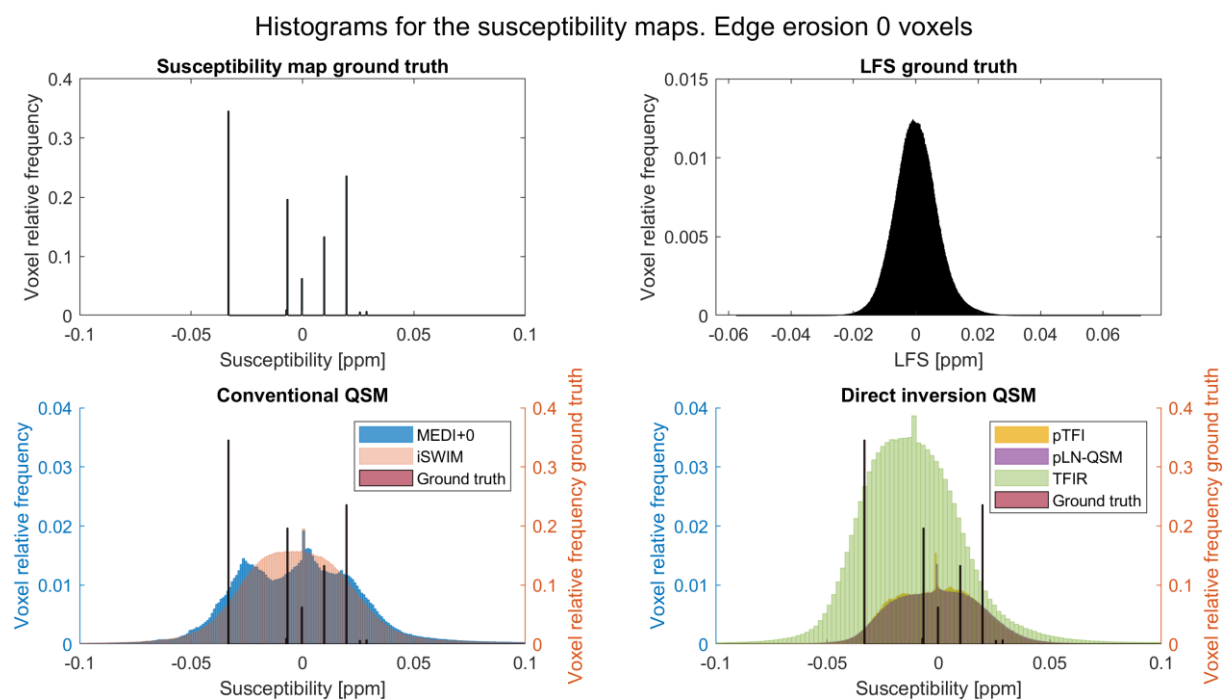


Figure 5.11: Histograms comparing the susceptibility distribution estimated by conventional QSM and direct inversion methods with the ground truth in numerical model B. a) Ground truth susceptibility distribution for numerical model B. b) Histogram of the LFS forward-modeled from the susceptibility by c). Histogram of estimated susceptibility distribution for conventional QSM on the left axis and ground truth susceptibility distribution on the right axis. d) Histogram of estimated susceptibility distribution for direct inversion QSM on the left axis and ground truth susceptibility distribution on the right.

pTFI and pLN-QSM more accurately described the susceptibility in the cortical region of the brain, as supported by the RMSE presented in Table 5.5. However, pTFI and pLN-QSM tended to underestimate the susceptibility in the considered ROIs when compared to the ground truth or conventional QSM. The mean and standard deviation of the measurements in anatomical ROIs are presented in Figure 5.12. pTFI and pLN-QSM returned lower mean values compared to MEDI+0 and ground truth. This is especially noticeable in deep gray matter structures, such as the globus pallidus (the highest susceptibility source included in the model), where pTFI and pLN-QSM estimated the lowest susceptibility values from all the QSM techniques considered. In the thalamus, Figure 5.12 also shows that pTFI and pLN-QSM failed to estimate a negative average value for the susceptibility of the structure. TFIR, when compared to the other two direct inversion methods, was more accurate in the globus pallidus. Moreover, TFIR generated a negative mean

value in the thalamus, where pTFI and pLN-QSM estimated positive mean values. But TFIR was the least accurate method in all other structures (except the globus pallidus). The 95% confidence intervals for the data Figure 5.12, not shown in the plot due to their small scale, suggested that almost all measurements were significantly different since the confidence intervals did not overlap for the measurements in the ROIs (the only exception was pTFI and pLN-QSM in the putamen). In no case did the confidence intervals contain the true value.

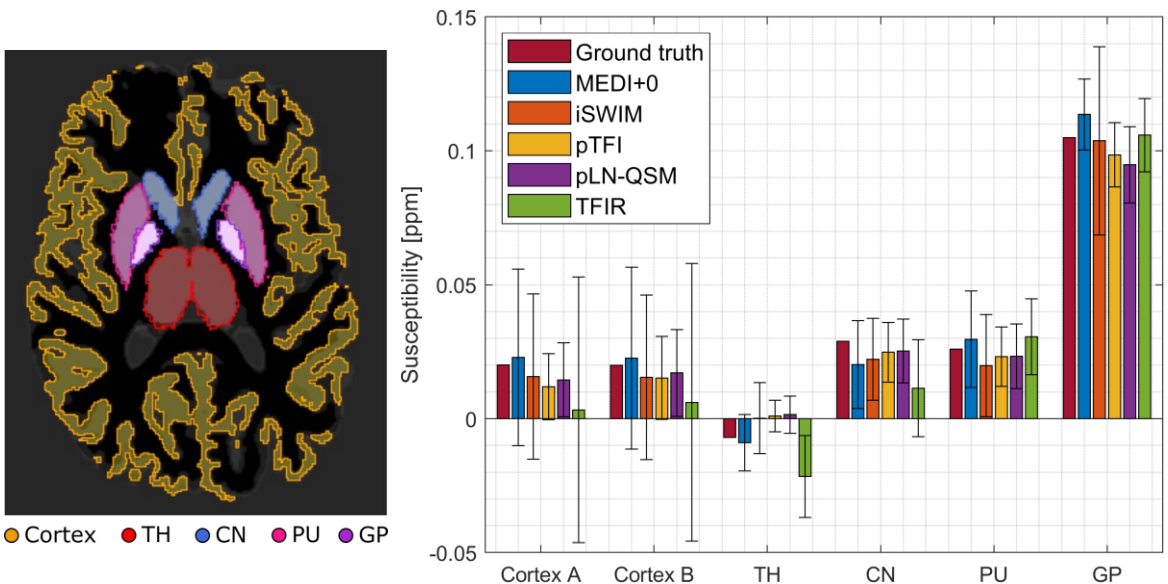


Figure 5.12: Bar plot of the mean and standard deviation in anatomical ROIs in the numerical models of the brain. The susceptibility of the cortical region of the brain was measured in model A (Cortex A) and model B (Cortex B). The susceptibility of the thalamus (TH), caudate nucleus (CN), putamen (PU), and globus pallidus (GP) are reported only for model B. The image on the left shows an axial slice of numerical model B with the position of the ROIs highlighted in different colors for each structure.

Table 5.5: RMSE (in ppb) for anatomical ROIs and the true values for the cortical region of the brain (Cortex A and Cortex B for numerical models A and B, respectively), thalamus (TH), caudate nucleus (CN), putamen (PU), and globus pallidus (GP).

	Cortex A	Cortex B	TH	CN	PU	GP
	[ppb]	[ppb]	[ppb]	[ppb]	[ppb]	[ppb]
MEDI+0	33.1	34.1	10.6	18.6	18.4	15.8
iSWIM	31.2	31.1	15.1	16.7	20.1	35.1
pTFI	14.8	16.2	9.9	11.9	11.4	13.6
pLN-QSM	14.9	16.5	11.0	12.5	12.4	17.5
TFIR	52.3	53.7	21.1	25.2	14.9	13.7

#### 5.1.3.5 Susceptibility estimation for varying SNR

When including noise in numerical model B, the appearance of the susceptibility maps changed depending on the amount of noise and dipole inversion or direct inversion technique. Axial slices for the results obtained at different SNRs in model B are showed in Figure 5.13. In the case of conventional QSM, the susceptibility maps presented speckle due to the increase in noise. This effect was much more prominent in iSWIM, in which case the "salt and pepper" appearance of the susceptibly maps was very noticeable at an SNR of 10 and still present at an SNR of 60. In MEDI+0, this effect was observed at an SNR of 10, although less noticeable when compared with iSWIM, and at an SNR of 40 the speckle was barely noticeable. With direct inversion methods pTFI and pLN-QSM, some speckle was observed in the susceptibility map especially at SNRs of 10 and 20. The speckle was more noticeable in the pLN-QSM output when compared with pTFI. Finally, in TFIR, ringing artifacts were more noticeable at smaller SNRs. These artifacts in TFIR appeared at all noise levels. Also, a very faint salt and pepper pattern appeared in the TFIR output for the lowest SNR.

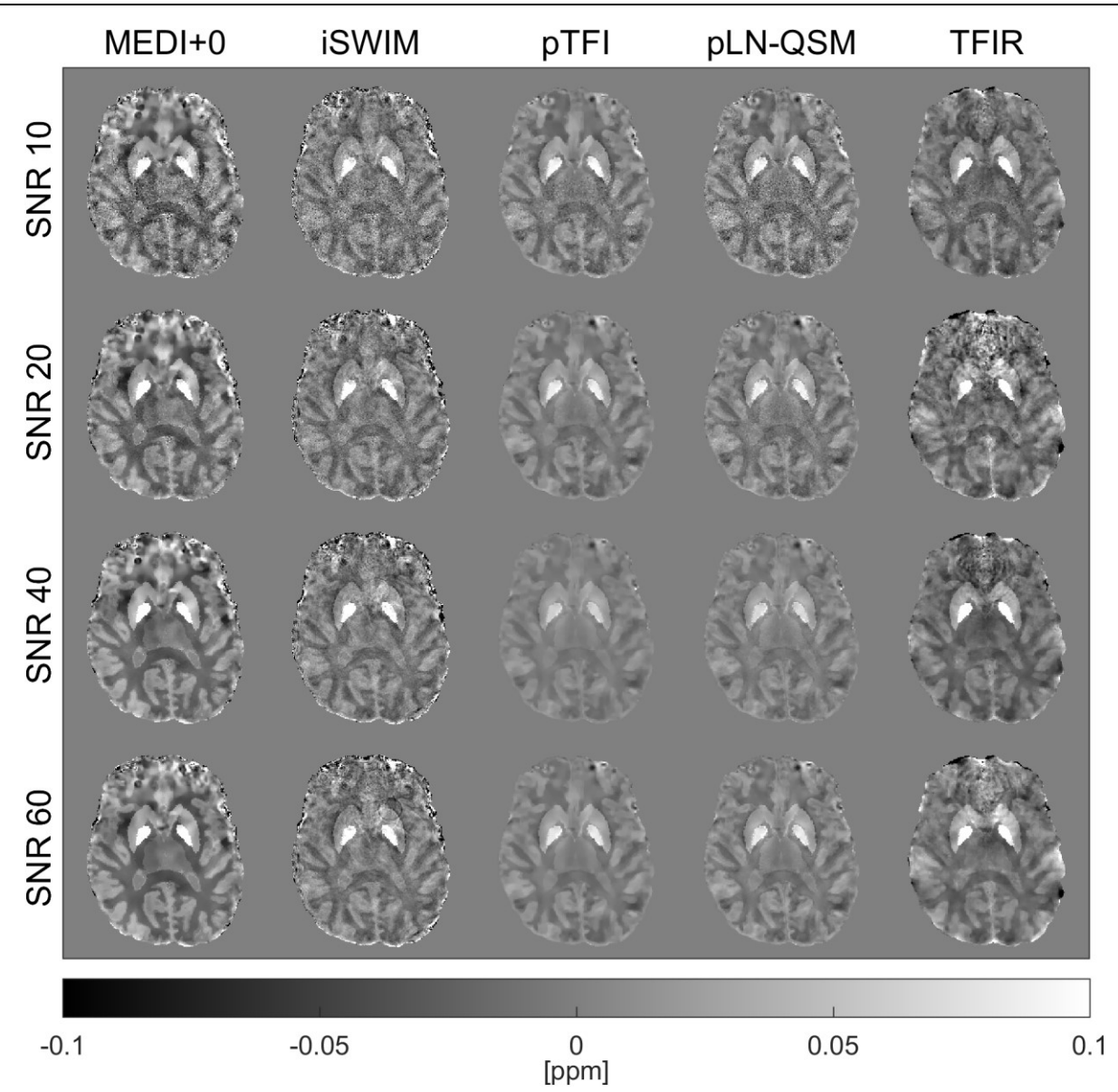


Figure 5.13: Axial slice of numerical model B for different SNR values and QSM techniques.

In MEDI+0, the precision of the susceptibility measured in ROIs corresponding to the TH, CN, PU, and GP increased with decreasing noise. A similar effect was noticed in the cortex of the numerical brain. However, the effect was much less pronounced compared to the deep gray matter structures. To illustrate this observation for varying levels of SNR in model B, box charts are presented in Figure 5.14 for the susceptibility measured in the cortical region of the brain and the GP. In these two structures, the measured susceptibility was found to be normally distributed. With iSWIM, little change in the precision of the measurement was observed, in contrast with MEDI+0.

In pTFI and pLN-QSM, in contrast with MEDI+0, the most noticeable consequence of a change in the SNR was a shift of the values measured in anatomical ROIs. This behavior can be observed in Figure 5.14. In the susceptibility maps, this is observable as subtle changes in susceptibility values. The shift of values was also accompanied by a small change in precision in the measurement. Once again, this behavior was much more noticeable in deep gray matter structures than in the cortical region of the brain. Finally, TFIR presented a behavior closer to MEDI+0, especially for deep grey matter structures.

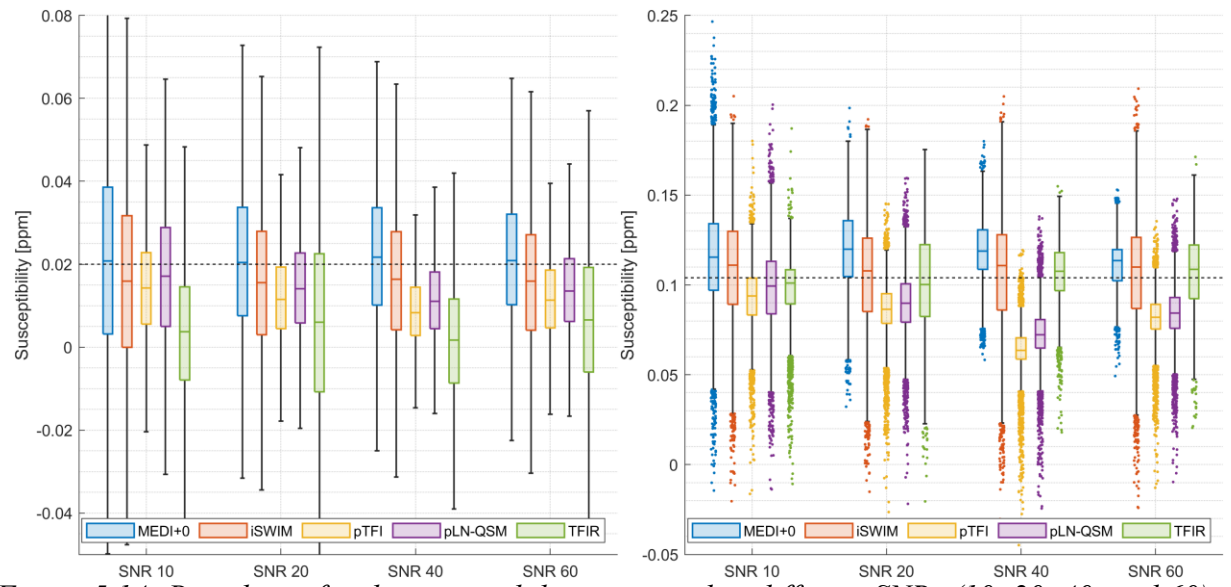


Figure 5.14: Box charts for the susceptibility measured at different SNRs (10, 20, 40, and 60) in model B for the cortical region of the brain (left) and the globus pallidus (right). The ground truth for the susceptibility values of the cortical region and globus pallidus are 0.020 and 0.104 ppm, respectively. These values are represented by black dashed lines. The diagram on the left does not show outlier values since their quantity prevents a good visualization of the boxes.

## 5.2 Evaluation of direct field inversion methods using in vivo datasets

To illustrate the results in each section related to *in vivo* datesets, a single representative dataset (unless otherwise stated) exemplifying the general behaviors observed across all datasets was used.

#### 5.2.1 Unwrapping algorithm comparison

When comparing the performance of unwrapping techniques, the unwrapped phase produced by dLu considerably differed from the phase estimated by QG and SEGUE. One example of the phase modification due to dLu unwrapping can be seen in the first echo in Figure 5.15. In the first echo, for the selected slice and profile orientation, a single wrap appears in the profile. Consequently, the wrapped phase (after phase offset correction), in this case, would be the closest data to the ground truth for the unwrapped phase. When comparing the true phase with the unwrapped phase obtained with dLu, the two phases are considerably different.

On the other hand, SEGUE and QG performed very similarly in the volume-of-interest (brain). However, the results of these two techniques differed in regions close to the sinuses and air canals and regions corresponding to vasculature. In regions corresponding to vasculature inside the brain, the algorithms handle the phase unwrapping differently due to flow artifacts. Examples of errors in the unwrapped phase for these two algorithms due to flow artifacts are present in the fifth echo in Figure 5.15. QG presents a very high maximum (orange arrow) in the location corresponding to the great vein of Galen (this maximum is not present either in the wrapped phase or in SEGUE), while SEGUE presents a minimum at approximately the same location (this minimum is not present either in the wrapped phase or in QG). Also, both QG and SEGUE failed to estimate the correct phase in the internal cerebral veins (green arrow) when compared to the true phase (since no wraps are presented in that region).

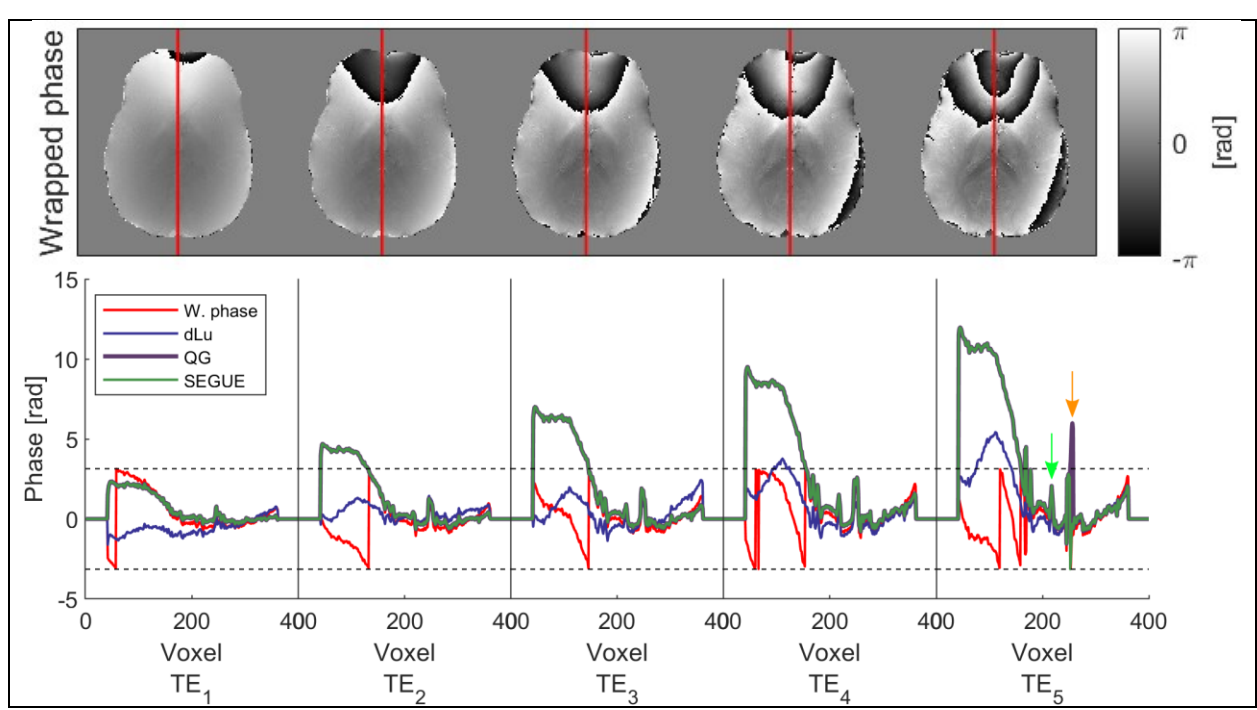


Figure 5.15: Unwrapped phase in a one-dimensional profile across an axial slice in a in vivo dataset. The three unwrapping techniques considered were dLu: discrete Laplacian, QG: quality guided, and SEGUE. The data for this figure was obtained from dataset D1 and the unwrapping was performed after phase offset correction. The green and orange arrows correspond to errors in the unwrapped phase in the internal cerebral veins and great vein of Galen.

One noticeable difference between the QG and SEGUE is that in all datasets studied, SEGUE tended to fill some regions of rapidly changing phase with zeros, while QG filled the same spaces with non-zero values. This behavior is illustrated in Figure 5.16 in axial slice where the anterior portion of the slice is close to the sinuses or close to ear canals. SEGUE places zeros in the unwrapped phase map in regions where the wrapped phase is not well-behaved, where isocontours do not form closed loops or where they terminate at the brain edge.

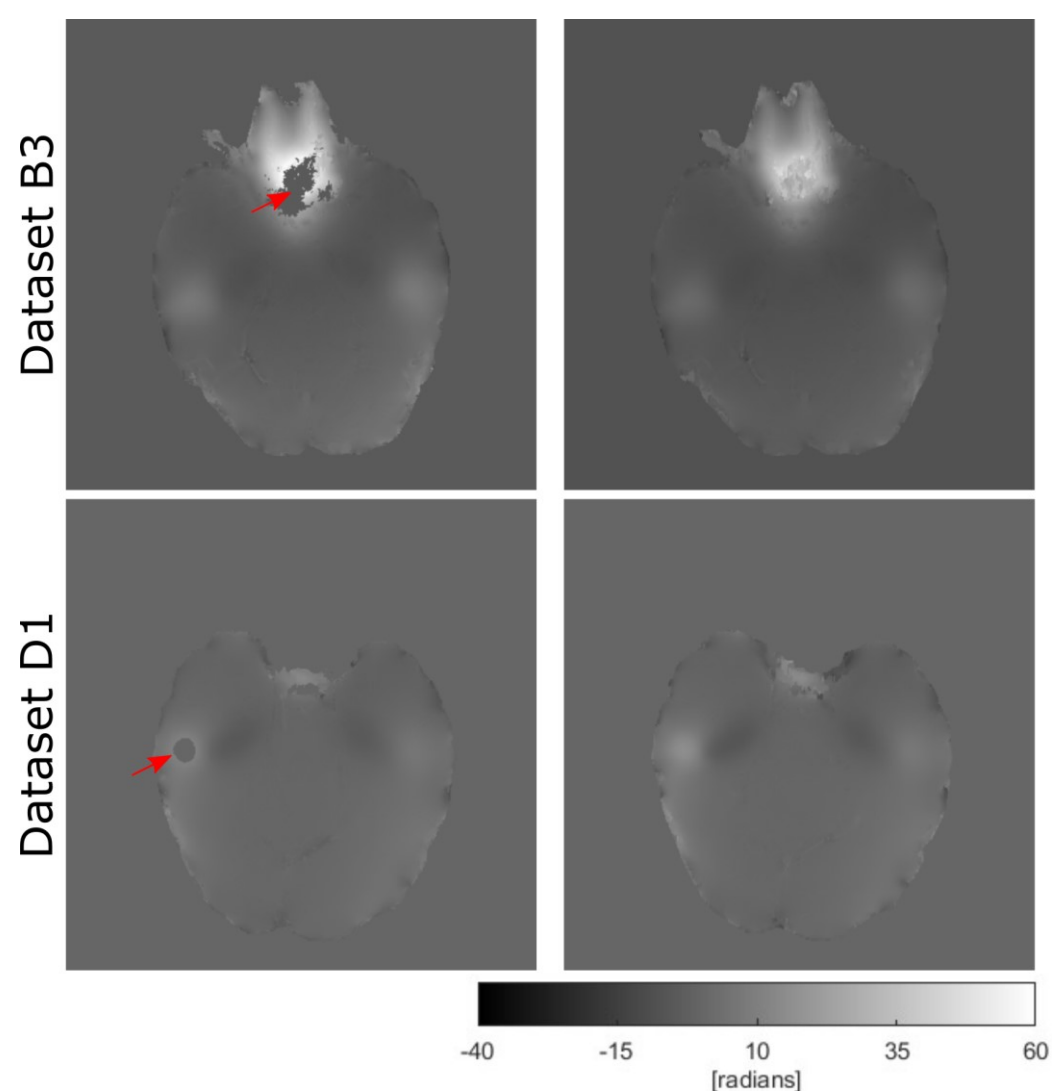


Figure 5.16: SEGUE and QG unwrapping difference in regions where the phase wraps are not well-behaved. Both images were obtained from the fifth echo in datasets B3 and D1 and represent the regions where SEGUE was observed to fail in all datasets. The images at the left corresponds to the result from SEGUE, while the image at the right is the result from QG. SEGUE tend to assign zero value to voxels inside regions of high value and rapid changing phase values close to air pockets (sinuses and ear canals).

The unwrapped phase predicted by QG and SEGUE, in some cases, differed from the wrapped phase, even where there were no phase wraps (meaning where the wrapped phase coincided with the true phase). This behavior is observable in Figure 5.15 (and it also was observed in all datasets), particularly at the beginning and at the end of the curves representing the phase across a one-

dimensional profile. As shown below, this difference was not an unwrapping error, but rather evidence of the phase offset correction performed before phase unwrapping.

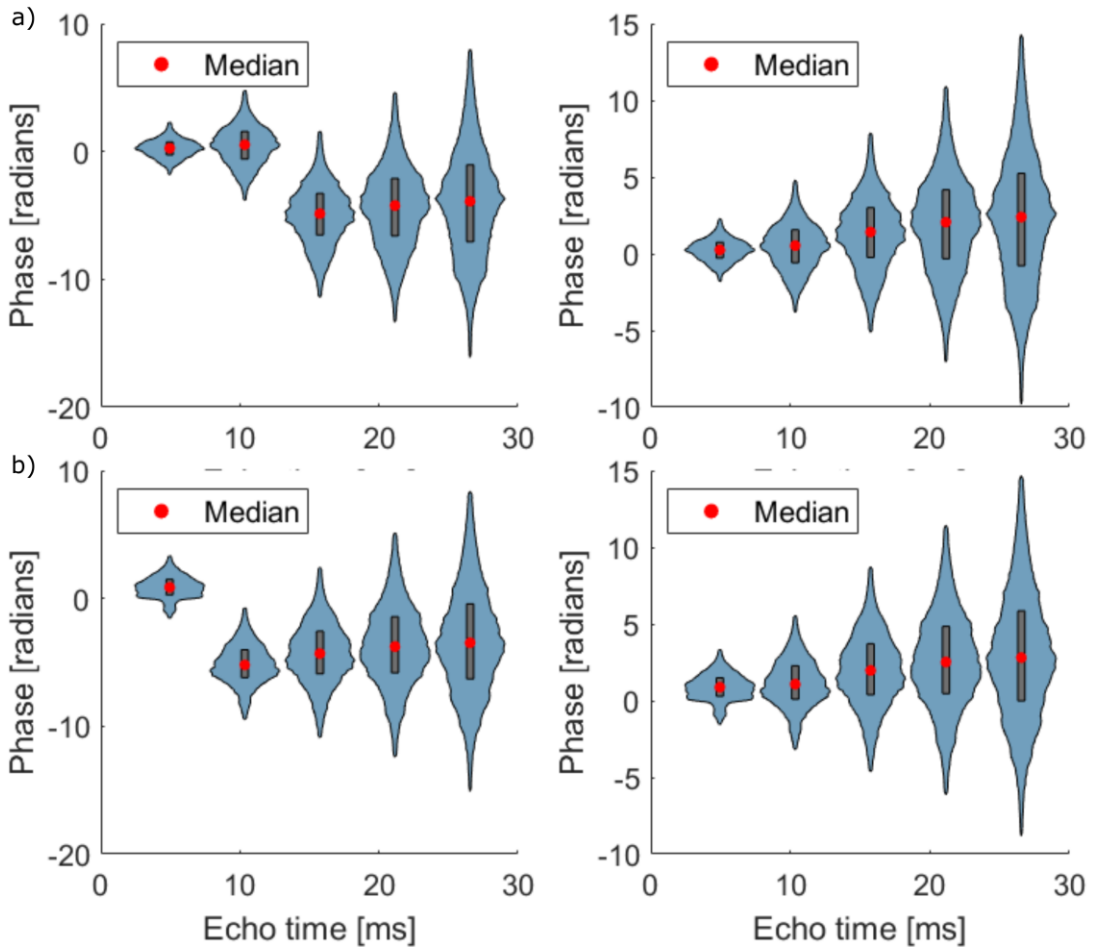


Figure 5.17: Violin plots representing the phase distribution after spatial unwrapping (using QG) at each echo before (left column) and after (right column) temporal phase unwrapping using THUMPR. The two images at each row (a and b) represent different methods to handle the phase offset correction. a) The phase offset correction was done before temporal unwrapping using a phase difference map and complex division. B) The distributions are presented without phase offset correction, which would take place during the weighted linear fit to combine the phase data. In the first case, the temporal wrap appears between the second and third echoes, while in the second case the wrap appears between the first and second echoes. The phase information used corresponds to dataset C2.

The discrepancies between the true phase and the unwrapped phase at the edges of the profiles in Figure 5.15 were due to the phase offset correction. The phase offset correction causes the wrapped

and (consequently) the unwrapped phase to change. In Figure 5.18 the wrapped phase without phase offset correction (as in Figure 5.15) is compared with the wrapped phase with phase offset correction. The figure also compares the unwrapped phase (using QG) with and without phase offset correction. As can be seen in Figure 5.18 (and in contrast with Figure 5.15), the unwrapped phase indeed coincides with the wrapped phase when considering phase offset correction. Figure 5.18 basically presents the unwrapped phase across a single one-dimensional profile for the unwrapped phase (after THUMPR) presented in Figure 5.17 a) and b). The difference in the profiles for the unwrapped phase with and without phase correction manifest as differences in the phase distribution in Figure 5.17 or the profiles in Figure 5.18.

The position of the introduced temporal wraps by spatial unwrapping changes depending on the postprocessing of the data after acquisition. Figure 5.17 illustrates the effect caused by handling the phase offset correction differently. In a) the phase offset correction was done before phase unwrapping and using a phase difference map and complex division (meaning the approach used in this project and described in the Methods section 4.1). In contrast, b) presents the phase when not corrected by phase offsets before unwrapping. In this case, the correction is performed during the linear fitting to combine the phase data (to generate the TFS map). In both cases, the temporal wrap produced by QG unwrapping occurs at different positions. The location of the wrap does not affect the performance of the unwrapping technique used to correct the evolution of phase with time (THUMPR). However, the phase distribution for each echo changes across all echoes, which is expected since in a) the phase distribution corresponding to the phase offset was removed (in contrast with b)).

The phase offset correction before unwrapping also caused fewer artifacts in the LFS map. This effect is shown in section 5.2.2 in Figure 5.20.

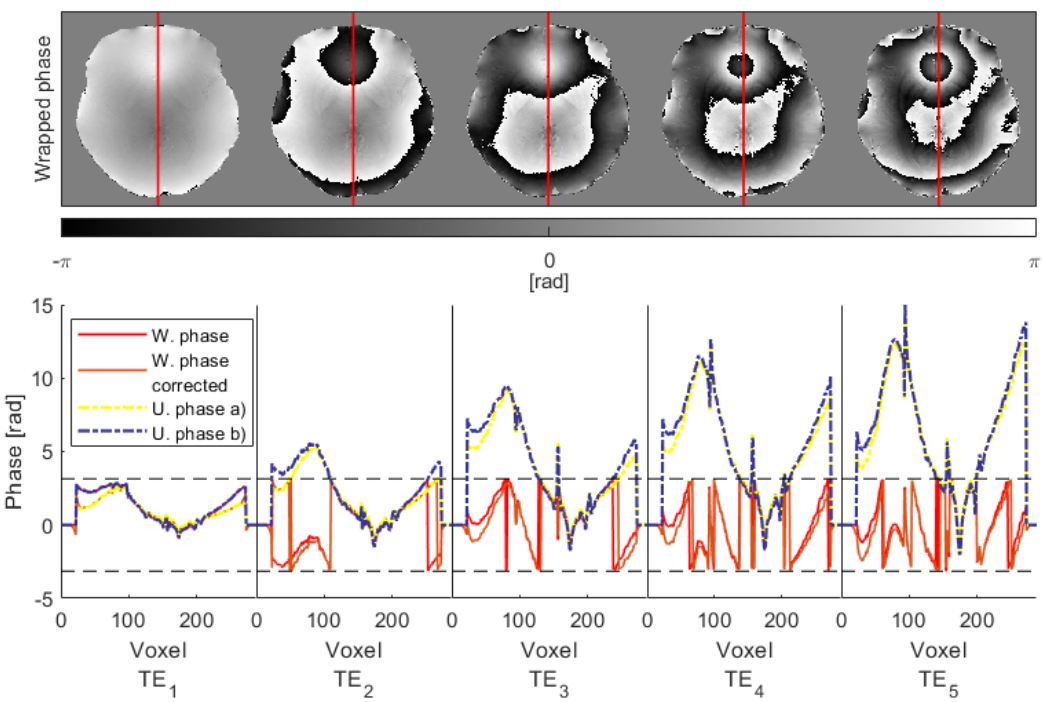


Figure 5.18: Wrapped phase in an axial slice and one-dimensional profiles to study the changes in wrapped and unwrapped phase (using QG) due to phase offset correction. The unwrapped phase including phase offset correction before unwrapping is labeled as "unwrapped phase a)", while without this correction it is labeled as "unwrapped phase b)". The data for this figure was obtained from dataset C2.

#### 5.2.2 Unwrapping and background removal techniques in conventional QSM

Visually, the best results for the calculated LFS maps were obtained with the methods paired with QG unwrapping, which lead to the maps with the least amount of background fields erroneously identified as local fields. Also, among the background removal techniques (paired with QG), PDF presented the least amount of background fields erroneously identified as local fields. These spurious local fields can be identified in Figure 5.19 as abnormally bright or dark regions in the LFS maps. Moreover, the errors at the edge of the brain when comparing PDF with LBV were gathered and highly constrained at the edges of the brain in PDF (orange arrows), while in LBV the artifacts that originated at the edges penetrated further inside the ROI (red arrows). The same trend was observed for all datasets collected in this study and these results are consistent with those from numerical simulations in Figure 5.3. For dataset D2, when comparing PDF and LBV (paired with QG) RMSE was 53.0 ppb. On the other hand, when comparing PDF and RESHARP and PDF

and LBV in an eroded mask (8 voxels) RMSE was 10.2 ppb and 23.9 ppb, respectively. Consequently, for calculating the susceptibility in deep gray matter structures, PDF and RESHARP would likely produce results more consistent with each other than LBV. On the other hand, the different interpretation of the local field close to the edges of the brain in LBV and PDF considerably increased (the RMSE doubles) the disagreement between these two methods.

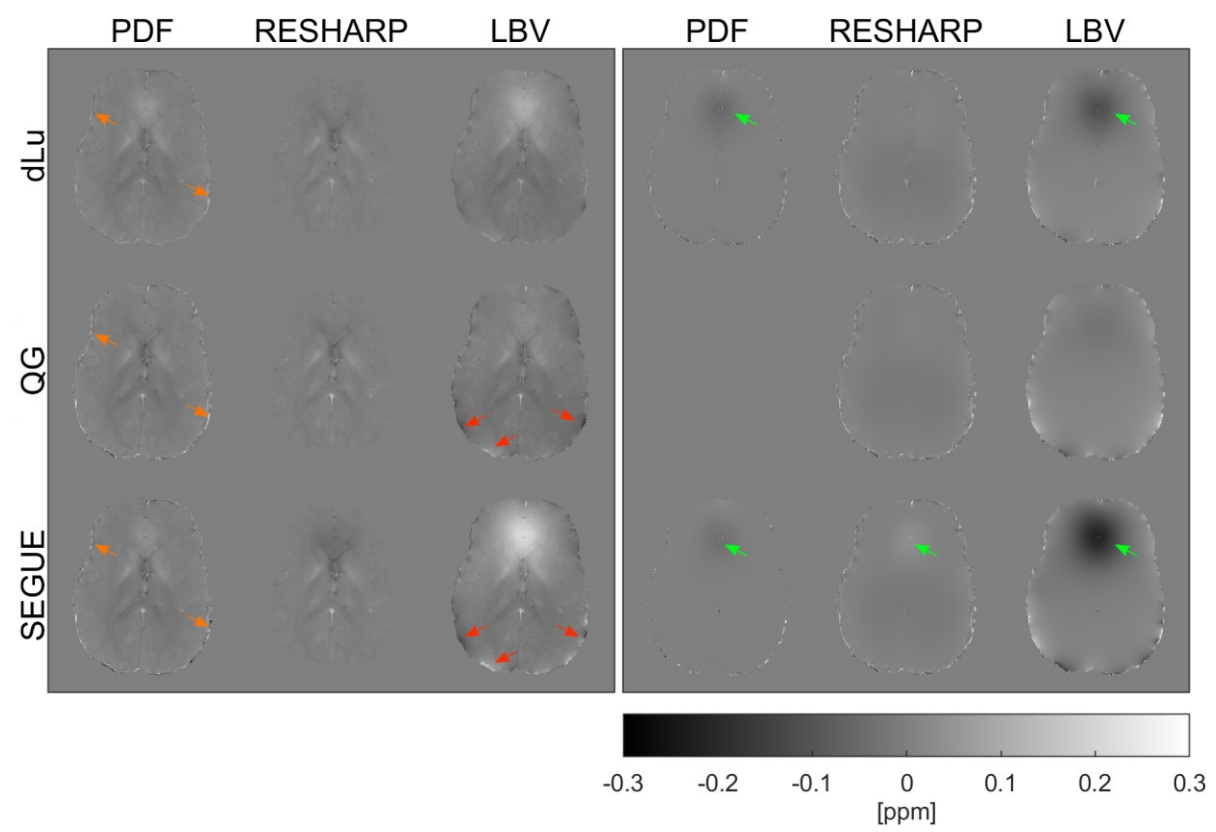


Figure 5.19: Comparison of background removal algorithms and the effect of unwrapping techniques on an in vivo dataset. The left image shows LFS maps. The right image shows difference maps for each LFS map using as ground truth the local magnetic field derived from the numerical model. The background removal techniques used were PDF, RESHARP (8 voxels radius), and LBV. The green arrows indicate examples of incorrectly identified local fields in the anterior region of the brain. The orange and red arrows indicate errors at the edges of the brain in PDF and LBV, respectively. The images showed correspond to dataset D2.

The quality of the LFS maps calculated after background removal was impacted by the approach considered for phase offset removal. By performing the phase offset removal before phase unwrapping, the presence of artifacts decreased in the calculated TFS and LFS maps as shown in

Figure 5.20. This figure shows the TFS (before background removal with PDF) and LFS (after background removal) maps (axial and sagittal) for dataset C2. When the phase offset correction was done during the weighted least square fit, after phase unwrapping, artifacts appeared in the inferior part of the brain. These artifacts appeared in both the TFS and LFS maps, and are indicated by arrows in Figure 5.20.

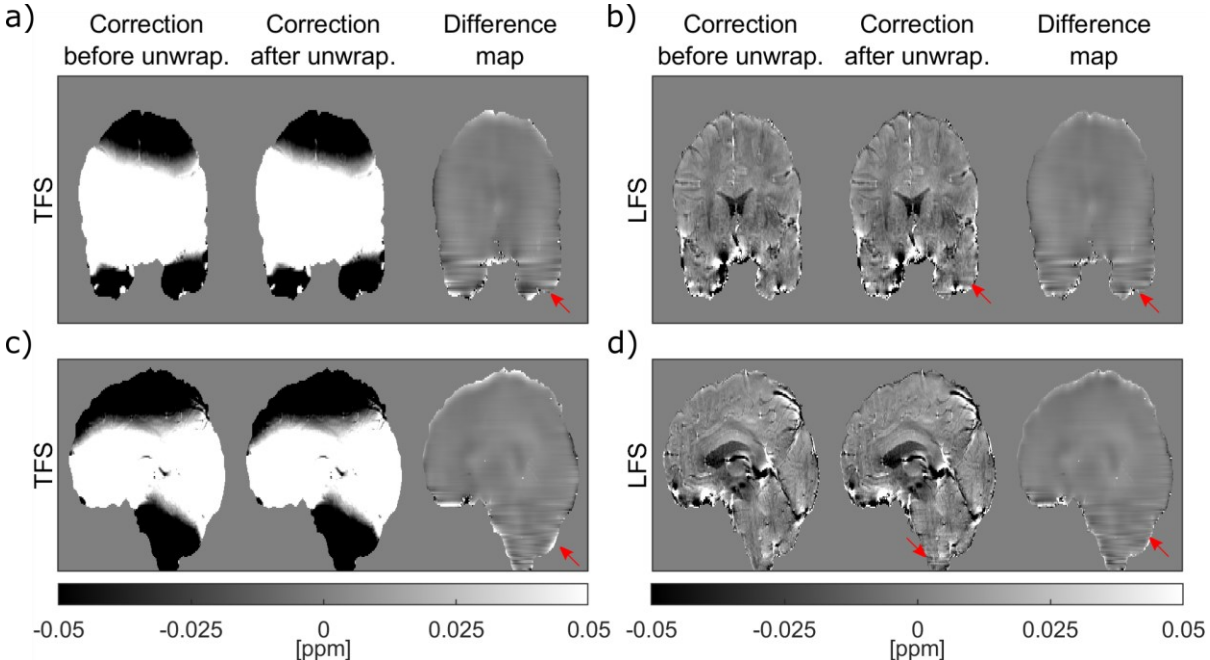


Figure 5.20: Effect of phase offset correction in TFS and LFS maps. a), b), c), and d) present the maps generated with different methods to calculate the phase offset correction and the corresponding difference maps. a) and c) are coronal and sagittal views of the TFS maps. b) and d) are LFS maps calculated using PDF. The arrows indicate artifacts that were present in the TFS and LFS maps when performing the phase offset correction during weighted least squares fit. The images showed correspond to dataset C2.

## 5.2.3 Evaluation of susceptibility maps using in vivo datasets

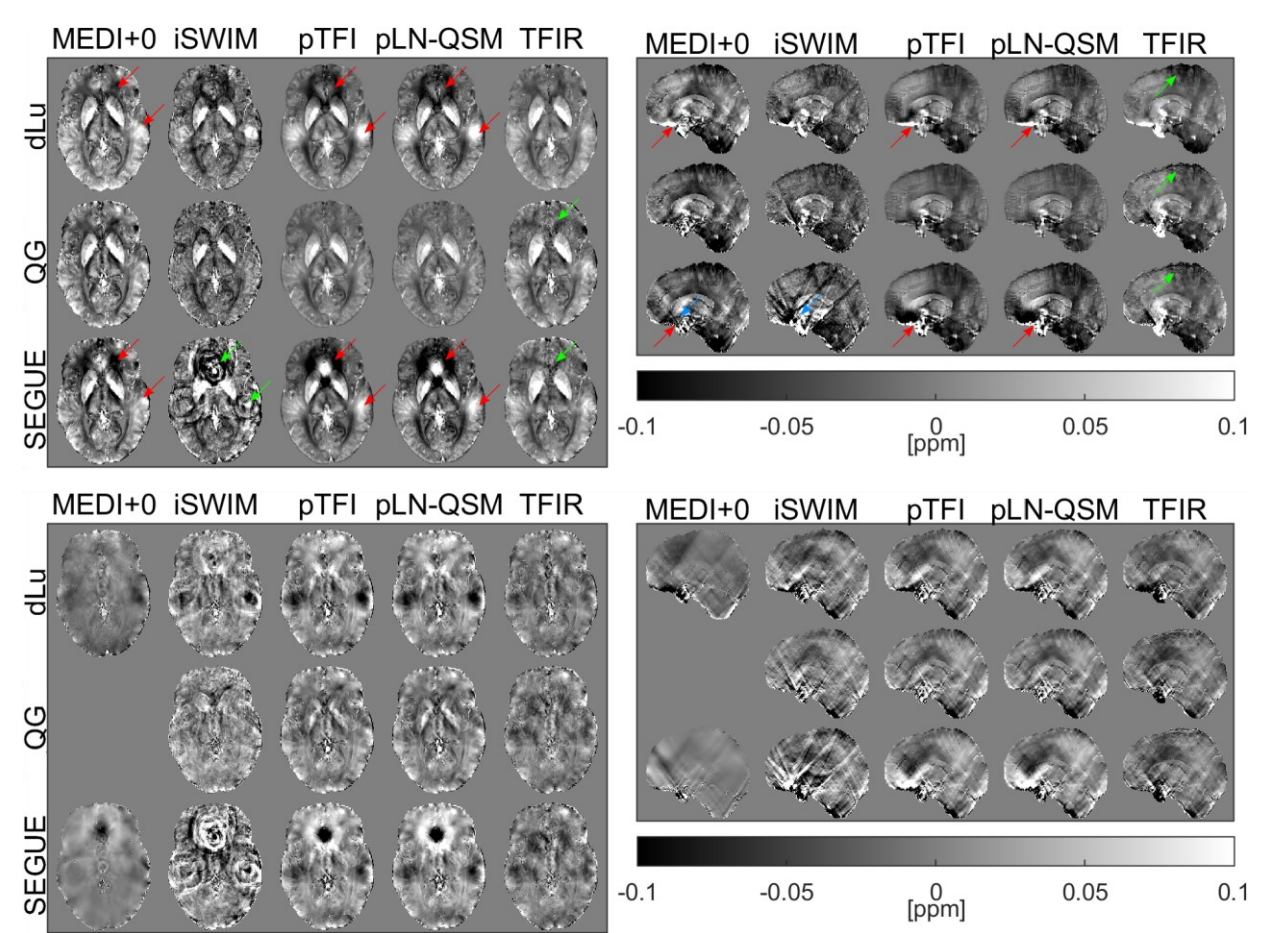


Figure 5.21: Susceptibility maps (superior image) and difference maps (inferior image) for all dipole inversion and direct inversion methods paired with different unwrapping techniques. All susceptibility maps were obtained from dataset C1. The difference maps were created using GQRG+PDF+MEDI+0. Red, green, and blue arrows indicate "bright and dark" artifacts, ringing artifacts, and streaking artifacts, respectively.

When comparing the performance of conventional QSM and direct inversion methods, the use of QG generated the susceptibility maps with the least amount of artifacts. Susceptibility maps obtained for each case in dataset C1 are displayed in Figure 5.21. The dynamic range was selected to highlight the artifacts present in the susceptibility maps. The susceptibility maps showed an increased number of "bright and dark" artifacts close to the anterior and lateral regions of the brain for SEGUE and dLu when paired with MEDI+0, pTFI, and pLN (red arrows). TFIR and iSWIM presented ringing artifacts that are more noticeable when pairing the techniques with SEGUE

(green arrows). MEDI+0 and iSWIM presented streaking artifacts that, similar to ringing artifacts, were more prominent when using SEGUE (blue arrows). The same trend was observed in all datasets.

In LN-QSM, the use of a preconditioner was indispensable to obtain acceptable quality susceptibility maps. The same preconditioner that was used in pTFI was also used in LN-QSM in all susceptibility maps shown in this project, using the method described as pLN-QSM. The effect of the preconditioner in LN-QSM is illustrated in Figure 5.22. Without a preconditioner and for a given number of iterations in the conjugate gradient algorithm, the quality of the susceptibility maps was noticeably worse when compared to the susceptibility maps that included the preconditioner.

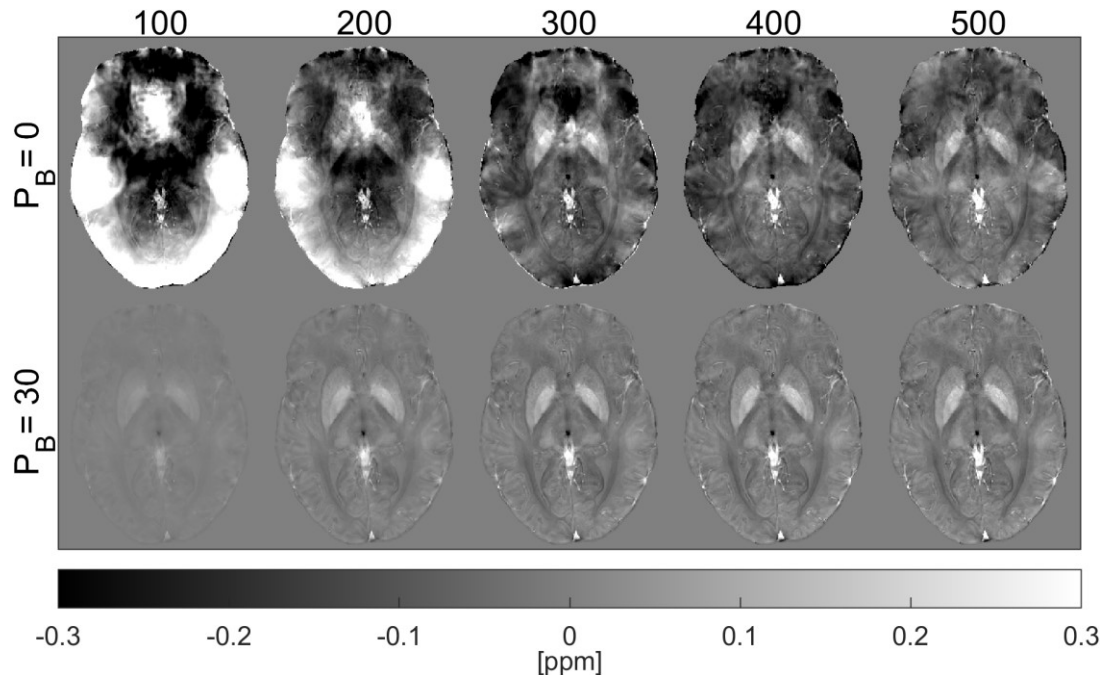


Figure 5.22: Effect of adding a preconditioner in LN-QSM. In the superior row, the image shows susceptibility maps obtained for LN-QSM without including a preconditioner ( $P_B = 0$ ). In the inferior row, the image shows susceptibility maps obtained for pLN-QSM, including the same preconditioner as in pTFI ( $P_B = 30$ ). In both cases, susceptibility maps for a different number of iterations in the conjugate gradient algorithm are shown. The iterations considered in the images are 100, 200, 300, 400, and 500. The susceptibility maps correspond to dataset C2.

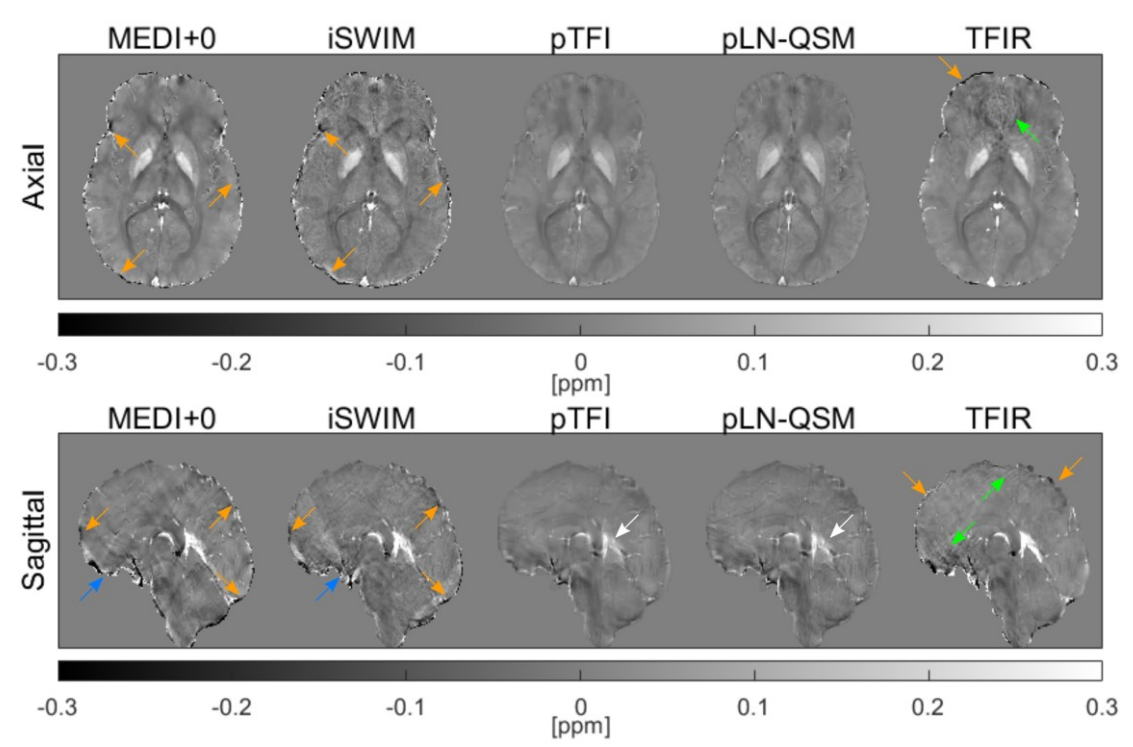


Figure 5.23: Axial and sagittal views for conventional QSM and direct inversion methods. All results were obtained with QG and PDF in the case of MEDI+0 and iSWIM. The susceptibility maps were obtained from dataset D1.

When comparing the susceptibility maps obtained for conventional QSM and direct inversion methods, fewer artifacts were observed in the susceptibility maps for pTFI and pLN-QSM. Figure 5.23 presents axial and sagittal views for the susceptibility maps obtained with all the techniques (paired with QG and PDF). Figure 5.23 is presented to allow a better visualization of the susceptibility maps presented in Figure 5.21. pTFI and pLN-QSM presented fewer streaking artifacts due to sinuses (blue arrows) and artifacts at the edges of the brain (orange arrows), as indicated in Figure 5.23 in conventional QSM. TFIR presents ringing artifacts in the anterior region of the brain (green arrows) and fewer artifacts at the edges when compared to MEDI+0 or iSWIM. pTFI and pLN-QSM produced susceptibility maps with a "softer" texture when compared with the other methods, which is observable in the sagittal view (white arrows) and the (relatively) less sharp depiction of vasculature in these two techniques.

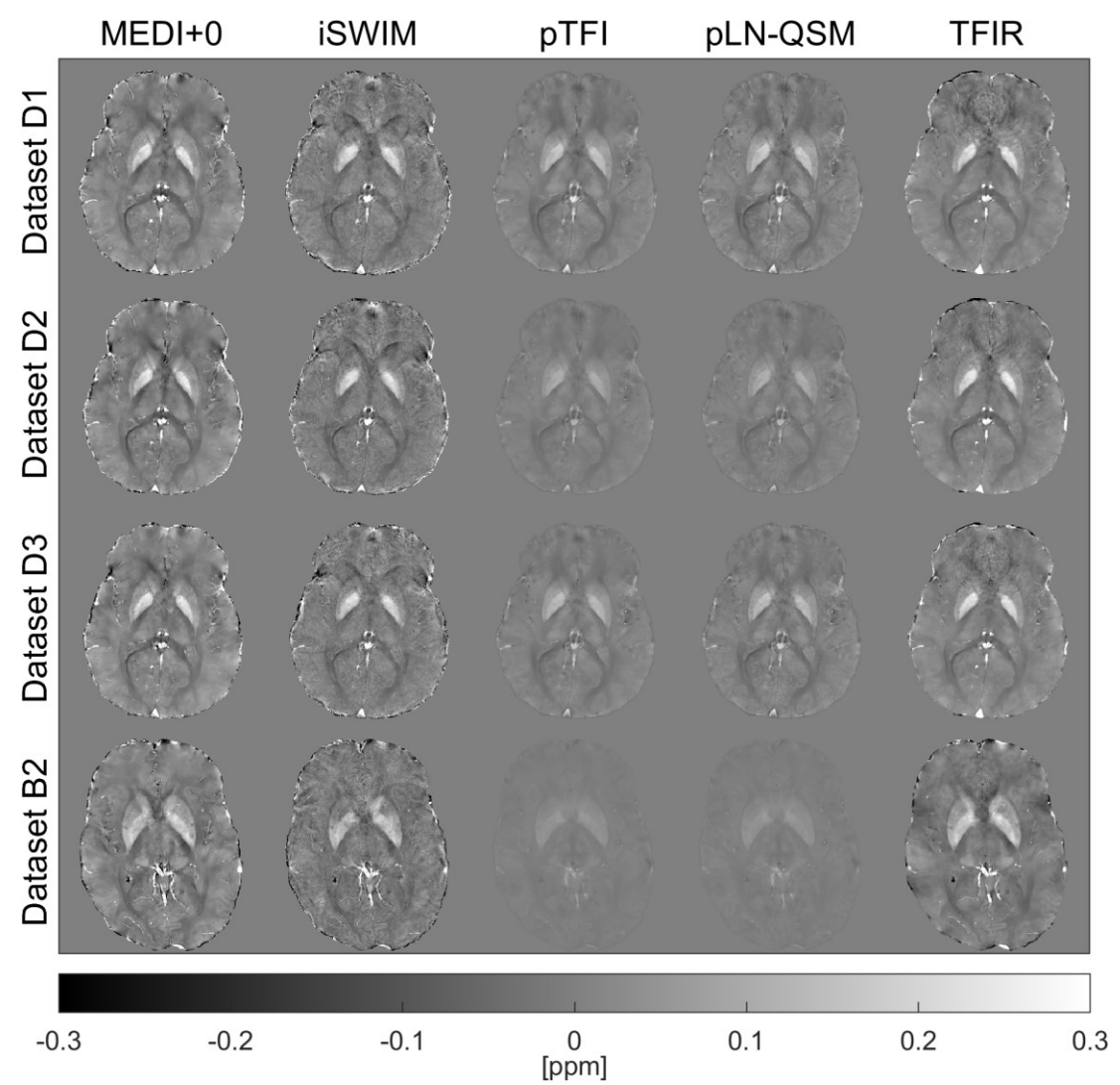


Figure 5.24: Systematic underestimation of susceptibility values in pTFI and pLN-QSM. These two techniques generate susceptibility maps with susceptibility values smaller than conventional QSM or TFIR. The figure also illustrates how this effect changes across datasets.

Direct inversion methods (pTFI and pLN-QSM) tended to estimate lower susceptibility values, especially for high susceptibility regions when compared to conventional QSM. This behavior was first noticed in numerical simulations (in the globus pallidus). The difference maps in Figure 5.21 show how pTFI and pLN-QSM differ from MEDI+0 in structures of high susceptibility like the putamen, globus pallidus, and caudate nucleus. However, in contrast to numerical simulations, for *in vivo* datasets, the tendency of estimating lower susceptibility values when compared to conventional QSM was more prominent all across the brain. The difference in susceptibility (lower values compared to conventional QSM) was visually perceptible in the susceptibility maps shown

in Figure 5.23. Moreover, the effect was variable depending on the dataset. This variability is illustrated in Figure 5.24, where datasets D1, D2, and D3 were selected to show the variability across the same volunteer, scanned the same day, with the bandwidth being the only parameter that changed across datasets. Dataset B1 was also included in this figure since this dataset presented the most extreme difference between pTFI and pLN-QSM and the other methods.

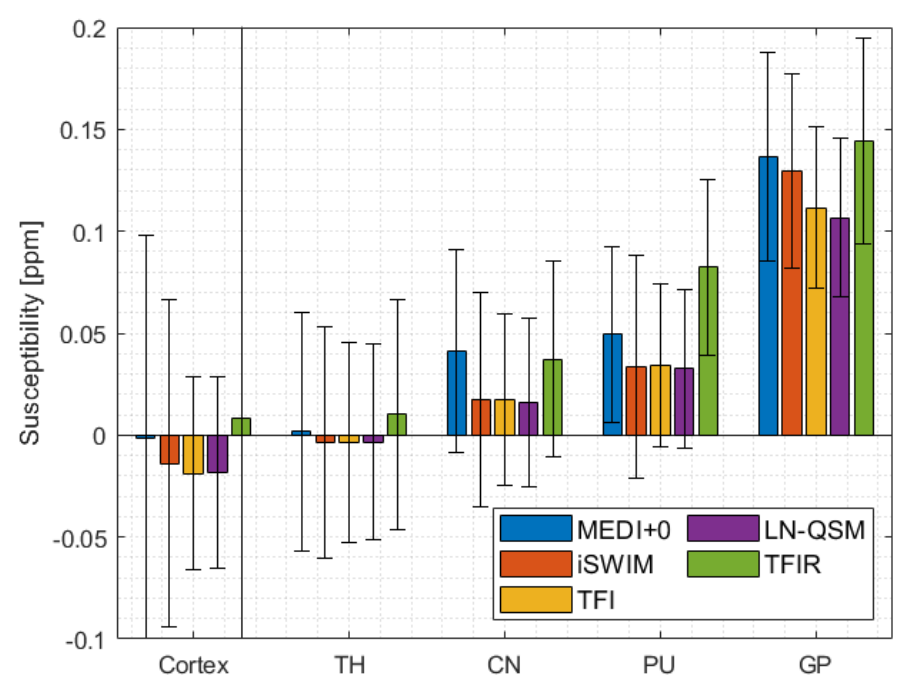


Figure 5.25: Bar plot of the mean and standard deviation in anatomical ROIs in dataset B1. The structures where the susceptibility was measured were the cortical region of the brain, thalamus (TH), caudate nucleus (CN), putamen (PU), and globus pallidus (GP).

When analyzing the values of the susceptibility in anatomical ROIs, the values measured for TH, CN, PU, and GP by pTFI and pLN-QSM were smaller than the values measured for MEDI+0. When comparing the values of these two techniques with iSWIM, the values were considerably smaller only in the GP. On the other hand, TFIR tended to produce higher susceptibility values than all other techniques in TH, CN, PU, and GP. In the case of the cortical region of the brain, TFIR was the only technique measuring positive susceptibility values, while all other techniques measured negative values. In the cortical region of the brain, pTFI and pLN-QSM measured comparable values for the susceptibility. The ANOVA performed to compare the effects of methods and ROI on the measured susceptibility values revealed that there was a statistically

significant difference between at least two methods. The *p* values for the two effects (methods and ROIs) and their interactions were well below 0.05. Post-hoc pairwise testing notably showed a significant difference between MEDI+0 and direct inversion methods (adjusted *p*-values values below 0.05). Since the numerical simulations indicated MEDI+0 as the most accurate conventional QSM method, the disagreement of MEDI+0 and direct inversion methods questions the reliability of pTFI, pLN-QSM, and TFIR in deep gray matter structures.

## Chapter 6

## **Discussion**

## 6.1 Evaluation of susceptibility maps using numerical simulations

## 6.1.1 Comparison of phase unwrapping algorithms

In numerical simulations, QG and SEGUE performed similarly according to the RMSE metric. QG was able to recover the true phase more accurately for early echoes and was more robust to noise when compared to SEGUE. On the other hand, SEGUE was more accurate for late echo times. This subtle difference between the accuracy of the methods depending on echo time contributes to QG being a better option for QSM. To combine the phase data, a weighted least square fit is used and the weights are proportional to the square of the magnitude signal [55]. Since the value of the magnitude decays with echo time, the data at earlier echoes is given higher weights. Higher accuracy in the unwrapped phase at early echoes could contribute to a better estimation of the total field shift (TFS) map.

In simulations, QG and SEGUE were more accurate than dLu, which significantly modified the retrieved phase. Despite modifying the phase, dLu led to more accurate susceptibility maps than SEGUE, based on smaller RMSE values and fewer artifacts for all cases. It was found that SEGUE tends to create regions of zero-valued voxels inside the brain (which was also observed for *in vivo* datasets and illustrated in Figure 5.16). This observation is consistent with the reported errors produced by SEGUE close to the sinuses [50]. However, the assigned zero value to these patches inside the volume-of-interest suggests that SEGUE is deliberately excluding these voxels from the calculation and labeling them as unreliable (instead of producing an incorrect unwrapped phase in these regions). These regions may be created during the "partitioning" step in the algorithm [47]. These regions propagate to the TFS after weighted least squares fit and they are interpreted during

the dipole inversion step as a steep change in the field, which produces artifacts. The failure of SEGUE in QSM shows that in addition to quantitative accuracy, smoothness and continuity are also desirable properties in the estimated phase.

The results show that dLu is the least accurate method. Although, the precision of dLu (compared to the other techniques) is unaffected by the increase of noise level. The lower accuracy of Laplacian unwrapping techniques is generally rooted in their inability to retrieve the exact phase and, depending on the implementation of boundary conditions, the introduction or removal of harmonic components when compared to the true phase. That said, the use of the Laplacian operators enforces smoothness in the calculated unwrapped phase and it makes these techniques more robust against noise [37]. Although not all Laplacian unwrapping techniques are created equal, the properties listed above are technically intrinsic to Laplacian unwrapping. Prioritizing Laplacian unwrapping over path-following techniques can be justified in scenarios where quantitative accuracy is not the main goal, as in SWI [97]. Laplacian unwrapping can be a good option in cases when sacrificing accuracy is justifiable in exchange for robustness to noise and a large amount of phase wraps or when the priority is to retrieve a smooth and continuous phase that still maintains enough structural information [50], [93].

## 6.1.2 Unwrapping and background removal techniques in conventional QSM

According to the results for the numerical simulations, the best performing method that does not require edge erosion was PDF. The different physical and mathematical assumptions driving the background removal algorithms explain the differences in the performance observed between the methods [2]. However, it is worthwhile to note that the background field in the numerical models was produced by susceptibility sources corresponding to anatomy simulated outside the brain. Thus, the background field in the numerical model is harmonic and produced by dipolar sources that are near the brain. This approach to simulate the background field is favorable for PDF. PDF models the background field by placing dipole sources outside the volume-of-interest but within the field of view (FOV) of the image, which corresponds to a model of the background field as a subspace of harmonic functions [58]. However, it has been reported in the literature that PDF cannot model background fields that are non-harmonic or that are harmonic but generated by

sources far from the brain. For example, this includes the background fields that are produced by the susceptibility change caused by the lungs/surrounding tissue interfaces [2].

The background field fitting approach in PDF outperformed spherical mean value filtration in RESHARP when comparing both methods in an eroded brain mask. Moreover, RESHARP (and for that matter, any variation of SHARP) requires edge erosion to remove the background field. The edge erosion is caused by the use of the spherical mean value (SMV) theorem to remove the harmonic contributions in the field caused by background fields [58]–[60]. Edge erosion renders this method inappropriate to measure susceptibility in cortical regions of the brain. Although, in this case, the method was included to evaluate how SMV filtration works when compared with the background field fitting that PDF performs. The worse performance of RESHARP when compared to PDF (in an eroded mask) can be explained due to averaging effect of SMV filtration that tends to suppress spatial information from the anatomy in the brain, producing flat LFS maps [98]. An aspect where RESHARP is better than PDF is to remove background fields due to non-harmonic contributions, which is possible due to the inclusion of Tikhonov regularization in the method [58], [60]. This aspect could not be evaluated since the background field was modeled only using harmonic contributions.

The goal of Tikhonov regularization in RESHARP is to suppress noise and error amplification when removing the background field [60]. Tikhonov regularization can also bring undesirable consequences like oversmoothing of the local field when a large regularization parameter is used [99], suppression of large and rapidly changing susceptibility (~0.3 ppm) regions [49], and an increase in artifacts (regularization artifacts) in the estimated local field [58]. In the numerical simulations presented in subsection 5.1.2, accuracy was greater with RESHARP than with SHARP (results not shown) in the description of deep gray matter structures, which is coherent with an other report [60]. Since this study was limited to brain parenchyma, no phase suppression as reported in [49] was observed. Finally, the numerical simulation considered in this work is basically a piecewise continuous model. Thus, it was not possible to evaluate if oversmoothing would affect the natural susceptibility variation within each of the structures added to the numerical model (since no natural variation or "texture" was added to the model). On the other

hand, oversmoothing did not appear to affect the resolution of the boundaries between the structures in the numerical model.

The errors at the edge of the brain in PDF and LBV are caused by violations of the physical assumptions close to the edges. In PDF, the assumption of orthogonality between the spaces spanned by background dipolar fields and local dipolar fields holds relatively well in the interior of the brain, but close to the edges the inner product between background and local fields is no longer close to zero—due to the spatial proximity between dipoles in the background and inside the brain—breaking the algorithm [56]. In LBV, the errors are not only constrained at the edges of the brain as showed in Figure 5.4, but high magnitude errors also appeared inside the eroded mask. In the case of SEGUE+LBV or QG+LBV, the errors at the edge of the brain are greater than in the eroded mask. The errors in LBV are caused due to erroneous boundary conditions introduced by an inaccurate brain mask. An inaccurate brain mask that extends beyond brain tissue introduces noisy voxels that produce incorrect boundary conditions. On the other hand, a brain mask that underestimated the extension of brain tissue introduces voxels where the value of the local field does not match the assumption of LBV [6], [58], [61].

#### 6.1.3 Evaluation of susceptibility maps using numerical simulations

To evaluate the susceptibility maps obtained from conventional QSM (MEDI+0 and iSWIM) and direct inversion (pTFI, pLN-QSM, and TFIR) methods, four approaches were considered. 1) In numerical models, the comparison of the estimated solution with the ground truth (when available) using difference maps and the RMSE as a quantitative metric was used to determine the accuracy of the methods. 2) For *in vivo* datasets, the evaluation of direct inversion methods was done through comparison with conventional QSM. 3) In numerical models and *in vivo* datasets, the performance of the methods was assessed by evaluating the susceptibility in anatomically relevant ROIs. 4) In numerical models and *in vivo* datasets, the evaluation of the visual appearance and artifacts spread across the brain was considered to determine the best method.

The use of the RMSE as the main quantitative metric was motivated by prior verification of its high correlation with other global metrics like Structural Similarity Index Measure (SSIM) and

High Frequency Error Norm (HFEN) [100]. In [100], it was also shown that the visual quality of the maps, qualitatively evaluated using a scale from 0 (best) to 3 (worst), correlated fairly well with the value of RMSE metrics. However, global metrics alone do not tell the full story since these metrics tend to favor reconstructed susceptibility maps that are over-smoothed or/and over-regularized [101]. Consequently, the analysis required additional qualitative visual inspection, evaluation of artifacts, and evaluation of accuracy in anatomically relevant ROIs. In the case of *in vivo* datasets, a quantitative comparison is more challenging since there is no ground truth or even a "gold standard" for comparison. Conventional QSM was chosen as a reference since the performance of these methods (MEDI+0 and iSWIM) is well documented in the literature. The best approach to evaluate QSM results is still an open question in simulation and *in vivo* datasets.

## 6.1.3.1 Unwrapping and background removal in QSM

In numerical model B, the best performing methods according to the RMSE metric were those paired with QG. This result was also consistent with improved visual quality and reduced artifacts compared to the methods paired with SEGUE or dLu. Considerable variations of the QSM result were observed depending on the combination of unwrapping technique and dipole inversion or direct inversion method.

Among conventional QSM methods, MEDI+0 produced better results than iSWIM, especially in model B. iSWIM iteratively adds information to k-space, while MEDI+0 includes L<sub>1</sub> regularization in the spatial domain. Although iSWIM reduces streaking artifacts, it has been shown in other works that MEDI-type solutions lead to better results [4], which is consistent with the results obtained in this work. However, one outcome of this project is that iSWIM failed to produce a satisfactory result when paired with SEGUE (in both numerical models). The zero-valued patches created by SEGUE when finding unreliable voxels considerably affect iSWIM performance. MEDI+0 was more robust against this type of effect produced during the unwrapping step in the numerical model B. This information can be interpreted as a cautionary tale for designing QSM techniques or for using existing methods in regions outside the brain. QSM methods that use information from the Fourier domain tend to require information throughout all space and they are generally unable to exclude information from specific spatial regions [2].

Moreover, the methods that operate over the Fourier space do not allow the addition of the same regularization added in the methods that work with spatial information.

Direct inversion methods presented similar artifacts to MEDI+0, which was expected since these methods also solve the problem in image space and use similar regularization. It was also observed that the range of susceptibility values estimated by TFIR differed from the range obtained from pTFI and pLN-QSM. The range of values in TFIR was biased towards the value of -0.033 ppm (WM), which corresponded to the largest number of voxels in the numerical model (this is illustrated in Figure 5.11). The modification in the dynamic range is a consequence of the spherical mean value (SMV) filtration included in TFIR, since SMV filtration causes bias towards high-frequency fitting [8]. By applying SMV filtration to the ground truth in the numerical model, it was observed that this low-frequency filter tends to favor keeping the information in some regions more than in others. This was especially true in WM in both numerical models, and it resulted in the observed susceptibility range modification.

## 6.1.3.2 Comparison of conventional QSM and direct inversion methods

When comparing the appearance of the susceptibility maps obtained with conventional QSM and direct inversion methods, pTFI and pLN-QSM presented fewer streaking artifacts and artifacts at the edges of the brain. TFIR also showed fewer streaking artifacts than conventional QSM, but ringing artifacts (in axial slces) appeared in the anterior region of the brain. However, it was observed that the susceptibility maps produced by direct inversion methods struggled to reproduce the structural features included in the numerical model, giving these susceptibility maps a "smoother" look when compared with conventional QSM (which was also observable in one-dimensional profiles). The simultaneous artifact suppression and "smoother" appearance of susceptibility maps in direct inversion methods are due to the regularization included in these methods akin to other QSM techniques that use regularization to solve the ill-posed inverse problem [36], [64], [73], [75].

The type and amount of regularization in QSM should be chosen according to the intended use of the susceptibility maps: namely, voxel-based study of the map, measurement of the susceptibility in anatomical ROIs, or visual inspection by radiologists [101]. The fact that pTFI and pLN-QSM produced the smallest RMSE values and the lack of artifact in numerical simulations and *in vivo* datasets suggests that these methods are well suited for voxel-based studies and even visual inspection by radiologists in regions close to the brain edge (due to the relatively small amount of artifacts in this region). On the other hand, the results in this thesis suggest that to quantitatively determine the susceptibility in anatomical regions, conventional QSM with MEDI+0 is a better alternative than direct inversion methods. Direct inversion methods are promising techniques thanks to reduced artifacts and reduced errors at the edge of the brain (when compared with conventional QSM). However, these methods' lack of refinement when solving the ill-posed inverse problem (as discussed further in subsection 6.1.3.4) or their questionable robustness/practicality (as discussed in subsection 6.2.3) are a signal that further development is required for this category of methods.

## 6.1.3.3 Decoding the operation of direct inversion problems

Direct inversion methods eliminate the explicit background removal step by estimating a susceptibility distribution outside the volume-of-interest (brain) that accurately reproduces the background field when compared to the ground truth. In simulations, there was a good agreement between the field derived from the susceptibility distribution outside the brain and the ground truth for the background field. This mechanism of action was already hinted at in the publications for each direct inversion method [6]–[10] when it was established that the susceptibility distribution  $\chi = \chi_L + \chi_B$  is estimated (for the susceptibility distribution  $\chi_L$ that produces the local field and the distribution  $\chi_B$  that produces the background field). Direct inversion methods are generally stated as unaffected by the imprecise separation between background and local fields when the physical and mathematical assumptions used in conventional background removal are broken (especially close to the edges of the volume-of-interest) [6], [7]. That said, there has yet to be an explanation of the principles that allow the separation between local and background fields in the case of direct inversion methods. Consequently, an explanation of how direct inversion methods operate is included below, along with an explanation of why these methods appear "immune" to the shortcomings of conventional background removal algorithms.

The direct inversion methods considered in this project rely on the same physical assumption as PDF, meaning that the background field is estimated by projecting the total field onto the space spanned by dipolar fields produced due to susceptibility variation outside the volume-of-interest (brain). To support this claim and to simplify the explanation (without losing generality), it is possible to consider the least-squares norm term in TFI with no preconditioning (meaning that the starting point from the derivation presented below corresponds to the least-squares term in equation 3.16, subsection 3.2.5.1) and state the problem in an equivalent form:

$$\begin{split} \left\| w \left[ \delta B - b_{\chi} * (\chi_{B} + \chi_{L}) \right] \right\|_{2}^{2} &= \left\| w \left[ \delta B - \left( b_{\chi} * \chi_{B} \right) - \left( b_{\chi} * \chi_{L} \right) \right] \right\|_{2}^{2} \\ &= \left\| w \left[ \delta B - B_{B} - B_{L} \right] \right\|_{2}^{2} \\ &= \left\| w \left[ \delta B - B_{B} \right] \right\|_{2}^{2} + \left\| w B_{L} \right\|_{2}^{2} - 2 \langle w \left[ \delta B - B_{B} \right], w B_{L} \rangle_{F} \end{split}$$

$$6.1$$

Here,  $B_B = (b_\chi * \chi_B)$ ,  $B_L = (b_\chi * \chi_L)$  and  $\langle , \rangle_F$  is the Frobenius inner product. For a detailed description of the notation used in this derivation, refer back to Chapter 3. Derivation 6.1 illustrates how direct inversion methods work. First, consider the minimum solution:

$$\min \| w[\delta B - b_{\chi} * (\chi_B + \chi_L)] \|_2^2 = 0$$
 6.2

When minimizing the new expression in 6.1, the zero value is obtained only when:

$$\|\mathbf{w}[\delta \mathbf{B} - \mathbf{B}_{\mathbf{B}}]\|_{2}^{2} + \|\mathbf{w}\mathbf{B}_{\mathbf{L}}\|_{2}^{2} = 2\langle \mathbf{w}[\delta \mathbf{B} - \mathbf{B}_{\mathbf{B}}], \mathbf{w}\mathbf{B}_{\mathbf{L}}\rangle_{\mathbf{F}}$$
 6.3

This solution is possible according to the projection theorem [56] only when  $\arg\min_{B_B} ||w| \delta B - B_B^*||_2^2 = B_B^*$  has a unique solution such that  $\delta B - B_B^* = B_L^*$  for  $B_B^*$  and  $B_L^*$ , the true background and local magnetic fields, respectively. Then, both sides of 6.3 are equal to two times the squared value of the Frobenius norm of the local magnetic field (times the weighting matrix w). Consequently, direct inversion methods also depend on the assumption of orthogonality between the spaces spanned by the background and local dipole fields. From a minimization problem standpoint, the terms in 6.1 can be interpreted as:

- The first term  $\|\mathbf{w}[\delta \mathbf{B} \mathbf{B}_{\mathbf{B}}]\|_{2}^{2}$  calculates the background field and is equivalent to PDF.
- The second and third terms  $\|\mathbf{w}\mathbf{B}_{\mathbf{L}}\|_{2}^{2}$  and  $2\langle \mathbf{w}[\delta \mathbf{B} \mathbf{B}_{\mathbf{B}}], \mathbf{w}\mathbf{B}_{\mathbf{L}}\rangle_{F}$  calculate the local field.

Although direct inversion methods use the same physical principles as PDF, the resulting susceptibility maps present fewer artifacts close to the edges of the brain and provide a more accurate description of the local/background field separation due to *a priori* information added to the model. Establishing a preconditioner in the susceptibility distribution as proposed in [6] is equivalent to *a priori* defining the background field as one or two orders of magnitude larger than the local field. Due to how the preconditioner is built, the established constraint (difference between local and background fields) "softens" towards the interior of the brain, which explains the better performance reported for pTFI close to the boundary of the brain [6]. On the other hand, PDF assumptions break down close to the boundary. But, by adding the preconditioner, the direct susceptibility reconstruction is aided in the regions where PDF breaks down. In the case of LN-QSM [7], the *a priori* information and the difference in magnitude between the local and background magnetic fields is supposedly introduced thanks to Tikhonov regularization. In this work it was found that Tikhonov regularization was not sufficient to create plausible susceptibility maps. This effect was illustrated in Figure 5.22 and will be discussed in subsection 6.2.3. TFIR [8] adds *a priori* information by including filtered R<sub>2</sub>\* information (equation 3.20).

## 6.1.3.4 Measurement of the susceptibility in anatomical ROIs

When studying the susceptibility in the deep gray matter structures included in numerical model B, MEDI+0 was the most accurate technique to estimate the susceptibility in the four structures included in the model. pTFI and pLN-QSM failed to estimate the susceptibility in the thalamus. TFIR also failed to estimate susceptibility accurately, especially in the thalamus and caudate, although it was the most accurate method in the globus pallidus and the only direct inversion method that estimated a negative mean susceptibility value for the thalamus. Relation 6.1 sheds some light on the explanation behind direct inversion methods failing to estimate susceptibility values in ROIs. pTFI includes *a priori* information added to the model to aid the separation between background and local magnetic fields [6] since the preconditioning will exclusively affect the terms in 6.1 containing the background field. On the other hand, the ill-posed inverse problem of estimating the susceptibility distribution from the local magnetic field is not aided with any additional information. In the case of pLN-QSM, extra regularization is added in the form of Tikhonov regularization. But this regularization is stated to aid the background/local field

separation [7]. Once again, no *a priori* information is added to the model to solve the ill-posed inverse problem. Moreover, even if Tikhonov regularization affects the estimation of the local susceptibility, the rather similar performance of this method compared to pTFI and the necessity of extra preconditioning (Figure 5.22) suggests that this is not the most appropriate way to aid the ill-posed inverse problem. Finally, TFIR performs a bit better in some structures thanks to the addition of  $R_2^*$  information (equation 3.20). The filtration required to include this information in the model brings new problems and the best way to include  $R_2^*$  information in direct inversion methods is still an open question [8].

For susceptibility measurements in the cortical region of the numerical brain, the only noticeable difference between models A and B was that the values measured in model A for pTFI and TFIR were slightly smaller when compared with model B. First, the intention behind having two different models was to determine if the presence of high susceptibility sources in the brain and consequently the increase of susceptibility dynamic range affects the measurement of the susceptibility in the cortical region of the brain. This approach was adopted since large susceptibility dynamic ranges degrade the quality of QSM, not only causing streaking artifacts but also altering the obtainable contrast and susceptibility values as observed in whole head QSM [7], one of the most extreme cases. The reasons why the values obtained in model A were slightly different from model B are still not entirely clear. One factor that contributed to the change in values between models was the "blurring" effect that QSM has over the numerical models considered. Discrete values corresponding to different structures were not recovered as sharp discrete values, but as highly blurred versions of the discrete distribution as in MEDI+0 or normally distributed susceptibility distributions in all other QSM techniques. By adding high susceptibility sources, the obtained susceptibility distributions were different when comparing models A and B. The "blurring" effect introduced by high susceptibility sources could affect the measurement in the cortical region of the brain.

#### 6.1.3.5 Susceptibility estimation for varying SNR

Lower SNR values produced more artifacts in the susceptibility maps, but the types of artifacts for each technique were different. The artifacts were more noticeable in iSWIM than in MEDI+0,

pTFI, pLN-QSM, and TFIR. This result was coherent with [102], where Bayesian methods that use noise weighting matrices dealt better with noise compared to other methods. In MEDI+0, pTFI, pLN-QSM, and TFIR the weighting matrix accounting for noise in the measurements contained the inverse of the standard deviation for each voxel [75].

In direct inversion methods, when measuring the susceptibility in anatomical ROIs, the change in SNR caused changes in the precision of the measurement and ad hoc shifts in the distribution of the susceptibility values for each region. The effect was more noticeable for deep grey matter structures than the cortical region of the brain. The change in the precision of the measurements was directly related to the noise level. With less noise, the precision of the measurements was better. On the other hand, the shift of the susceptibility distributions and the accompanying change in appearance of the susceptibility maps did not follow a clear trend with SNR. This shift is similar to the effect illustrated for *in vivo* datasets in Figure 5.24 and will be discussed in subsection 6.2.3.

## 6.2 Evaluation of susceptibility maps using in vivo datasets

## 6.2.1 Unwrapping algorithms comparison

In the measured datasets, the closest data to the "ground truth" for the unwrapped phase is the phase at early echoes when there are few phase wraps. When comparing the phase from the selected phase unwrapping algorithms with the "true" phase in axial slices, similar results to the numerical models were obtained. SEGUE and QG performed similarly according to the profiles studied in several axial slices for all datasets. SEGUE produced zero-valued patches close to regions of steep phase change as discussed in subsection 6.1.1. Finally, similar to the numerical models, dLu altered the phase when compared with the unwrapped phase of other techniques. The modified phase from dLu, similar to numerical simulation, was produced due to the use of the Laplacian operator [2], [58]

The phase offset correction step was implemented using a similar approach to the one proposed in [37], [82] but applied to the phase information combined over channels. This correction was performed since even if matched phase information is used to create the composite phase image

combined over channels [37], there might be time-independent contributions in the composite phase images that are not removed during phase matching or channel information combination [2]. By implementing the phase offset correction in the proposed way, instead of during the weighted least square fit to calculate the total field shift, fewer artifacts were observed in the TFS and LFS maps. By removing time-independent phase contributions before phase unwrapping, singularities (open-ended fringelines) are removed facilitating the operation of path-following phase unwrapping techniques [82]. Moreover, there is a possibility that an optimal SNR is achieved by removing the phase offset using a smooth version of the  $\phi_0$  map, which would improve the performance of unwrapping algorithms over the wrapped phase in each echo. This would be an effect similar to the one observed when considering the multi-channel phase difference combination method [37].

## 6.2.2 Unwrapping and background removal techniques in conventional QSM

For QSM of deep grey matter structures, PDF or RESHARP are suitable options for background removal in conventional QSM, while LBV was found as the method that differs the most when compared to the other techniques. In the entire brain, the disagreement between PDF and LBV just increases due to the different depictions of the local field close to the edges. The agreement between PDF and RESHARP can be explained since both techniques work by minimizing the norm of the internal field [58]. When comparing the errors at the edges of the brain it was observed that for *in vivo* datasets (and numerical simulations) the errors were more spread towards the interior of the brain, in contrast with the highly localized errors in PDF. This observation is consistent with a previous report [58], where the spread of the errors was explained due to violations of the assumption of zero local field at the boundary of the brain. Moreover, the better performance of PDF over LBV in the collected datasets and observed in this thesis is consistent with prior findings [50], where the same datasets were used to study the effect of temporal unwrapping. However, other sources have deemed LBV as the superior technique when compared with PDF [58], [103]. In the current work, PDF was selected due to the better performance in numerical models and the reduced amount of errors in the LFS map at the edge of the brain.

## 6.2.3 Evaluation of susceptibility maps using in vivo datasets

In terms of phase postprocessing, the optimal options (among the methods studied in this project) in conventional QSM are also the optimal algorithms for direct inversion methods. As discussed in subsection 6.2.1, the approach that generates fewer artifacts in both the LFS and TFS maps is to perform the phase offset correction before unwrapping. Since this approach produces a better description of the local and background fields, it is the better option (compared to removing the phase offset during the weighted least square fit) for conventional QSM and direct inversion methods. In determining the best unwrapping method for QSM, it was found that QG was the best option for conventional QSM and direct inversion methods. This result is consistent with the results obtained from the numerical simulations. Similar to numerical simulations, the discontinuities created by SEGUE considerably reduced the quality of the estimated susceptibility maps. Finally, similar to numerical simulations, dLu also altered the phase in the experimental data.

When comparing the susceptibility maps obtained in pTFI and pLN-QSM with conventional QSM, there was a visually perceptible difference in the values of susceptibility estimated in each case. This effect was observed for all datasets and it changed depending on the unwrapping technique and dataset. One possible explanation for the noticeable difference could be a suboptimal selection of regularization constants. This might bring into question either the robustness of pTFI and pLN-QSM or the practicality of these methods. In all cases, for the susceptibility reconstruction using direct inversion methods, the regularization parameters suggested in the original papers for each method were used [6]–[8] for QSM in a healthy brain. The degree to which the susceptibility values changed depending on the datasets or unwrapping technique indicates that, even after selecting the ideal parameters for one dataset, those parameters may not work for other datasets. Moreover, the "right" approach to selecting these parameters remains an open question. In only three different papers, there are four different ways to search for reconstruction parameters: minimizing the RMSE value when compared with a numerical model [6], L-curve criterion [7], minimizing the RMSE value when compared with the results of a conventional QSM technique (COSMOS) [8], and selecting the parameters empirically. Even if the right approach for direct inversion methods is to calculate a particular set of reconstruction parameters for every dataset, the methods listed

before require sweeping through many different values. Given the amount of computation time required for a single susceptibility map (which was between 1 to 5 hours using a workstation equipped with an i7-4770 CPU and 32 GB of RAM), pTFI and pLN-QSM would be impractical.

The use of a preconditioner in pLN-QSM considerably improved the quality of the calculated susceptibility maps. The use of a preconditioner is justified in this case since in [71], it is shown how the considered preconditioner in pTFI [6] is also compatible with Tikhonov regularization. Also, considering how the preconditioner is built (equation 3.18) and derivation 6.1, the preconditioner, in reality, does not affect the Tikhonov regularization term and only aids the separation of background and local fields. Thus, in this project, it was verified that Tikhonov regularization by itself is not enough to separate the background field from the local field. It was not possible to reproduce the results reported in [7] without the use of a preconditioner.

pTFI and pLN-QSM estimated lower susceptibility values when compared with MEDI+0 in deep gray matter anatomical structure ROIs, consistent with numerical simulations. Systematic estimation of lower susceptibility values (compared to conventional QSM) in some regions when using direct inversion methods has been previously reported, but there is conflicting information in the few publications available for this category of methods. In the original publications for pTFI [6] and LN-QSM [7], the tendency of the methods to produce lower susceptibility was not described. However, there is a clear consensus about the tendency of pTFI and LN-QSM to underestimate susceptibility (when compared to conventional QSM) [9] [8]. In [9], pTFI produced lower susceptibility values for the CN, GN, and PU when compared with COSMOS and MEDI, which coincides with the observed results in this project. In [8], LN-QSM (without preconditioning) was observed to estimate lower susceptibilities for CN, GN, PU, and TH compared with COSMOS. In [8], it was also demonstrated that pTFI presents higher or similar values for the mentioned structures but underestimated the values for other high susceptibility structures not considered in this thesis (substantia nigra and red nucleus).

When comparing the values of the estimated susceptibility in the cortical region of the brain, it was observed that the standard deviation is large compared to the mean value in MEDI+0, iSWIM, and TFIR. In conventional QSM, the large standard deviation is due to the increase number of

artifacts/errors at the boundary of the brain when compared to pTFI and pLN-QSM. On the other hand, the large standard deviation in TFIR is a consequence of the inability of SMV filtration to work properly close to the boundary of the brain. The standard deviation values in TH, CN, PU, and GP are coherent with the values expected for *in vivo* measurements [95].

#### 6.3 Limitations

The first limitation of this work was that the reconstructions parameters were not specifically recalculated for the QSM algorithms. All the parameters were used according to the values suggested in the literature or proposed in the original publication (of the algorithm) for QSM of a healthy brain. The best way to determine these parameters is still an open question. There are several alternatives as mentioned in subsection 6.2.3. Establishing the appropriate way to determine the set of reconstruction parameters for each case requires a systematic analysis of each option and the results that can be obtained. Also, a study of this magnitude will require considerable computational resources and/or time since many iterations with varying parameters must be performed.

In this project, susceptibility anisotropy and chemical shift of fat were not considered. For the direct inversion and dipole inversion algorithms (in the case of conventional QSM) only single-orientation QSM methods were considered and other methods like STI were not included. Consequently, the susceptibility was assumed as a scalar and isotropic property. This assumption breaks down in white matter where the susceptibility is an anisotropic property [5], [104]. The chemical shift of fat was ignored as healthy brain parenchyma does not contain any significant proportion of triglyceride signal. Chemical shift would need to be considered if the skull and scalp were to be included in the field inversion problem.

Only healthy brain QSM was considered for this project. Hemorrhages and calcifications in the brain can widely change the susceptibility of some structures and the range of susceptibility values in the brain [7], [89]. From the perspective of direct inversion methods, the reconstruction parameters between healthy and diseased brains change considerably and even finer spatial resolution could be required to achieve susceptibility maps with reasonably good quality.

Finally, the background field in numerical models was created according only to the field produced by the anatomy modeled outside and inside the brain. This approach was selected based on [89]. However, this approach implies that the background field does not contain non-harmonic contributions like B<sub>1</sub>-related field perturbations or that the model does not contain distant harmonic contributions like the air/tissue interface produced by the lungs [37], [58]. The best approach to model a realistic background field is still an open question. The code for a numerical brain model far more sophisticated than the one created for this thesis was recently released [86], but became available too late in the development of this thesis to be included.

# Chapter 7

## **Conclusions and future work**

#### 7.1 Conclusions

For this work, a QSM pipeline for conventional QSM and direct inversion methods was implemented and used to study and compare the susceptibility maps obtained with these two approaches for numerical simulation and *in vivo* datasets. It was determined that for conventional QSM the best combination of options for the different steps in the pipeline are phase offset correction through complex division before phase unwrapping, QG unwrapping, PDF background field removal, and MEDI+0 dipole inversion. For direct inversion methods, it was verified that the optimal options for phase data processing in conventional QSM also apply for direct inversion methods. In particular, QG was the best unwrapping technique for direct inversion methods.

It was shown that the operation of direct inversion methods depends on the assumption of orthogonality between the subspace spanned by all dipole fields inside the volume-of-interest and the subspace spanned by all dipole fields outside the volume-of-interest. Thus, direct inversion methods rely on the same physical/mathematical assumptions used in PDF. However, in contrast with PDF, the simultaneous estimation of the background field and local susceptibility distribution allows the introduction of *a priori* information in the model that aids the separation of background fields from local fields. This was especially noticeable in regions where PDF fails like the edge of the brain. The use of direct inversion methods such as pTFI and pLN-QSM resulted in fewer artifacts at the edge of the brain and overall more accurate techniques (as suggested by the RMSE metric) when compared with iSWIM or MEDI+0 (paired with PDF).

To measure the susceptibility in deep gray matter structures, conventional QSM is the better alternative when compared with direct inversion methods. From the methods considered in numerical simulations, MEDI+0 generated the closest susceptibility values to the ground truth for

all the structures included in the numerical model compared to direct inversion methods. On the other hand, pTFI and pLN-QSM systematically measured lower susceptibility values in deep gray matter structures in the experimental datasets, when compared with conventional QSM. TFIR solves some of the shortcomings of pTFI and pLN-QSM, but the use of spherical mean value filtration to introduce  $R_2^*$  information biases the solution and generates (relatively) more artifacts. All these factors together highlight the limitations of direct inversion methods to handle the ill-posed inversion problem of obtaining the susceptibility distribution from the magnetic field. Moreover, the lack of robustness and the impracticality of direct inversion methods is a consideration in choosing conventional QSM versus direct inversion methods for deep gray matter structures.

To measure the susceptibility in the cortical region of the brain, conventional QSM is not a suitable option due to the errors introduced close to the edge of the brain during background removal. Direct inversion methods are a promising set of techniques for this region due to the suppression of artifacts in this location, but a novel technique that improves over the lack of refinement when solving the ill-posed inverse is required.

#### 7.2 Future work

One of the conclusions derived from this project is that although direct inversion methods are a promising approach to solve the QSM problem and measure the susceptibility in the cortical region of the brain, current methods require further improvement. In direct inversion methods, the "name of the game" is *a priori* information. The model requires information to aid the separation of background and local fields, and information to aid the ill-posed inverse problem. pTFI and pLN-QSM contemplate adding information to improve the background/local field separation when compared to conventional QSM. TFIR adds additional information for the ill-posed inverse problem, but the approach to adding the information in the model is not optimal.

Future work building on this thesis could be focused on studying the *a priori* information required to improve direct inversion methods and the optimal way in which to include it in the model

One place to start this research would be to generalize the proposed dipole inversion technique named "structurally constrained Susceptibility Weighted Imaging and Mapping" scSWIM [40]. In direct inversion methods, similar to dipole inversion techniques, the least-squares term can be interpreted as the data fidelity term to estimate the total magnetic field shift [40]. The L<sub>1</sub> and L<sub>2</sub> regularization terms add structural feature-based constraints and voxel fidelity-based constraints, respectively [40]. scSWIM uses T1-weighted and R<sub>2</sub>\* information to enforce constraints accomplishing a reduction of streaking artifacts while preserving structural details. Thus, adapting some of the ideas presented in scSWIM to direct inversion methods could significantly improve the accuracy and visual quality of the susceptibility maps calculated with this category of techniques.

## References

- [1] E. M. Haacke, S. Liu, S. Buch, W. Zheng, D. Wu, and Y. Ye, "Quantitative susceptibility mapping: current status and future directions.," *Magn. Reson. Imaging*, vol. 33, no. 1, pp. 1–25, Jan. 2015, doi: 10.1016/j.mri.2014.09.004.
- [2] F. Schweser, A. Deistung, and J. R. Reichenbach, "Foundations of MRI phase imaging and processing for Quantitative Susceptibility Mapping (QSM).," *Z. Med. Phys.*, vol. 26, no. 1, pp. 6–34, Mar. 2016, doi: 10.1016/j.zemedi.2015.10.002.
- [3] F. Schweser, A. Deistung, B. W. Lehr, and J. R. Reichenbach, "Quantitative imaging of intrinsic magnetic tissue properties using MRI signal phase: An approach to in vivo brain iron metabolism?," *Neuroimage*, vol. 54, no. 4, pp. 2789–2807, 2011, doi: https://doi.org/10.1016/j.neuroimage.2010.10.070.
- [4] Y. Wang and T. Liu, "Quantitative susceptibility mapping (QSM): Decoding MRI data for a tissue magnetic biomarker.," *Magn. Reson. Med.*, vol. 73, no. 1, pp. 82–101, Jan. 2015, doi: 10.1002/mrm.25358.
- [5] C. Liu, H. Wei, N.-J. Gong, M. Cronin, R. Dibb, and K. Decker, "Quantitative Susceptibility Mapping: Contrast Mechanisms and Clinical Applications.," *Tomogr. (Ann Arbor, Mich.)*, vol. 1, no. 1, pp. 3–17, Sep. 2015, doi: 10.18383/j.tom.2015.00136.
- [6] Z. Liu, Y. Kee, D. Zhou, Y. Wang, and P. Spincemaille, "Preconditioned total field inversion (TFI) method for quantitative susceptibility mapping.," *Magn. Reson. Med.*, vol. 78, no. 1, pp. 303–315, Jul. 2017, doi: 10.1002/mrm.26331.
- [7] H. Sun, Y. Ma, M. E. MacDonald, and G. B. Pike, "Whole head quantitative susceptibility mapping using a least-norm direct dipole inversion method.," *Neuroimage*, vol. 179, pp. 166–175, Oct. 2018, doi: 10.1016/j.neuroimage.2018.06.036.
- [8] P. S. Balasubramanian, P. Spincemaille, L. Guo, W. Huang, I. Kovanlikaya, and Y. Wang, "Spatially Adaptive Regularization in Total Field Inversion for Quantitative Susceptibility Mapping," *iScience*, vol. 23, no. 10, p. 101553, Sep. 2020, doi: 10.1016/j.isci.2020.101553.
- [9] L. Zhang *et al.*, "Fast quantitative susceptibility reconstruction via total field inversion with improved weighted L(0) norm approximation.," *NMR Biomed.*, vol. 32, no. 5, p.

- e4067, May 2019, doi: 10.1002/nbm.4067.
- [10] Z. Liu *et al.*, "Automated adaptive preconditioner for quantitative susceptibility mapping," *Magn. Reson. Med.*, vol. 83, no. 1, pp. 271–285, Jan. 2020, doi: https://doi.org/10.1002/mrm.27900.
- [11] D. Nishimura, *Principles of Magnetic Resonance Imaging*. Stanford University, 1996.
- [12] R. Brown, Y. C. Cheng, E. M. Haacke, M. Thompson, and R. Venkatesan, *Magnetic Resonance Imaging*, vol. 9780471720. Chichester, UK: John Wiley & Sons Ltd, 2014.
- [13] F. Bloch, "Nuclear Induction," *Phys. Rev.*, vol. 70, no. 7–8, pp. 460–474, Oct. 1946, doi: 10.1103/PhysRev.70.460.
- [14] E. Purcell, H. Torrey, and R. Pound, "Resonance Absorption by Nuclear Magnetic Moments in a Solid," *Phys. Rev.*, vol. 69, no. 1–2, pp. 37–38, Jan. 1946, doi: 10.1103/PhysRev.69.37.
- [15] P. Lauterbur, "Image Formation by Induced Local Interactions: Examples Employing Nuclear Magnetic Resonance," *Nature*, vol. 242, no. 5394, pp. 190–191, 1973, doi: 10.1038/242190a0.
- [16] M. Kaila and R. Kaila, *Quantum Magnetic Resonance Imaging Diagnostics of Human Brain Disorders*. Elsevier Inc., 2010.
- [17] D. Plewes and W. Kucharczyk, "Physics of MRI: A primer," *J. Magn. Reson. Imaging*, vol. 35, no. 5, pp. 1038–1054, May 2012, doi: https://doi.org/10.1002/jmri.23642.
- [18] G. Stanisz *et al.*, "T1, T2 relaxation and magnetization transfer in tissue at 3T," *Magn. Reson. Med.*, vol. 54, no. 3, pp. 507–512, Sep. 2005, doi: https://doi.org/10.1002/mrm.20605.
- [19] S. Currie, N. Hoggard, I. J. Craven, M. Hadjivassiliou, and I. D. Wilkinson, "Understanding MRI: basic MR physics for physicians," *Postgrad. Med. J.*, vol. 89, no. 1050, pp. 209 LP 223, Apr. 2013, doi: 10.1136/postgradmedj-2012-131342.
- [20] R. Bitar *et al.*, "MR Pulse Sequences: What Every Radiologist Wants to Know but Is Afraid to Ask," *RadioGraphics*, vol. 26, no. 2, pp. 513–537, Mar. 2006, doi: 10.1148/rg.262055063.
- [21] D. McRobbie, E. Moore, M. Graves, and M. Prince, *MRI from Picture to Proton*, 2nd ed. Cambridge: Cambridge University Press, 2006.
- [22] R. Hashemi, W. Bradley, and C. Lisanti, "MRI: the basics." Wolters Kluwer Health,

- Philadelphia, 2018, [Online]. Available: https://search.ebscohost.com/login.aspx?direct=true&scope=site&db=nlebk&db=nlabk&AN=2013143.
- [23] A. Halefoglu and D. M. Yousem, "Susceptibility weighted imaging: Clinical applications and future directions.," *World J. Radiol.*, vol. 10, no. 4, pp. 30–45, Apr. 2018, doi: 10.4329/wjr.v10.i4.30.
- [24] Y. Wen *et al.*, "Cardiac quantitative susceptibility mapping (QSM) for heart chamber oxygenation," *Magn. Reson. Med.*, vol. 79, no. 3, pp. 1545–1552, Mar. 2018, doi: 10.1002/mrm.26808.
- [25] S. Sharma, D. Hernando, D. Horng, and S. Reeder, "Quantitative susceptibility mapping in the abdomen as an imaging biomarker of hepatic iron overload," *Magn. Reson. Med.*, vol. 74, no. 3, pp. 673–683, Sep. 2015, doi: 10.1002/mrm.25448.
- [26] E. Bechler *et al.*, "Feasibility of quantitative susceptibility mapping (QSM) of the human kidney.," *MAGMA*, Nov. 2020, doi: 10.1007/s10334-020-00895-9.
- [27] D. Griffiths, Introduction to Electrodynamics. Prentice Hall, 1999.
- [28] S. Blundell, Magnetism in Condensed Matter. OUP Oxford, 2001.
- [29] V. Iacovacci, "Magnetic Field-Based Technologies for Lab-on-a-Chip Applications," G. Lucarini, Ed. Rijeka: IntechOpen, 2016, p. Ch. 3.
- [30] J. Jackson, Classical Electrodynamics. Wiley, 2012.
- [31] G. M. Wysin, "Demagnetization Fields." Kansas State University, Manhattan, pp. 1–3, 2012, [Online]. Available: https://www.phys.ksu.edu/personal/wysin/notes/demag.pdf.
- [32] J. P. Marques and R. Bowtell, "Application of a Fourier-based method for rapid calculation of field inhomogeneity due to spatial variation of magnetic susceptibility," *Concepts Magn. Reson. Part B Magn. Reson. Eng.*, vol. 25B, no. 1, pp. 65–78, Apr. 2005, doi: https://doi.org/10.1002/cmr.b.20034.
- [33] K. Koch, X. Papademetris, D. Rothman, and R. de Graaf, "Rapid calculations of susceptibility-induced magnetostatic field perturbations for in vivo magnetic resonance.," *Phys. Med. Biol.*, vol. 51, no. 24, pp. 6381–6402, Dec. 2006, doi: 10.1088/0031-9155/51/24/007.
- [34] A. Deistung, F. Schweser, and J. R. Reichenbach, "Overview of quantitative susceptibility mapping," *NMR Biomed.*, vol. 30, no. 4, p. e3569, Apr. 2017, doi:

- https://doi.org/10.1002/nbm.3569.
- [35] K. Yu, Z. Ren, J. Li, S. Guo, Y. Hu, and Y. Li, "Direct visualization of deep brain stimulation targets in patients with Parkinson's disease via 3-T quantitative susceptibility mapping," *Acta Neurochir. (Wien).*, vol. 163, no. 5, pp. 1335–1345, 2021, doi: 10.1007/s00701-021-04715-4.
- [36] T. Liu, W. Xu, P. Spincemaille, A. S. Avestimehr, and Y. Wang, "Accuracy of the morphology enabled dipole inversion (MEDI) algorithm for quantitative susceptibility mapping in MRI," *IEEE Trans. Med. Imaging*, vol. 31, no. 3, pp. 816–824, Mar. 2012, doi: 10.1109/TMI.2011.2182523.
- [37] S. D. Robinson, K. Bredies, D. Khabipova, B. Dymerska, J. P. Marques, and F. Schweser, "An illustrated comparison of processing methods for MR phase imaging and QSM: combining array coil signals and phase unwrapping.," *NMR Biomed.*, vol. 30, no. 4, Apr. 2017, doi: 10.1002/nbm.3601.
- [38] D. H. Kim, N. Choi, S. M. Gho, J. Shin, and C. Liu, "Simultaneous imaging of in vivo conductivity and susceptibility," *Magn. Reson. Med.*, vol. 71, no. 3, pp. 1144–1150, Mar. 2014, doi: 10.1002/mrm.24759.
- [39] H. Sun *et al.*, "Extracting more for less: multi-echo MP2RAGE for simultaneous T1-weighted imaging, T1 mapping, mapping, SWI, and QSM from a single acquisition," *Magn. Reson. Med.*, vol. 83, no. 4, pp. 1178–1191, Apr. 2020, doi: https://doi.org/10.1002/mrm.27975.
- [40] S. Gharabaghi *et al.*, "Multi-Echo Quantitative Susceptibility Mapping for Strategically Acquired Gradient Echo (STAGE) Imaging," *Front. Neurosci.*, vol. 14, p. 581474, Oct. 2020, doi: 10.3389/fnins.2020.581474.
- [41] J. Li *et al.*, "Phase-corrected bipolar gradients in multi-echo gradient-echo sequences for quantitative susceptibility mapping," *MAGMA*, vol. 28, no. 4, pp. 347–355, Aug. 2015, doi: 10.1007/s10334-014-0470-3.
- [42] H. Sun, M. E. MacDonald, and G. B. Pike, "Phase Corretion of a Bipolar Gradient-Echo Acquisition for Quantitative Susceptibility Mapping," 2016.
- [43] S. Hirsch, J. Braun, and I. Sack, "Phase Unwrapping," in *Magnetic Resonance Elastography*, 2016, pp. 191–198.
- [44] X. Wang, S. Fang, X. Zhu, K. Kou, Y. Liu, and M. Jiao, "Phase unwrapping based on

- adaptive image in-painting of fringe patterns in measuring gear tooth flanks by laser interferometry," *Opt. Express*, vol. 28, no. 12, pp. 17881–17897, 2020, doi: 10.1364/OE.395453.
- [45] M. Gdeisat and F. Lilley, "One-Dimensional Phase Unwrapping Problem," Jan. 2011.
- [46] M. Jenkinson, "Fast, automated, N-dimensional phase-unwrapping algorithm.," *Magn. Reson. Med.*, vol. 49, no. 1, pp. 193–197, Jan. 2003, doi: 10.1002/mrm.10354.
- [47] A. Karsa and K. Shmueli, "SEGUE: A Speedy rEgion-Growing Algorithm for Unwrapping Estimated Phase.," *IEEE Trans. Med. Imaging*, vol. 38, no. 6, pp. 1347–1357, Jun. 2019, doi: 10.1109/TMI.2018.2884093.
- [48] J. Dong *et al.*, "Simultaneous phase unwrapping and removal of chemical shift (SPURS) using graph cuts: application in quantitative susceptibility mapping.," *IEEE Trans. Med. Imaging*, vol. 34, no. 2, pp. 531–540, Feb. 2015, doi: 10.1109/TMI.2014.2361764.
- [49] V. Fortier and I. R. Levesque, "Phase processing for quantitative susceptibility mapping of regions with large susceptibility and lack of signal," *Magn. Reson. Med.*, vol. 79, no. 6, pp. 3103–3113, Jun. 2018, doi: https://doi.org/10.1002/mrm.26989.
- [50] A. Ensworth, "Robuts phase pre-processing for quantitative susceptibility mapping (MSc Thesis)," McGill University, Montreal, 2020.
- [51] H. Abdul-Rahman, M. Gdeisat, D. Burton, M. Lalor, F. Lilley, and C. Moore, "Fast and robust three-dimensional best path phase unwrapping algorithm," *Appl. Opt.*, vol. 46, no. 26, pp. 6623–6635, 2007, doi: 10.1364/AO.46.006623.
- [52] S. Robinson, H. Schödl, and S. Trattnig, "A method for unwrapping highly wrapped multi-echo phase images at very high field: UMPIRE," *Magn. Reson. Med.*, vol. 72, no. 1, pp. 80–92, Jul. 2014, doi: 10.1002/mrm.24897.
- [53] C. Shalazi, "Lecture 24-25: Weighted and Generalized Least Squares." Carnegie Mellon University, Pittsburgh, 2015, [Online]. Available: https://www.stat.cmu.edu/~cshalizi/mreg/15/lectures/24/lecture-24--25.pdf.
- [54] D. Pandian, C. Ciulla, E. M. Haacke, J. Jiang, and M. Ayaz, "Complex threshold method for identifying pixels that contain predominantly noise in magnetic resonance images.," *J. Magn. Reson. Imaging*, vol. 28, no. 3, pp. 727–735, Sep. 2008, doi: 10.1002/jmri.21487.
- [55] B. Wu, W. Li, A. V. Avram, S.-M. Gho, and C. Liu, "Fast and tissue-optimized mapping of magnetic susceptibility and T2\* with multi-echo and multi-shot spirals.," *Neuroimage*,

- vol. 59, no. 1, pp. 297–305, Jan. 2012, doi: 10.1016/j.neuroimage.2011.07.019.
- [56] T. Liu *et al.*, "A novel background field removal method for MRI using projection onto dipole fields (PDF)," *NMR Biomed.*, vol. 24, no. 9, pp. 1129–1136, Nov. 2011, doi: https://doi.org/10.1002/nbm.1670.
- [57] F. Schweser, B. Lehr, and A. Deistung, *Sophisticated Harmonic Artifact Reduction for Phase Data (SHARP)*. 2010.
- [58] F. Schweser, S. D. Robinson, L. de Rochefort, W. Li, and K. Bredies, "An illustrated comparison of processing methods for phase MRI and QSM: removal of background field contributions from sources outside the region of interest.," *NMR Biomed.*, vol. 30, no. 4, Apr. 2017, doi: 10.1002/nbm.3604.
- [59] P. S. Özbay, A. Deistung, X. Feng, D. Nanz, J. R. Reichenbach, and F. Schweser, "A comprehensive numerical analysis of background phase correction with V-SHARP," *NMR Biomed.*, vol. 30, no. 4, p. 10.1002/nbm.3550, Apr. 2017, doi: 10.1002/nbm.3550.
- [60] H. Sun and A. H. Wilman, "Background field removal using spherical mean value filtering and Tikhonov regularization," *Magn. Reson. Med.*, vol. 71, no. 3, pp. 1151–1157, Mar. 2014, doi: https://doi.org/10.1002/mrm.24765.
- [61] D. Zhou, T. Liu, P. Spincemaille, and Y. Wang, "Background field removal by solving the Laplacian boundary value problem," *NMR Biomed.*, vol. 27, no. 3, pp. 312–319, Mar. 2014, doi: https://doi.org/10.1002/nbm.3064.
- [62] W. Li, A. V Avram, B. Wu, X. Xiao, and C. Liu, "Integrated Laplacian-based phase unwrapping and background phase removal for quantitative susceptibility mapping.," *NMR Biomed.*, vol. 27, no. 2, pp. 219–227, Feb. 2014, doi: 10.1002/nbm.3056.
- [63] F. Schweser, A. Deistung, K. Sommer, and J. R. Reichenbach, "Toward online reconstruction of quantitative susceptibility maps: Superfast dipole inversion," *Magn. Reson. Med.*, vol. 69, no. 6, pp. 1581–1593, Jun. 2013, doi: https://doi.org/10.1002/mrm.24405.
- [64] B. Bilgic *et al.*, "Fast image reconstruction with L2-regularization," *J. Magn. Reson. Imaging*, vol. 40, no. 1, pp. 181–191, Jul. 2014, doi: https://doi.org/10.1002/jmri.24365.
- [65] B. Wu, W. Li, A. Guidon, and C. Liu, "Whole brain susceptibility mapping using compressed sensing.," *Magn. Reson. Med.*, vol. 67, no. 1, pp. 137–147, Jan. 2012, doi: 10.1002/mrm.23000.

- [66] T. Liu *et al.*, "Morphology enabled dipole inversion (MEDI) from a single-angle acquisition: comparison with COSMOS in human brain imaging.," *Magn. Reson. Med.*, vol. 66, no. 3, pp. 777–783, Sep. 2011, doi: 10.1002/mrm.22816.
- [67] J. Tang, S. Liu, J. Neelavalli, Y. C. N. Cheng, S. Buch, and E. M. Haacke, "Improving susceptibility mapping using a threshold-based K-space/image domain iterative reconstruction approach," *Magn. Reson. Med.*, vol. 69, no. 5, pp. 1396–1407, May 2013, doi: https://doi.org/10.1002/mrm.24384.
- [68] C. Milovic, B. Bilgic, B. Zhao, J. Acosta-Cabronero, and C. Tejos, "Fast nonlinear susceptibility inversion with variational regularization.," *Magn. Reson. Med.*, vol. 80, no. 2, pp. 814–821, Aug. 2018, doi: 10.1002/mrm.27073.
- [69] C. Langkammer *et al.*, "Fast quantitative susceptibility mapping using 3D EPI and total generalized variation.," *Neuroimage*, vol. 111, pp. 622–630, May 2015, doi: 10.1016/j.neuroimage.2015.02.041.
- [70] I. Chatnuntawech *et al.*, "Single-step quantitative susceptibility mapping with variational penalties," *NMR Biomed.*, vol. 30, no. 4, p. e3570, Apr. 2017, doi: https://doi.org/10.1002/nbm.3570.
- [71] D. Calvetti and E. Somersalo, "Priorconditioners for linear systems," *Inverse Probl.*, vol. 21, no. 4, pp. 1397–1418, 2005, doi: 10.1088/0266-5611/21/4/014.
- [72] J. Liu *et al.*, "Morphology enabled dipole inversion for quantitative susceptibility mapping using structural consistency between the magnitude image and the susceptibility map," *Neuroimage*, vol. 59, no. 3, pp. 2560–2568, Feb. 2012, doi: 10.1016/j.neuroimage.2011.08.082.
- [73] B. Bilgic *et al.*, "Fast quantitative susceptibility mapping with L1-regularization and automatic parameter selection," *Magn. Reson. Med.*, vol. 72, no. 5, pp. 1444–1459, Nov. 2014, doi: 10.1002/mrm.25029.
- [74] D. S. Holder, *Electrical Impedance Tomography: Methods, History and Applications*. CRC Press, 2004.
- [75] L. de Rochefort *et al.*, "Quantitative susceptibility map reconstruction from MR phase data using bayesian regularization: Validation and application to brain imaging," *Magn. Reson. Med.*, vol. 63, no. 1, pp. 194–206, Jan. 2010, doi: https://doi.org/10.1002/mrm.22187.

- [76] H. Sun and A. H. Wilman, "Quantitative susceptibility mapping using single-shot echoplanar imaging.," *Magn. Reson. Med.*, vol. 73, no. 5, pp. 1932–1938, May 2015, doi: 10.1002/mrm.25316.
- [77] A. P. Fan *et al.*, "Quantitative oxygenation venography from MRI phase.," *Magn. Reson. Med.*, vol. 72, no. 1, pp. 149–159, Jul. 2014, doi: 10.1002/mrm.24918.
- [78] B. Bilgic, A. Pfefferbaum, T. Rohlfing, E. V Sullivan, and E. Adalsteinsson, "MRI estimates of brain iron concentration in normal aging using quantitative susceptibility mapping.," *Neuroimage*, vol. 59, no. 3, pp. 2625–2635, Feb. 2012, doi: 10.1016/j.neuroimage.2011.08.077.
- [79] S. M. Smith, "Fast robust automated brain extraction.," *Hum. Brain Mapp.*, vol. 17, no. 3, pp. 143–155, Nov. 2002, doi: 10.1002/hbm.10062.
- [80] M. Jenkinson, C. F. Beckmann, T. E. J. Behrens, M. W. Woolrich, and S. M. Smith, "FSL.," *Neuroimage*, vol. 62, no. 2, pp. 782–790, Aug. 2012, doi: 10.1016/j.neuroimage.2011.09.015.
- [81] M. W. Woolrich *et al.*, "Bayesian analysis of neuroimaging data in FSL.," *Neuroimage*, vol. 45, no. 1 Suppl, pp. S173-86, Mar. 2009, doi: 10.1016/j.neuroimage.2008.10.055.
- [82] S. Hongfu, "Quantitative Susceptibility Mapping in Human Brain: Methods Development and Applications," University of Alberta, 2015.
- [83] M. Pei *et al.*, "Algorithm for fast monoexponential fitting based on Auto-Regression on Linear Operations (ARLO) of data," *Magn. Reson. Med.*, vol. 73, no. 2, pp. 843–850, Feb. 2015, doi: https://doi.org/10.1002/mrm.25137.
- [84] X. Feng, A. Deistung, and J. R. Reichenbach, "Quantitative susceptibility mapping (QSM) and R 2 \* in the human brain at 3 T Evaluation of intra-scanner repeatability," *Zeitschrift fßr Medizinische Phys.*, 2017, doi: 10.1016/j.zemedi.2017.05.003.
- [85] Z. Liu, P. Spincemaille, Y. Yao, Y. Zhang, and Y. Wang, "MEDI+0: Morphology enabled dipole inversion with automatic uniform cerebrospinal fluid zero reference for quantitative susceptibility mapping," *Magn. Reson. Med.*, vol. 79, no. 5, pp. 2795–2803, May 2018, doi: https://doi.org/10.1002/mrm.26946.
- [86] S. Straub *et al.*, "Suitable reference tissues for quantitative susceptibility mapping of the brain.," *Magn. Reson. Med.*, vol. 78, no. 1, pp. 204–214, Jul. 2017, doi: 10.1002/mrm.26369.

- [87] S. Buch, S. Liu, Y. Ye, Y.-C. N. Cheng, J. Neelavalli, and E. M. Haacke, "Susceptibility mapping of air, bone, and calcium in the head.," *Magn. Reson. Med.*, vol. 73, no. 6, pp. 2185–2194, Jun. 2015, doi: 10.1002/mrm.25350.
- [88] S. Wharton and R. Bowtell, "Whole-brain susceptibility mapping at high field: a comparison of multiple- and single-orientation methods.," *Neuroimage*, vol. 53, no. 2, pp. 515–525, Nov. 2010, doi: 10.1016/j.neuroimage.2010.06.070.
- [89] J. P. Marques *et al.*, "QSM reconstruction challenge 2.0: A realistic in silico head phantom for MRI data simulation and evaluation of susceptibility mapping procedures.," *Magn. Reson. Med.*, vol. 86, no. 1, pp. 526–542, Jul. 2021, doi: 10.1002/mrm.28716.
- [90] Z. Hu and S. T. Acton, "Morphological pyramid image registration," in *4th IEEE Southwest Symposium on Image Analysis and Interpretation*, 2000, pp. 227–231, doi: 10.1109/IAI.2000.839604.
- [91] D. Shattuck *et al.*, "Semi-automated method for delineation of landmarks on models of the cerebral cortex.," *J. Neurosci. Methods*, vol. 178, no. 2, pp. 385–392, Apr. 2009, doi: 10.1016/j.jneumeth.2008.12.025.
- [92] D. Shattuck and R. Leahy, "BrainSuite: an automated cortical surface identification tool.," *Med. Image Anal.*, vol. 6, no. 2, pp. 129–142, Jun. 2002, doi: 10.1016/s1361-8415(02)00054-3.
- [93] K.-S. Chan and J. P. Marques, "SEPIA—Susceptibility mapping pipeline tool for phase images," *Neuroimage*, vol. 227, p. 117611, 2021, doi: https://doi.org/10.1016/j.neuroimage.2020.117611.
- [94] R. Wang *et al.*, "Stability of R2\* and quantitative susceptibility mapping of the brain tissue in a large scale multi-center study," *Sci. Rep.*, vol. 7, p. 45261, Mar. 2017, doi: 10.1038/srep45261.
- [95] P.-Y. Lin, T.-C. Chao, and M.-L. Wu, "Quantitative susceptibility mapping of human brain at 3T: a multisite reproducibility study," *AJNR. Am. J. Neuroradiol.*, vol. 36, no. 3, pp. 467–474, Mar. 2015, doi: 10.3174/ajnr.A4137.
- [96] F. Cribari-Neto, "Asymptotic inference under heteroskedasticity of unknown form," *Comput. Stat. Data Anal.*, vol. 45, no. 2, pp. 215–233, 2004, doi: https://doi.org/10.1016/S0167-9473(02)00366-3.
- [97] K. Eckstein et al., "Improved susceptibility weighted imaging at ultra-high field using

- bipolar multi-echo acquisition and optimized image processing: CLEAR-SWI," *Neuroimage*, vol. 237, p. 118175, 2021, doi: https://doi.org/10.1016/j.neuroimage.2021.118175.
- [98] S. Bollmann *et al.*, "SHARQnet Sophisticated harmonic artifact reduction in quantitative susceptibility mapping using a deep convolutional neural network.," *Z. Med. Phys.*, vol. 29, no. 2, pp. 139–149, May 2019, doi: 10.1016/j.zemedi.2019.01.001.
- [99] J. Fang, L. Bao, X. Li, P. C. M. van Zijl, and Z. Chen, "Background field removal for susceptibility mapping of human brain with large susceptibility variations," *Magn. Reson. Med.*, vol. 81, no. 3, pp. 2025–2037, Mar. 2019, doi: https://doi.org/10.1002/mrm.27492.
- [100] B. Bilgic, C. Langkammer, J. P. Marques, J. Meineke, C. Milovic, and F. Schweser, "QSM reconstruction challenge 2.0: Design and report of results," *Magn. Reson. Med.*, vol. 86, no. 3, pp. 1241–1255, Sep. 2021, doi: https://doi.org/10.1002/mrm.28754.
- [101] C. Langkammer *et al.*, "Quantitative susceptibility mapping: Report from the 2016 reconstruction challenge," *Magn. Reson. Med.*, vol. 79, no. 3, pp. 1661–1673, Mar. 2018, doi: https://doi.org/10.1002/mrm.26830.
- [102] S. Wang *et al.*, "Noise Effects in Various Quantitative Susceptibility Mapping Methods," *IEEE Trans. Biomed. Eng.*, vol. 60, no. 12, pp. 3441–3448, Dec. 2013, doi: 10.1109/TBME.2013.2266795.
- [103] M. Wu *et al.*, "Correction of motion-induced susceptibility artifacts and B0 drift during proton resonance frequency shift-based MR thermometry in the pelvis with background field removal methods," *Magn. Reson. Med.*, vol. 84, no. 5, pp. 2495–2511, Nov. 2020, doi: https://doi.org/10.1002/mrm.28302.
- [104] C. Liu, "Susceptibility tensor imaging," *Magn. Reson. Med.*, vol. 63, no. 6, pp. 1471–1477, Jun. 2010, doi: https://doi.org/10.1002/mrm.22482.